Technische Universität München
Prof. Dr.-Ing. Nikolaus Adams

– **Master's Thesis** –

Non-Equilibrium Wall Model for Large Eddy Simulation

Author:
Alexander Avdonin
Registration Number:
3601787

Supervisors:
Dr. Stefan Hickel
Prof. Nikolaus Adams

28. Februar 2014
Lehrstuhl für Aerodynamik, Technische Universität München

Bestätigung der eigenständigen Arbeit

Ich erkläre hiermit, dass ich diese Arbeit ohne fremde Hilfe angefertigt und nur die in dem Literaturverzeichnis angeführten Quellen und Hilfsmittel benutzt habe.

München, den 28.02.2014 _____

Name:	Alexander Avdonin
Matrikelnummer	3601787

Abstract

The objective of this thesis is to develop a new non-equilibrium wall model for large-eddy simulation (LES). The wall model is derived from the thin boundary layer equations (TBLE). A convective term model is proposed that reduces the TBLE to a set of ordinary differential equations. The new wall model is validated by a stand-alone simulation and by LES of turbulent channel flow and shock/turbulent boundary layer interaction. Coarse LES with the wall model compare well with LES with near-wall resolution. The results suggest that the error introduced by neglecting the convective term is much smaller than the error introduced by the eddy viscosity model. Thus, improvement of the eddy viscosity model is of paramount importance in wall modeling research.

Contents

List of Figures

List of Tables

Notation

Latin characters

C_f		skin friction coefficient
c_p	$[J/(kgK)]$	specific heat capacity at constant pressure
c_v	$[J/(kgK)]$	specific heat capacity at constant volume
$\mathcal{D}$		eddy viscosity damping function
e	$[J/kg]$	inner energy per unit mass
e_t	$[J/kg]$	total energy per unit mass
h	$[J/kg]$	enthalpy per unit mass
h	$[m]$	grid spacing
k	$[W/(mK)]$	thermal conductivity
L	$[m]$	domain length
l^+		viscous length scale
l_{mix}	$[m]$	mixing length
M		Mach number
N		number of cells
Pr		Prandtl number
p	$[Pa]$	pressure
$\boldsymbol{q}$	$[W/m^2]$	heat flux
Re		Reynold number
R	$[J/(kgK)]$	specific gas constant
Re		Reynold number
Re_τ		Reynold number based on friction velocity
r		recovery factor
$\boldsymbol{S}$	$[1/s]$	strain rate tensor
s		scaling factor
T	$[K]$	temperature
T_t	$[K]$	total temperature
T_w	$[K]$	wall temperature
t	$[s]$	time
$\boldsymbol{t}$	$[N/m^2]$	stress tensor
$\boldsymbol{u}$	$[m/s]$	velocity vector
u	$[m/s]$	streamwise velocity

u_τ	$[m/s]$	friction velocity
v	$[m/s]$	wall-normal velocity
$\mathcal{W}$		weighting function
w	$[m/s]$	spanwise velocity
x	$[m]$	streamwise coordinate
y	$[m]$	wall-normal coordinate
y^+		wall distance in wall units
y_{top}	$[m]$	height of the wall model interface
z	$[m]$	spanwise coordinate

Greek characters

α		growth rate
γ		ratio of specific heats
γ^2	$[m^2/s^2]$	turbulence intensity
Δ	$[m]$	grid spacing
δ	$[m]$	boundary layer thickness
κ		von Karman constant
μ	$[kg/(ms)]$	dynamic viscosity
ν	$[m^2/s]$	dynamic viscosity
ρ	$[kg/m^3]$	density
ρ_w	$[kg/m^3]$	density at the wall
$\boldsymbol{\tau}$	$[N/m^2]$	shear stress tensor
$\boldsymbol{\tau}^R$	$[N/m^2]$	Reynolds shear stress tensor
$\boldsymbol{\tau}^{SGS}$	$[N/m^2]$	subgrid-scale stress tensor
τ_w	$[N/m^2]$	wall shear stress

Abbreviations

APGTBL	turbulent boundary layer in adverse pressure gradient
CFD	computational fluid dynamics
CFL	Courant-Friedrichs-Lewy (condition)
DNS	direct numerical simulation
FTT	flow through time
GWF	generalized wall function
ILES	implicit large-eddy simulation
LES	large-eddy simulation
LES-NWR	large-eddy simulation with near-wall resolution
OTBLE	ordinary thin boundary layer equations
RANS	Reynolds averaged Navier-Stokes (equations)
SGS	subgrid-scale (term)
STBLI	shock/turbulent boundary layer interaction
TBL	thin boundary layer
TBLE	thin boundary layer equations
TCF	turbulent channel flow
WMLES	large-eddy simulation with wall model

1. Introduction

Large-eddy simulation (LES) has become popular in scientific research. On one hand it yields more accurate results than Reynolds averaged simulations (RANS) since LES resolves the most part of the turbulence kinetic energy, whereas it is completely modeled in RANS. On the other hand LES is not as expensive as direct numerical simulation (DNS) since LES does not resolve the smallest turbulence length and time scales. LES resolves only the large scales and filters out scales smaller than the mesh size. Since the small scales tend to be more homogeneous and isotropic than the large ones, it is assumed that the subgrid-scale (SGS) terms can be modeled.
The cost of an LES, however, increases drastically if a solid surface is present in the simulation. The near-wall grid size should be in order of $y^+ \approx 1$ for accurate prediction of the wall shear stress. Thus, this "near-wall problem" requires DNS-like resolution. In this work large-eddy simulation with near-wall resolution is abbreviated as LES-NWR. The near-wall grid resolution depends on the Reynolds number. That makes high Reynolds number flow simulations extremely expensive and thus, keeps LES application to engineering flows quite limited.
There are two different methods to overcome the "near-wall problem". The first method is a hybrid LES/RANS, in which the Reynolds averaged equations are solved in the inner layer, while the filtered Navier-Stokes equations are solved away from the wall. The RANS approach completely models the turbulent kinetic energy. Therefore, the grid requirement is less severe than for the LES-NWR.The disadvantage of this method is occurrence of the log layer mismatch at the interface between RANS and LES, i.e., the RANS velocity profile does not match the LES velocity profile in the log region. This feature was observed and discussed in [3, 4, 5, 6, 7, 8].
The other method is to predict the wall shear stress directly from the field quantities in the LES near-wall cells. These models are based on the thin boundary layer equations (TBLE) or on the law of the wall. Large-eddy simulations with such models are abbreviated as WMLES.
The aim of this study is to develop and to validate a new non-equilibrium wall model for LES, which solves a set of ordinary differential equations. This set of equations is a simplification of the TBLE.
In Chapter 2 the governing equations for RANS and LES are introduced. Chapter 3 discusses the thin boundary layer theory and derives the TBLE, which are solved by the wall model. Chapter 4 deals with wall modeling for LES. At first, an overview of different wall models for LES is given, than the motivation for the new model is explained and finally, the model is described. Chapter 5 gives details of the wall model implementation. In Chapter 6 the developed model is validated by two in-

compressible and one compressible implicit large-eddy simulations. Results of coarse WMLES are compared to that of LES-NWR. Chapter 7 summarizes this study. It also gives an insight into possible improvements of the developed wall model.

2. Gouverning Equations

2.1. Governing equations for compressible flows

The governing equations for compressible flow in conservative variables neglecting body forces (such as gravity force) can be written as

$$\frac{\partial \rho}{\partial t} + \frac{\partial}{\partial x_j}(\rho u_j) = 0, \tag{2.1.1}$$

$$\frac{\partial \rho u_i}{\partial t} + \frac{\partial \rho u_i u_j}{\partial x_j} + \frac{\partial p}{\partial x_i} = \frac{\partial \tau_{ij}}{\partial x_j}, \tag{2.1.2}$$

$$\frac{\partial \rho e_t}{\partial t} + \frac{\partial (\rho e_t + p) u_j}{\partial x_j} = \frac{\partial t_{ij} u_i}{\partial x_j} - \frac{\partial q_j}{\partial x_j}, \tag{2.1.3}$$

where t and x_i are independent variables representing time and spacial coordinates in Cartesian coordinate system. The three components of the velocity vector $\mathbf{u}$ are denoted u_i $(i = 1, 2, 3)$. The Einstein summation convention over repeated indices applies. All indices are written in a contravariant form since covariant and contravariant systems coincide in Cartesian coordinate system. The density of a fluid is denoted by ρ, the pressure by p, the total energy per mass unit by e_t, the shear stress tensor by τ_{ij} and the heat flux by q_j. Eq. (2.1.1) is the mass continuity equation, Eq. (2.1.2) is the momentum equation, and Eq. (2.1.3) is the total energy equation. The total energy per unit mass e_t consists of the internal energy and the kinetic energy

$$e_t = e + \frac{1}{2}\rho u_i u_i. \tag{2.1.4}$$

For an ideal gas the relation between the density ρ, the pressure p and the static temperature T is given by the equation of state

$$p = \rho R T. \tag{2.1.5}$$

The specific gas constant is $R = c_p - c_v$, where c_p and c_v are the specific heats at constant pressure and constant volume, respectively. The ratio between the two specific heats is denoted by $\gamma = \frac{c_p}{c_v}$. An ideal gas for that R, c_p, c_v and thus, γ are constant is usually called a calorically perfect gas[1]. In this work we consider only

[1] Anderson in [9] distinguishes between calorically perfect gas with $c_p, c_v, \gamma = const$, thermally perfect gas with $c_p, c_v, \gamma = f(T)$, chemical equilibrium reacting gas with $c_p, c_v, \gamma = f(T, p)$ and chemical non-equilibrium reacting gas with $c_p, c_v, \gamma = f(T, p, t)$

calorically perfect gas. Using the equation of state, the internal energy per unit mass e can be written as

$$e = c_v T = \frac{p}{\rho(1-\gamma)}. \tag{2.1.6}$$

It should be noted that the total energy equation can be written in other variables such as temperature T or specific enthalpy $h = \frac{\gamma p}{(\gamma-1)\rho}$. The total energy equation can also be replaced by the internal energy equation. With respect to the wall modeling, the internal energy equation in two slightly different forms are of great interest

$$\rho\frac{\partial c_v T}{\partial t} + \rho u_i \frac{\partial c_v T}{\partial x_i} + p\frac{\partial u_i}{\partial x_i} = \tau_{ij}\frac{\partial u_i}{\partial x_j} - \frac{\partial q_j}{\partial x_j} \tag{2.1.7}$$

and

$$\rho\frac{\partial c_p T}{\partial t} + \rho u_i \frac{\partial c_p T}{\partial x_i} - \frac{\partial p}{\partial t} - u_j\frac{\partial p}{\partial x_j} = \tau_{ij}\frac{\partial u_i}{\partial x_j} - \frac{\partial q_j}{\partial x_j}. \tag{2.1.8}$$

Nevertheless, the only way to formulate this equation in conservative form is to chose the total energy. In a Newtonian fluid the shear stress tensor is given by

$$\tau_{ij} = 2\mu(S_{ij} - \frac{1}{3}S_{kk}\delta_{ij}) + \mu_v S_{kk}\delta_{ij}, \tag{2.1.9}$$

where

$$S_{ij} = \frac{1}{2}(\frac{\partial u_i}{\partial x_j} + \frac{\partial u_j}{\partial x_i}) \tag{2.1.10}$$

is the strain rate tensor, μ_v is the bulk viscosity which resists compression and expansion in the same way that the dynamic viscosity μ resists strain. According to the Stokes's hypothesis μ_v can be neglected. For compressible flow the variation of viscosity with temperature must be taken into account. A commonly used relation for the dynamic viscosity is that of Sutherland

$$\frac{\mu}{\mu_0} = \left(\frac{T}{T_0}\right)^{\frac{3}{2}} \frac{T_0 + S_1}{T + S_1}, \tag{2.1.11}$$

where for air $T_0 = 273.15\ K$, $S_1 = 110.4\ K$ and $\mu_0 = 1.716 \cdot 10^{-5}\ kg/ms$. The Sutherland's law is valid from 100 K to 1900 K. If the temperature ranges between 150 K and 500 K then it can be approximated by the power law

$$\frac{\mu}{\mu_0} = \left(\frac{T}{T_0}\right)^{0.76}. \tag{2.1.12}$$

The heat flux is described by the Fourier's law

$$q_j = -k\frac{\partial T}{\partial x_j}, \tag{2.1.13}$$

where the thermal conductivity k depends on the temperature as the dynamic viscosity does. It is usually convenient to express the variation in k through the Prandtl number

$$Pr = \frac{\mu c_p}{k}. \tag{2.1.14}$$

The value for air equals $Pr = 0.71$ and is almost constant in the temperature range between 300 K and 2000 K.
It is possible to write the governing equations in a non-dimensional form

$$x_i = L_{ref} x_i^*, \qquad u = U_{ref} u^*, \tag{2.1.15}$$

$$\rho = \rho^* \rho_{ref}, \qquad t = \frac{U_{ref} t^*}{L_{ref}}, \tag{2.1.16}$$

$$p = \frac{p^*}{\rho_{ref} u_{ref}^2}, \qquad e_t = \frac{e_t^*}{\rho_{ref} u_{ref}^2}, \tag{2.1.17}$$

$$T = T_{ref} T^*, \qquad \mu = \mu_{ref} \mu^* \tag{2.1.18}$$

$$c_p = c_{p,ref} c_p^*, \qquad R = R^* R_{ref}, \tag{2.1.19}$$

$$\tag{2.1.20}$$

where quantity with superscript * denotes the dimensionless form. Applying these non-dimensional definitions on Eq. (2.1.1)-(2.1.3) yields

$$\frac{\partial \rho^*}{\partial t^*} + \frac{\partial}{\partial x_j^*}(\rho^* u_j^*) = 0, \tag{2.1.21}$$

$$\frac{\partial \rho^* u_i^*}{\partial t^*} + \frac{\partial \rho^* u_i^* u_j^*}{\partial x_j^*} + \frac{\partial p^*}{\partial x_i^*} = \frac{1}{Re} \frac{\partial t_{ij}^*}{\partial x_j^*}, \tag{2.1.22}$$

$$\frac{\partial \rho^* e_t^*}{\partial t^*} + \frac{\partial (\rho^* e_t^* + p^*) u_j^*}{\partial x_j^*} = \frac{1}{Re} \frac{\partial \tau_{ij}^* u_i^*}{\partial x_j^*} - \frac{1}{RePrM_0^2(\gamma - 1)} \frac{\partial q_j^*}{\partial x_j^*} \tag{2.1.23}$$

with the Reynolds number $Re = \frac{\rho_{ref} U_{ref} L_{ref}}{\mu_{ref}}$, the Prandtl number $Pr = \frac{\mu_{ref} c_{p,ref}}{k_{ref}}$ and the Mach number $M_0 = \frac{U_{ref}}{\sqrt{\gamma R_{ref} T_{ref}}}$. For convenience we redefine the dynamic viscosity as $\mu = \frac{\mu^*}{Re}$, the specific heat at constant pressure as $c_p = \frac{c_p^*}{M_0^2(\gamma - 1)}$ and drop superscript *

$$\frac{\partial \rho}{\partial t} + \frac{\partial}{\partial x_j}(\rho u_j) = 0, \tag{2.1.24}$$

$$\frac{\partial \rho u_i}{\partial t} + \frac{\partial \rho u_i u_j}{\partial x_j} + \frac{\partial p}{\partial x_i} = \frac{\partial \tau_{ij}}{\partial x_j}, \tag{2.1.25}$$

$$\frac{\partial \rho e_t}{\partial t} + \frac{\partial (\rho e_t + p) u_j}{\partial x_j} = \frac{\partial \tau_{ij} u_i}{\partial x_j} - \frac{\partial q_j}{\partial x_j}. \tag{2.1.26}$$

Now, non-dimensional Eq. (2.1.24)-(2.1.26) have exactly the same form as Eq. (2.1.1)-(2.1.3) with dimensioned variables. The only one difference is in material parameters μ, c_p, k and R. The non-dimensional specific gas constant R is computed as

$$R = \frac{1}{\gamma M_0^2}. \tag{2.1.27}$$

2.2. Governing equations for incompressible flows

A simplification of the equations stated in the previous section is obtained by assuming constant density. Furthermore, assuming constant dynamic viscosity and no heat transfer, the governing equations will read as

$$\frac{\partial u_i}{\partial x_i} = 0, \tag{2.2.1}$$

$$\frac{\partial u_j}{\partial t} + u_i \frac{\partial u_j}{\partial x_i} + \frac{1}{\rho}\frac{\partial p}{\partial x_j} = \nu \frac{\partial^2 u_j}{\partial x_i \partial x_i}, \tag{2.2.2}$$

where $\nu = \frac{\mu}{\rho}$ is the kinematic viscosity. The continuity equation has become a constraint for the velocity field which should hold at any time. Under the above assumptions the energy equation is completely decoupled from analysis. If a given problem involves heat transfer and hence, temperature gradients exist in the flow, the temperature field can be obtained from the energy equation after solving the continuity and momentum equations for the velocity and pressure fields.
The incompressible Navier-Stokes equations in non-dimensional form look exactly like their dimensional counterpart but with the kinematic viscosity $\nu = 1/Re_{ref}$.

2.3. RANS equations

In Sections 2.1 and 2.2 the general gouverning equations have been introduced. They are suitable for any laminar flow simulation or DNS. To perform RANS simulation or LES, where the turbulence modeling is applied, a special form of governing equations is required. For incompressible RANS simulations the governing equations are Reynolds-averaged, and for compressible RANS simulations the equations are Favre-averaged. The various flow properties are decomposed in means and fluctuating parts and the averaging operator is applied on the governing equations.

2.3.1. Reynolds Averaging

When the Reynolds decomposition is applied, the instantaneous value q is written as a sum of a mean part $\overline{q}$ or Q and a fluctuating part q'. The mean value of a random field q can be considered either as an ensemble average over a large number of realizations N with

$$Q = \frac{1}{N}\sum_{n=1}^{N} q_n, \tag{2.3.1}$$

or as a time average over a long period T with

$$Q = \frac{1}{T}\int_{t-T}^{t+T} q(\tau)d\tau. \tag{2.3.2}$$

If we consider steady flows, it is convenient to relate the Reynolds averaging to the time average, for time dependent flows the ensemble average is the more suitable type of averaging. The averaging operator has following properties:

1. The average of the fluctuating quantity is zero:
$$\overline{q'} = 0. \tag{2.3.3}$$

2. The averaged quantities do not affect and are not affected by averaging:
$$\overline{\overline{q}} = \overline{q}, \tag{2.3.4}$$
$$\overline{\overline{q}r} = \overline{q}\ \overline{r}. \tag{2.3.5}$$

3. The average of the sum is the sum of the averages (linearity):
$$\overline{q + r} = \overline{q} + \overline{r}. \tag{2.3.6}$$

4. Constants do not affect and are not affected by averaging:
$$\overline{aq} = a\overline{q}, \text{ where } a = const. \tag{2.3.7}$$

5. The average of the time or space derivative is equal to the corresponding derivative of the average (commutation with differentiation):
$$\overline{\frac{\partial q}{\partial s}} = \frac{\partial \overline{q}}{\partial s}, \text{ where } s = t, x_i. \tag{2.3.8}$$

Using the above properties, the average of the product of two instantaneous quantities q and r is computed in following way
$$\overline{qr} = \overline{q}\ \overline{r} + \overline{q'r'}. \tag{2.3.9}$$

2.3.2. Reynolds Averaged Governing Equations

For incompressible flow with no heat transfer Eq. (2.2.1) and (2.2.2) are solved for the velocity and pressure fields. We apply Reynolds decomposition on u_i and p
$$u_i = U_i + u_i', \tag{2.3.10}$$
$$p = P + p'. \tag{2.3.11}$$

Then, we average the governing equations. This yields the Reynolds averaged equations
$$\frac{\partial U_i}{\partial x_i} = 0, \tag{2.3.12}$$
$$\frac{\partial U_i}{\partial t} + U_j \frac{\partial U_i}{\partial x_j} + \frac{1}{\rho}\frac{\partial P}{\partial x_i} = \frac{\partial}{\partial x_j}\left(\nu \frac{\partial U_i}{\partial x_j} - \overline{u_i' u_j'}\right). \tag{2.3.13}$$

Apart from replacement of instantaneous values by mean values, the only one difference between the general equations and the Reynolds averaged equations is the appearance of the correlation term $\overline{u_i' u_j'}$. The quantity $-\overline{\rho u_i' u_j'}$ is known as the Reynolds stress tensor τ_{ij}^R. Because of the correlation terms, the averaged equations contain more unknowns than the number of equations which is known as the turbulence closure problem. The Reynolds stress tensor should be modeled. Many turbulence models are based on the Boussinesq eddy-viscosity approximation, which relates the Reynolds stress tensor with the dynamic eddy viscosity μ_t, the mean strain rate tensor $\overline{S_{ij}}$ and the turbulence kinetic energy $k = \frac{1}{2}\overline{\rho u_i' u_i'}$ in following way

$$-\overline{\rho u_j' u_i'} = 2\mu_t \overline{S}_{ij} - \frac{2}{3} k \delta_{ij}. \tag{2.3.14}$$

There are several ways to model the turbulence kinetic energy k (see Wilcox [10]). In this work we consider only simplest algebraic turbulence models. Therefore we do not model the turbulence kinetic energy and thus, we set it to zero. According to Wilcox [10] ignoring the turbulence kinetic energy is a good approximation for flows with Mach numbers up to supersonic range. Since the wall model for LES covers only a small part of the boundary layer close to the wall, this assumption is reasonable. For incompressible flow it is more common to use the kinematic eddy-viscosity $\nu_t = \frac{\mu_t}{\rho}$ instead of the dynamic one. For convenience we rewrite the viscous term $\nu \frac{\partial^2 U_j}{\partial x_i \partial x_i}$ in the Reynolds averaged equations using the mean strain rate tensor and apply the Boussinesq eddy-viscosity approximation. That yields the Reynolds averaged equations in the form, which is used in Chapter 3 to derive the thin boundary layer equations

$$\frac{\partial U_i}{\partial x_i} = 0, \tag{2.3.15}$$

$$\frac{\partial U_i}{\partial t} + U_j \frac{\partial U_i}{\partial x_j} + \frac{1}{\rho}\frac{\partial P}{\partial x_i} = \frac{\partial}{\partial x_j}\left(2\left(\nu + \nu_t\right)\overline{S}_{ij}\right). \tag{2.3.16}$$

2.3.3. Favre Averaging

In compressible flow in addition to velocity and pressure fluctuations we must also account for density and temperature fluctuations. Therefore, the Reynolds averaging of governing equations leads to additional correlations like $\overline{\rho' u_i'}$ even in the continuity equation, which is not desirable. For that reason a Favre (mass) averaged quantity is introduced

$$q = \tilde{q} + q'', \tag{2.3.17}$$

where q is an instantaneous value, $\tilde{q}$ is a mass-averaged part, and q'' is a fluctuating part. As in case of the Reynolds averaging, $\tilde{q}$ can be either an ensemble average with

$$\tilde{q} = \frac{1}{\overline{\rho} N} \sum_{n=1}^{N} \rho_n q_n, \tag{2.3.18}$$

or a time average with

$$\tilde{q} = \frac{1}{T\overline{\rho}} \int_{t-T}^{t+T} \rho(\tau) q(\tau) d\tau, \tag{2.3.19}$$

where $\overline{\rho}$ is the Reynolds averaged density. According to the above definition, the relation between Favre and Reynolds average is given by

$$\overline{\rho}\tilde{q} = \overline{\rho q}. \tag{2.3.20}$$

Furthermore,

$$q'' = q - \overline{q} - \frac{\overline{\rho' q'}}{\overline{\rho}} \tag{2.3.21}$$

and

$$\overline{q''} = -\frac{\overline{\rho' q'}}{\overline{\rho}}. \tag{2.3.22}$$

The Favre average becomes Reynolds average when the density fluctuation tends to zero, i.e., the flow is incompressible.

2.3.4. Favre Averaged Governing Equations

In order to average the governing equations we decompose the field quantities

$$u_i = \tilde{u}_i + u_i'', \tag{2.3.23}$$
$$\rho = \overline{\rho} + \rho', \tag{2.3.24}$$
$$p = P + p', \tag{2.3.25}$$
$$e = \tilde{e} + e'', \tag{2.3.26}$$
$$h = \tilde{h} + h'', \tag{2.3.27}$$
$$T = \tilde{T} + T''. \tag{2.3.28}$$

Note that the density and Pressure are Reynolds decomposed, whereas other quantities are Favre decomposed. The Favre averaging is only a mathematical simplification, the governing equations (2.1.1)-(2.1.3) are still Reynolds averaged, but the variables are written in the Favre decomposed way. This mathematical trick simplifies the equations. The averaging of the continuity equation is straightforward

$$\frac{\partial \overline{\rho}}{\partial t} + \frac{\partial}{\partial x_i}(\overline{\rho}\tilde{u}_i) = 0. \tag{2.3.29}$$

Because of high order correlations, the averaging of the momentum and energy equations is a tedious and complex process with numerous assumptions. The detailed derivation can be found, e.g., in [10]. The momentum equation in primitive form[2] reads:

$$\overline{\rho}\frac{\partial \tilde{u}_i}{\partial t} + \overline{\rho}\tilde{u}_j\frac{\partial \tilde{u}_i}{\partial x_j} + \frac{\partial P}{\partial x_i} = \frac{\partial}{\partial x_j}\left(\tilde{\tau}_{ij} - \overline{\rho u_i'' u_j''}\right), \tag{2.3.30}$$

[2]Transformation between conservative and primitive form is given in Appendix A.1

where

$$\tilde{\tau}_{ij} = 2\mu(\tilde{S}_{ij} - \frac{1}{3}\tilde{S}_{kk}\delta_{ij}) + \mu_v\tilde{S}_{kk}\delta_{ij} \tag{2.3.31}$$

and

$$\tilde{S}_{ij} = \frac{1}{2}(\frac{\partial\tilde{u}_i}{\partial x_j} + \frac{\partial\tilde{u}_j}{\partial x_i}). \tag{2.3.32}$$

Fluctuation of the dynamic viscosity is neglected $\mu = \overline{\mu} = \tilde{\mu}$. This equation differ from the instantaneous governing equations by the appearance of the Favre averaged Reynolds stress tensor τ_{ij}^R, which is modeled exactly as in Section 2.3.2

$$-\overline{\rho u_j'' u_i''} = 2\mu_t\tilde{S}_{ij} - \frac{2}{3}k\delta_{ij}, \tag{2.3.33}$$

where the turbulence kinetic energy $k = \frac{1}{2}\overline{\rho u_i'' u_i''}$ is neglected. Instead of the averaged total energy equation, the averaged internal energy equation is given

$$\overline{\rho}\frac{\partial c_p\tilde{T}}{\partial t} + \overline{\rho}\tilde{u}_i\frac{\partial c_p\tilde{T}}{\partial x_i} - \frac{\partial P}{\partial t} - \tilde{u}_j\frac{\partial P}{\partial x_j} = \left(\tilde{\tau}_{ij} - \overline{\rho u_j'' u_i''}\right)\frac{\partial u_i}{\partial x_j} - \frac{\partial}{\partial x_j}\left(\tilde{q}_j + \overline{\rho u_j'' h''}\right). \tag{2.3.34}$$

The turbulent heat flux vector $q_{t,j} = \overline{\rho u_j'' h''}$ is assumed to be proportional to the mean temperature gradient

$$q_{t,j} \approx -\frac{\mu_t c_p}{Pr_t}\frac{\partial\tilde{T}}{\partial x_j} = -k_t\frac{\partial\tilde{T}}{\partial x_j}, \tag{2.3.35}$$

fluctuation of c_p with temperature is neglected, Pr_t is the turbulent Prandtl number, which is assumed to be constant. The most common values for Pr_t are 0.89 or 0.9 according to [10]. The equation of state for the averaged quantities reads

$$P = \overline{\rho}R\tilde{T}. \tag{2.3.36}$$

Summarizing, we write the entire set of equations after all simplifications

$$\frac{\partial\overline{\rho}}{\partial t} + \frac{\partial}{\partial x_j}(\overline{\rho}\tilde{u}_j) = 0, \tag{2.3.37}$$

$$\overline{\rho}\frac{\partial\tilde{u}_i}{\partial t} + \overline{\rho}\tilde{u}_j\frac{\partial\tilde{u}_i}{\partial x_j} + \frac{\partial P}{\partial x_i} = \frac{\partial}{\partial x_j}\left(2\left(\mu + \mu_t\right)\tilde{S}_{ij} - \frac{2}{3}\mu\tilde{S}_{kk}\delta_{ij}\right), \tag{2.3.38}$$

$$\overline{\rho}c_p\frac{\partial\tilde{T}}{\partial t} + \overline{\rho}\tilde{u}_i c_p\frac{\partial\tilde{T}}{\partial x_i} - \frac{\partial P}{\partial t} - \tilde{u}_j\frac{\partial P}{\partial x_j} = \left(2\left(\mu + \mu_t\right)\tilde{S}_{ij} - \frac{2}{3}\mu\tilde{S}_{kk}\delta_{ij}\right)\frac{\partial\tilde{u}_i}{\partial x_j} + \frac{\partial}{\partial x_j}\left(\left(k + k_t\right)\frac{\partial\tilde{T}}{\partial x_j}\right), \tag{2.3.39}$$

$$P = \overline{\rho}R\tilde{T}. \tag{2.3.40}$$

The difference between the instantaneous equations of motion and the Favre averaged equations is in the effective viscosity and heat conductivity. Nevertheless, the turbulent viscosity and heat conductivity are not related to molecular processes. They are consequences of the convective transport of the fluctuating velocity u'' and fluctuating enthalpy h'' by the fluctuating mass $\rho u''$.

2.4. Introduction to Large Eddy Simulation

In large-eddy simulation the larger unsteady turbulent motions are directly represented, whereas the smaller-scale motions are modeled. If the filter and the grid are sufficiently fine, LES resolves more than 80% of the turbulence energy. According to Pope [1], there are four conceptual steps in LES:

1. A filtering operation is defined to decompose the flow field quantities like velocity, density, pressure and temperature into filtered (resolved) components and residual (subgrid-scale) components. The filtered components are capable of resolving the motion of the large eddies.

2. The equations for the evolution of the filtered quantities are derived from the governing equations given in sections 2.1 and 2.2. The filtered equations contain the residual stress tensor (or SGS stress tensor)

3. The residual stress tensor is modeled either by an explicit SGS model or an implicit SGS model.

4. The resulting equations are solved numerically.

2.4.1. Filtering

The general filtering operation was introduced by Leonard [11]. It is defined by

$$\overline{q}(\mathbf{x},t) = \int_{-\infty}^{\infty} G(\mathbf{r},\mathbf{x}) q(\mathbf{x}-\mathbf{r},t) d\mathbf{r}, \tag{2.4.1}$$

where integration is performed over the entire flow domain, q is a field variable and the specified function G satisfies the normalization condition

$$\int G(\mathbf{r},\mathbf{x}) d\mathbf{r} = 1. \tag{2.4.2}$$

The filtering operation (2.4.1) is also called a convolution operation

$$\overline{q} = G \star q, \tag{2.4.3}$$

where G is a convolution kernel. There are several different filter functions (convolution kernels) in physical space $(\mathbf{x},t)$ as well as in spectral space $(\mathbf{k},t)$, which can be found, e.g., in [1]. The decomposition of a random quantity q in a filtered part $\overline{q}$ and a residual part q',

$$q = \overline{q} + q', \tag{2.4.4}$$

appears analogous to the Reynolds decomposition. We even use the same notation for the Filtering and Reynolds operators. Indeed, the filtering operator has similar properties to the Reynolds averaging operator:

1. Conservation of constants:

$$\overline{a} = a, \tag{2.4.5}$$
$$\overline{a\overline{q}} = a\overline{q}, \text{ where } a = const. \tag{2.4.6}$$

2. Linearity:

$$\overline{q + r} = \overline{q} + \overline{r}. \tag{2.4.7}$$

3. Commutation with differentiation:

$$\overline{\frac{\partial q}{\partial s}} = \frac{\partial \overline{q}}{\partial s}, \text{ where } s = t, x_i. \tag{2.4.8}$$

However, there are important differences. In general, following properties of Reynolds averaging operator are not fulfilled by the filtering operator

$$\overline{\overline{q}} \neq \overline{q}, \tag{2.4.9}$$
$$\overline{q'} \neq 0, \tag{2.4.10}$$
$$\overline{\overline{q}r} \neq \overline{q}\ \overline{r}. \tag{2.4.11}$$

2.4.2. Filtered Governing Equations

Applying the filtering operation $[G \star\ ]$ on Eq.(2.2.1) and (2.2.2) yields the filtered equations of motion for incompressible flow

$$\frac{\partial U_i}{\partial x_i} = 0, \tag{2.4.12}$$
$$\frac{\partial U_j}{\partial t} + U_i \frac{\partial U_j}{\partial x_i} + \frac{1}{\rho}\frac{\partial P}{\partial x_j} = \frac{\partial}{\partial x_i}\left(\nu \frac{\partial U_j}{\partial x_i} - \frac{\tau_{ij}^{SGS}}{\rho}\right), \tag{2.4.13}$$

where U_i and P are filtered field variables and $\tau_{ij}^{SGS} = \overline{\rho u_i u_j} - \rho U_i U_j$ is the residual (SGS) stress tensor. An introduction to the modeling of the SGS stress tensor is given in Section 2.4.4. The filtered equations for incompressible flow are analogous to the Reynolds averaged equations (2.3.12) and (2.3.13). Nevertheless, these two operations have different physical meaning. Hence, the Reynolds stress tensor τ_{ij}^{R} is not equal to the SGS stress tensor τ_{ij}^{SGS}.

2.4.3. Favre Filtered Governing Equations

In compressible LES as in compressible RANS it is convenient to use Favre filtered variables. Any field quantity q can be decomposed into a Favre filtered part $\tilde{q}$ and residual part q''

$$q = \tilde{q} + q''. \tag{2.4.14}$$

A Favre filtered quantity can be computed in following way

$$\tilde{q} = \frac{\overline{\rho q}}{\overline{q}}. \tag{2.4.15}$$

The governing equation for compressible flow (2.1.1)-(2.1.3) are conventional filtered but the change of variables of filtered velocity and temperature fields to the Favre filtered fields is applied:

$$\frac{\partial \overline{\rho}}{\partial t} + \frac{\partial}{\partial x_i}(\overline{\rho}\tilde{u}_i) = 0, \tag{2.4.16}$$

$$\overline{\rho}\frac{\partial \tilde{u}_i}{\partial t} + \overline{\rho}\tilde{u}_j\frac{\partial \tilde{u}_i}{\partial x_j} + \frac{\partial P}{\partial x_i} = \frac{\partial}{\partial x_j}\left(\tilde{\tau}_{ij} - \tau_{ij}^{SGS}\right), \tag{2.4.17}$$

$$\begin{aligned}\overline{\rho}\frac{\partial c_p\tilde{T}}{\partial t} + \overline{\rho}\tilde{u}_i\frac{\partial c_p\tilde{T}}{\partial x_i} - \frac{\partial P}{\partial t} - \tilde{u}_j\frac{\partial P}{\partial x_j} = \\ \tilde{\tau}_{ij}\frac{\partial \tilde{u}_i}{\partial x_j} - \frac{\partial \tilde{q}_j}{\partial x_j} - \left[\frac{\partial c_v F_j}{\partial x_j} + \Pi_{dil} - \epsilon_v + \frac{\partial Q_j}{\partial x_j}\right].\end{aligned} \tag{2.4.18}$$

The SGS stress tensor in the momentum equation is $\tau_{ij}^{SGS} = \overline{\rho u_i u_j} - \overline{\rho}\tilde{u}_i\tilde{u}_j$. Eq. (2.4.18) is the internal energy equation in temperature formulation. All terms which should be modeled are enclosed in square brackets. The SGS temperature flux is defined as

$$F_j = \overline{\rho}\left(\widetilde{u_j T} - \tilde{u}_j\tilde{T}\right). \tag{2.4.19}$$

The SGS pressure-dilatation can be written as

$$\Pi_{dil} = \overline{p\frac{\partial u_j}{\partial x_j}} - \overline{p}\frac{\partial \tilde{u}_j}{\partial x_j}. \tag{2.4.20}$$

The SGS viscous dissipation is expressed as

$$\epsilon_v = \overline{\tau_{ij}\frac{\partial u_i}{\partial x_j}} - \tilde{\tau}_{ij}\frac{\partial \tilde{u}_i}{\partial x_j}, \tag{2.4.21}$$

and the SGS heat flux is

$$Q_j = \overline{q_j} - \tilde{q}_j = -\overline{k(T)\frac{\partial T}{\partial x_j}} + k(\tilde{T})\frac{\partial \tilde{T}}{\partial x_j}. \tag{2.4.22}$$

There are different ways to write the set of governing equations, which can be found, e.g., in Garnier *et al.* [12]. This formulation has been chosen to allow for direct comparison with the Favre averaged equations (2.3.37)-(2.3.39).

2.4.4. SGS Modeling

There are several different approaches to model the SGS stress tensor. One possible way to structure these models is to distinguish between explicit and implicit

SGS models. Applying the explicit SGS Model, the filtering and the modeling are independent of the numerical discretization method. Thus, 'filtered' and 'residual' components are more appropriate terms then 'resolved' and 'subgrid' components. The discretization scheme is, under other aspects, also responsible for the resolution quality of the field quantities. The other important aspect that determines the resolution quality is the grid resolution, which is more or less included in the explicit SGS model. On the other hand, implicit SGS models use the truncation error of the numerical scheme to describe the SGS stress tensor. In this case the modeling, grid and the discretization scheme are coupled. Each scheme has its own SGS model. Different SGS models, explicit, as well as implicit, can be found, e.g., in [12]. Description of existing models is beyond the scope of this work.

3. Thin boundary layer theory

The boundary layer theory was developed by Prandtl. He assumed that the viscous effects are limited to a thin region close to a surface, so called the boundary layer. Whereas, the flow outside this region can be considered as inviscid. The boundary layer should be thin, i.e., $\delta << L$, which implies $Re \gg 1$. The non-dimensional distance from the leading edge should be large, i.e., the boundary layer is developed. Originally, the thin boundary layer theory was developed for laminar incompressible flow. Later it was extended for both turbulent and compressible flow.
The structure of a thin boundary layer is given in Figure 3.1. The sketch shows

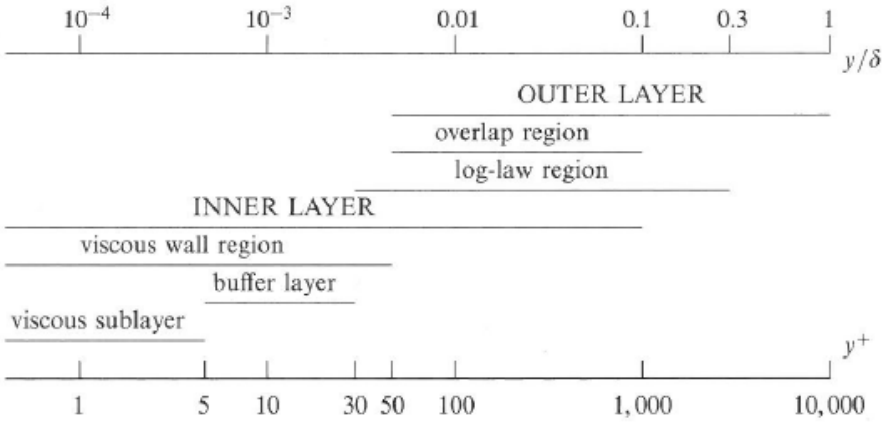

Figure 3.1.: Different boundary layer regions defined in y^+ and y/δ for the steady turbulent channel flow at $Re_\tau = 10^4$. The Sketch is taken from [1]

typical boundary layer regions on example of the steady turbulent channel flow at $Re_\tau = 10^4$. The inner layer is usually defined in wall units, it consists of the viscous sublayer ($y^+ < 5$), the buffer layer ($5 < y^+ < 30$) and the overlap region with the outer layer. In the viscous sublayer without pressure gradient the flow is dominated by the viscosity, hence the velocity can be described by the differential equation $\frac{d^2U}{dy^2} = 0$. That gives the linear velocity profile. If the velocity at any point in the viscous sublayer is known then the wall shear stress can be computed with the best accuracy because of the linearity of the velocity profile. The buffer layer is the transition region between the viscosity-dominated and the turbulence-dominated parts of the flow. The overlap region, also called log region, is defined by $y^+ > 30$ and $y < 0.3\delta$, and it is dominated by turbulent momentum transfer. The velocity profile has a shape of a logarithmic function and it follows the law of the wall given

in Eq. (4.1.1). In the outer region, which is sometimes called wake region, effects of the viscosity on the velocity profile become weaker until they are fully negligible for $y > \delta$, i.e., outside of the thin boundary layer.
In following sections the thin boundary layer equations (TBLE) are derived for turbulent incompressible and compressible flow. The TBLE are simplified governing equations of motion. The derivation is performed using the scale analysis. Terms with lower orders, i.e., with a small contribution to the motion are neglected. The scale analysis is applicable on terms that do not contain instantaneous fluctuations. Hence, the TBLE can be derived for laminar flow or Reynolds averaged flow, but not for filtered flow if instantaneous fluctuations are so high that the scale analysis is no longer possible. Because of the same reason the TBLE do not hold in separation region.

3.1. Thin Boundary Layer Equations for Incompressible Turbulent Flow

In this section, the two-dimensional thin boundary layer equations for incompressible turbulent flow are derived. The extension to three dimensions is straight forward. The streamwise direction is denoted by $x_1 = x$, and the wall-normal direction by $x_2 = y$. The corresponding velocities are $u_1 = u$ and $u_2 = v$, respectively. The two-dimensional averaged governing equations are derived from Eq. (2.3.12) and (2.3.13):

$$\frac{\partial U}{\partial x} + \frac{\partial V}{\partial y} = 0, \tag{3.1.1}$$

$$\frac{\partial U}{\partial t} + U\frac{\partial U}{\partial x} + V\frac{\partial U}{\partial y} + \frac{1}{\rho}\frac{\partial P}{\partial x} = \nu\left(\frac{\partial^2 U}{\partial x^2} + \frac{\partial^2 U}{\partial y^2}\right) - \left(\frac{\partial}{\partial x}\overline{u'^2} + \frac{\partial}{\partial y}\overline{u'v'}\right), \tag{3.1.2}$$

$$\frac{\partial V}{\partial t} + U\frac{\partial V}{\partial x} + V\frac{\partial V}{\partial y} + \frac{1}{\rho}\frac{\partial P}{\partial y} = \nu\left(\frac{\partial^2 V}{\partial x^2} + \frac{\partial^2 V}{\partial y^2}\right) - \left(\frac{\partial}{\partial x}\overline{u'v'} + \frac{\partial}{\partial y}\overline{v'^2}\right). \tag{3.1.3}$$

Usually, the derivation of TBLE is performed for steady flows. Here we keep the time dependence $\frac{\partial U}{\partial t}$ and $\frac{\partial V}{\partial t}$, since mathematically, the derivation is possible including these terms. The second important note is that even if we consider two-dimensional flow, the turbulence is three-dimensional. Due to symmetry, the Reynolds stresses $\overline{u'w'}$ and $\overline{v'w'}$ are zero.
If we assume that a typical length in the streamwise direction is L, a typical length in the wall-normal direction is δ and the streamwise velocity is of the order of the free stream velocity U_e then we can estimate the magnitude of the wall-normal velocity v from the continuity equation (3.1.1):

$$V \sim \frac{\delta}{L} U_e. \tag{3.1.4}$$

It is assumed that the fluctuating terms in the momentum equation, $\overline{u'^2}$, $\overline{u'v'}$, $\overline{v'^2}$, are of the same order of magnitude

$$\overline{v'^2} \lesssim |\overline{u'v'}| \lesssim \overline{u'^2} \sim \gamma^2 U_e^2, \tag{3.1.5}$$

where γ^2 is the turbulence intensity. In steady thin boundary layers $\gamma^2 << 1$. The turbulence intensity can also be estimated considering the convective and turbulent diffusive time scales

$$t_{convective} \sim \frac{L}{U_e}, \tag{3.1.6}$$

$$t_{turbulent} \sim \frac{\delta^2}{\nu_t}. \tag{3.1.7}$$

We also require that the two time scales are of the same order $t_{convective} \sim t_{turbulent}$ that implies

$$\nu_t \sim \frac{U_e \delta^2}{L}. \tag{3.1.8}$$

To relate the eddy viscosity ν_t with the Reynolds stress tensor we take the Boussinesq approximation $-\overline{u'v'} = \nu_t \frac{\partial U}{\partial y}$. Hence,

$$\gamma^2 \sim \frac{\delta}{L} \ll 1. \tag{3.1.9}$$

Pressure term $\frac{P}{\rho}$ can be estimated of the order U_e^2, the time scale t of the order $\frac{L}{U_e}$, the kinematic viscosity ν of the order $\frac{U_e L}{Re}$. The terms in the wall-normal momentum equation can be estimated as

$$\begin{aligned} &\underbrace{\mathcal{O}\left(\frac{V}{t}\right)}_{\frac{\partial V}{\partial t}} + \underbrace{\mathcal{O}\left(\frac{U_e V}{L}\right)}_{U\frac{\partial V}{\partial x}} + \underbrace{\mathcal{O}\left(\frac{V^2}{\delta}\right)}_{V\frac{\partial V}{\partial y}} + \underbrace{\mathcal{O}\left(\frac{P}{\rho\delta}\right)}_{\frac{1}{\rho}\frac{\partial P}{\partial y}} = \\ &\underbrace{\mathcal{O}\left(\frac{\nu V}{L^2}\right)}_{\nu\frac{\partial^2 V}{\partial x^2}} + \underbrace{\mathcal{O}\left(\frac{\nu V}{\delta^2}\right)}_{\nu\frac{\partial^2 V}{\partial y^2}} + \underbrace{\mathcal{O}\left(\frac{\gamma^2 U_e^2}{L}\right)}_{\frac{\partial}{\partial x}\overline{u'v'}} + \underbrace{\mathcal{O}\left(\frac{\gamma^2 U_e^2}{\delta}\right)}_{\frac{\partial}{\partial y}\overline{v'^2}}. \end{aligned} \tag{3.1.10}$$

Using the above derived estimations for V, t, $\frac{P}{\rho}$, ν and γ^2 yields

$$\begin{aligned} &\mathcal{O}\left(\frac{U_e^2\delta}{L^2}\right) + \mathcal{O}\left(\frac{U_e^2\delta}{L^2}\right) + \mathcal{O}\left(\frac{U_e^2\delta}{L^2}\right) + \mathcal{O}\left(\frac{U_e^2}{\delta}\right) = \\ &\mathcal{O}\left(\frac{U_e^2\delta}{ReL^2}\right) + \mathcal{O}\left(\frac{U_e^2}{Re\delta}\right) + \mathcal{O}\left(\frac{U_e^2\delta}{L^2}\right) + \mathcal{O}\left(\frac{U_e^2}{L}\right). \end{aligned} \tag{3.1.11}$$

Since $\frac{\delta}{L} \ll 1$ and $Re \gg 1$ the highest order term is $\frac{1}{\rho}\frac{\partial P}{\partial y} = \mathcal{O}\left(\frac{U_e^2}{\delta}\right)$. Neglecting other lower order terms the momentum equation in the wall-normal direction reduces to

$$\frac{1}{\rho}\frac{\partial P}{\partial y} = 0. \tag{3.1.12}$$

That means the pressure variation across the thin boundary layer can be neglected.The second highest order term, which is neglected, is $\frac{\partial}{\partial y}\overline{v'^2} = \mathcal{O}\left(\frac{U_e^2}{L}\right)$. Hence, the relative error is of the order of $\gamma^2 \sim \frac{\delta}{L}$.
Order of the terms in the momentum equation in the streamwise direction (3.1.2) can be estimated in the similar way

$$\mathcal{O}\left(\frac{U_e^2}{L}\right) + \mathcal{O}\left(\frac{U_e^2}{L}\right) + \mathcal{O}\left(\frac{U_e^2}{L}\right) + \mathcal{O}\left(\frac{U_e^2}{L}\right) = \\ \mathcal{O}\left(\frac{U_e^2}{ReL}\right) + \mathcal{O}\left(\frac{U_e^2 L}{Re\delta^2}\right) + \mathcal{O}\left(\frac{U_e^2\delta}{L^2}\right) + \mathcal{O}\left(\frac{U_e^2}{L}\right). \tag{3.1.13}$$

The lowest order terms, the streamwise molecular and turbulent diffusion, $\nu\frac{\partial^2 U}{\partial x^2}$ and $\frac{\partial}{\partial x}\overline{u'^2}$, are neglected. The relative error is of the order γ^2. The thin boundary layer equations for incompressible turbulent flow read

$$\frac{\partial U}{\partial x} + \frac{\partial V}{\partial y} = 0, \tag{3.1.14}$$

$$\frac{\partial U}{\partial t} + U\frac{\partial U}{\partial x} + V\frac{\partial U}{\partial y} + \frac{1}{\rho}\frac{dP}{dx} = \nu\frac{\partial^2 U}{\partial y^2} - \frac{\partial}{\partial y}\overline{u'v'}, \tag{3.1.15}$$

$$\frac{\partial P}{\partial y} = 0. \tag{3.1.16}$$

The Reynolds stress term $\overline{u'v'}$ is equal to zero for laminar flow.

3.2. Thin Boundary Layer Equations for Compressible Turbulent Flow

The two-dimensional averaged governing equations are derived from Eq. (2.3.37), (2.3.38) and (2.3.39)

$$\frac{\partial \overline{\rho}}{\partial t} + \frac{\partial \overline{\rho}\tilde{u}}{\partial x} + \frac{\partial \overline{\rho}\tilde{v}}{\partial y} = 0, \tag{3.2.1}$$

$$\overline{\rho}\frac{\partial \tilde{u}}{\partial t} + \overline{\rho}\tilde{u}\frac{\partial \tilde{u}}{\partial x} + \overline{\rho}\tilde{v}\frac{\partial \tilde{u}}{\partial y} + \frac{\partial P}{\partial x} = \frac{\partial}{\partial x}\left(2\left(\mu+\mu_t\right)\frac{\partial \tilde{u}}{\partial x} - \frac{2}{3}\mu\left(\frac{\partial \tilde{u}}{\partial x} + \frac{\partial \tilde{v}}{\partial y}\right)\right) + \frac{\partial}{\partial y}\left(\mu+\mu_t\right)\left(\frac{\partial \tilde{u}}{\partial y} + \frac{\partial \tilde{v}}{\partial x}\right), \tag{3.2.2}$$

$$\overline{\rho}\frac{\partial \tilde{v}}{\partial t} + \overline{\rho}\tilde{u}\frac{\partial \tilde{v}}{\partial x} + \overline{\rho}\tilde{v}\frac{\partial \tilde{v}u}{\partial y} + \frac{\partial P}{\partial y} = \frac{\partial}{\partial y}\left(2\left(\mu+\mu_t\right)\frac{\partial \tilde{v}}{\partial y} - \frac{2}{3}\mu\left(\frac{\partial \tilde{u}}{\partial x} + \frac{\partial \tilde{v}}{\partial y}\right)\right) + \frac{\partial}{\partial x}\left(\mu+\mu_t\right)\left(\frac{\partial \tilde{u}}{\partial y} + \frac{\partial \tilde{v}}{\partial x}\right), \tag{3.2.3}$$

$$\begin{aligned}\overline{\rho}c_p\frac{\partial \tilde{T}}{\partial t} + \overline{\rho}\tilde{u}c_p\frac{\partial \tilde{T}}{\partial x} + \overline{\rho}\tilde{v}c_p\frac{\partial \tilde{T}}{\partial y} - \frac{\partial P}{\partial t} - \tilde{u}\frac{\partial P}{\partial x} - \tilde{v}\frac{\partial P}{\partial y} = \\ \left(2\left(\mu+\mu_t\right)\frac{\partial \tilde{u}}{\partial x} - \frac{2}{3}\mu\left(\frac{\partial \tilde{u}}{\partial x} + \frac{\partial \tilde{v}}{\partial y}\right)\right)\frac{\partial \tilde{u}}{\partial x} + \left(\mu+\mu_t\right)\left(\frac{\partial \tilde{u}}{\partial y} + \frac{\partial \tilde{v}}{\partial x}\right)\frac{\partial \tilde{u}}{\partial y} \\ \left(2\left(\mu+\mu_t\right)\frac{\partial \tilde{v}}{\partial y} - \frac{2}{3}\mu\left(\frac{\partial \tilde{u}}{\partial x} + \frac{\partial \tilde{v}}{\partial y}\right)\right)\frac{\partial \tilde{v}}{\partial y} + \left(\mu+\mu_t\right)\left(\frac{\partial \tilde{u}}{\partial y} + \frac{\partial \tilde{v}}{\partial x}\right)\frac{\partial \tilde{v}}{\partial x} \\ + \frac{\partial}{\partial x}\left(\left(k+k_t\right)\frac{\partial \tilde{T}}{\partial x}\right) + \frac{\partial}{\partial y}\left(\left(k+k_t\right)\frac{\partial \tilde{T}}{\partial y}\right).\end{aligned} \tag{3.2.4}$$

The derivation of the TBLE for compressible turbulent flow is similar to the derivation in Section 3.1. In the continuity equation (3.2.1) the time dependent term is assumed to be of the lower order than the two other terms. This assumption is justified for steady flow or if time dependence is sufficiently weak. The equation yields the relation

$$\tilde{v} \sim \frac{\delta}{L}\tilde{u}_e. \tag{3.2.5}$$

The simplified momentum equation states that the pressure variation across the boundary layer can be neglected

$$\overline{\rho}\frac{\partial \tilde{u}}{\partial t} + \overline{\rho}\tilde{u}\frac{\partial \tilde{u}}{\partial x} + \overline{\rho}\tilde{v}\frac{\partial \tilde{u}}{\partial y} + \frac{dP}{dx} = \frac{\partial}{\partial y}\left(\left(\mu+\mu_t\right)\frac{\partial \tilde{u}}{\partial y}\right), \tag{3.2.6}$$

$$\frac{\partial P}{\partial y} = 0. \tag{3.2.7}$$

In the internal energy equation, the lower order terms like derivatives $\frac{\partial^2}{\partial x^2}$ and $\frac{\partial^2}{\partial x \partial y}$ are neglected. All time dependent terms are kept. The simplified equation reads

$$\overline{\rho} c_p \frac{\partial \tilde{T}}{\partial t} + \overline{\rho} \tilde{u} c_p \frac{\partial \tilde{T}}{\partial x} + \overline{\rho} \tilde{v} c_p \frac{\partial \tilde{T}}{\partial y} - \frac{\partial P}{\partial t} - \tilde{u} \frac{\partial P}{\partial x} = \\ (\mu + \mu_t) \left(\frac{\partial \tilde{u}}{\partial y} \right)^2 + \frac{\partial}{\partial y} \left((k + k_t) \frac{\partial \tilde{T}}{\partial y} \right). \quad (3.2.8)$$

Eq. (3.2.1), (3.2.6), (3.2.7) and (3.2.8) are the TBLE for compressible flow.

4. Wall Model for LES

4.1. Overview of Wall Models

In this section an overview of existing wall models for LES is exposed. According to Cabot and Moin [13], wall models can be distinguished by type of the boundary condition supplied to LES.
One approach is to apply the boundary conditions directly on the velocity field at some physical distance to the wall, i.e., LES does not see any wall. These conditions are referred to as off-wall boundary conditions. Attempts to apply such boundary conditions have been proven to be largely unsuccessful [14, 15, 16]. One of the reasons for that might be the energy transfer between the model and the LES, which might be unphysical.
The other models, so called wall stress models, supply only the wall shear stress and do not change the velocity field. These models are the most promising. Simplest models are algebraic models. They are based on the law of the wall. They are valid if the flow is incompressible and steady, if there is no pressure gradient and the interface between the wall model and LES cells is located in the log layer. Then the streamwise velocity is given by

$$U = u_\tau \frac{1}{\kappa} \ln\left(\frac{y u_\tau}{\nu}\right) + B, \quad \text{with } u_\tau^2 = \frac{\tau_w}{\rho_w}, \tag{4.1.1}$$

where τ_w is the wall shear stress, ρ_w is the density at the wall, u_τ is the friction velocity, $\kappa \approx 0.4$ is von Karman's constant and $B \approx 5$. The law of the wall can also be applied for compressible flows with adiabatic walls if the velocity is van Driest transformed

$$U_{VD} = u_\tau \frac{1}{\kappa} \ln\left(\frac{y u_\tau}{\nu}\right) + B. \tag{4.1.2}$$

The van Driest Transformation is given in Appendix A.2. The standard wall function can be extended by a term that accounts for a pressure gradient. The new wall function is called the generalized wall function, which was implemented, e.g., by Shih *et al.* [17]. The algebraic wall stress models (even extended models) are very efficient but imply the law of the wall for the mean velocity, which is not valid in many complex flows. The next type of models is based on the TBLE. The TBLE

for incompressible flow can be written in following way

$$\frac{\partial U}{\partial x} + \frac{\partial V}{\partial y} + \frac{\partial W}{\partial z} = 0, \tag{4.1.3}$$

$$\frac{\partial}{\partial x_2}\left(\nu + \nu_t\right)\frac{\partial u_i}{\partial x_2} = F_i, \tag{4.1.4}$$

$$\frac{\partial P}{\partial x_2} = 0, \tag{4.1.5}$$

where

$$F_i = \frac{1}{\rho}\frac{\partial P}{\partial x_i} + \frac{\partial u_i}{\partial t} + \frac{\partial}{\partial x_j}\left(u_i u_j\right) \tag{4.1.6}$$

and $i = 1, 3$ are wall-tangential directions. Because of the convective term $\frac{\partial}{\partial x_j}\left(u_i u_j\right)$, these equations are partial differential equations. The wall model embedded cells need information from neighboring cells in all three directions. This model is referred to as the TBLE model, which was investigated, e.g., by Wang and Moin [18], Zhen *et al.* [19]. Applying this model is numerically more efficient than to perform LES with near-wall resolution. Furthermore, there is no need to solve the Poisson equation since the pressure is constant in the wall-normal direction, and the pressure gradient in wall-tangential directions is taken from the LES at the interface. The TBLE model has two simpler variants with $F_i = 0$ and $F_i = \frac{1}{\rho}\frac{dP}{dx_i}$. Then equations are reduced to ordinary differential equations in the wall-normal direction $y = x_2$. The computational effort is strongly reduced. The exclusion of the convective term reduces the partial differential equations to ordinary differential equations. Nevertheless, the full TBLE model gives the best results. The objective of this work is to develop a model for the convective term, which does not require information from neighboring embedded cells in wall-tangential direction, i.e., the differential equations remain ordinary. Theoretically, this new model can achieve results of TBLE model with less computational effort. The model is derived in Section 4.4 for incompressible flow and in Section 4.5 for compressible flow.

4.2. Modeling of the Turbulent Eddy-Viscosity

TBLE models require an appropriate turbulent eddy viscosity model. The wall model height extends at least to the log region, where the flow is turbulence-dominated. Hence, the turbulent eddy viscosity model is crucial for any wall model. A simple Smagorinsky model that can be used in explicit LES is too inaccurate near the wall. Nevertheless, it should be a robust algebraic model to keep the wall model as simple and efficient as possible. The most common models are the mixing length models with wall damping. This section discusses such models. The Prandtl's mixing length hypothesis defines the eddy viscosity as

$$\mu_t = \rho l_{mix}^2 \left|\frac{dU}{dy}\right|. \tag{4.2.1}$$

This equation was derived for a flat shear flow, where U is the streamwise velocity, y is the direction across the shear layer, and l_{mix} is the mixing length. In the log region following relation holds

$$l_{mix} \sim \kappa y. \tag{4.2.2}$$

To account for the viscous sublayer and the buffer region, van Driest proposed to introduce a damping function $\mathcal{D}$, such that

$$l_{mix} = \kappa y \mathcal{D}. \tag{4.2.3}$$

A van Driest-style damping function D is given by

$$\mathcal{D}(y^+) = \left[1 - \exp\left(-y^{+n}/A^n\right)\right]^m, \tag{4.2.4}$$

where A, n and m are modeling parameters. The mean velocity derivative $\frac{dU}{dy}$ is computed from the law of the wall (see Eq. (4.1.1))

$$\frac{dU}{dy} = \frac{u_\tau}{\kappa y}. \tag{4.2.5}$$

Inserting Eq. (4.2.3) and (4.2.5) into Eq. (4.2.1) yields the eddy viscosity

$$\mu_t = \mu \kappa y^+ \mathcal{D}^2. \tag{4.2.6}$$

To summarize, the eddy viscosity model is derived using the properties of the log layer. The deviation from the log layer is corrected by tuning parameters of the damping function. These models are highly empirical and thus are far from perfect. The invention of a new eddy viscosity model is far beyond the scope of this work. Hence we consider only two existing models:

1. Classical van Driest eddy viscosity model with $\mathcal{D}(y^+) = [1 - \exp(-y^+/A)]$, where $\kappa = 0.4$ and $A = 19$.

2. A more sophisticated eddy viscosity model that takes into account the pressure gradient. It is taken from Duprat *et al.* [20] and is defined by

$$\mu_t = \mu y^* \kappa \left[\alpha + y^* (1-\alpha)^{3/2}\right]^\beta \left[1 - e^{-y^*/\left(1+A\alpha^3\right)}\right]^2, \tag{4.2.7}$$

   where $\kappa = 0.41$, $A = 17$, $\beta = 0.78$. For the non-dimensional length $y^* = y u_{\tau p}/\nu$ and velocity $U^* = U/u_{\tau p}$, a new combined friction velocity $u_{\tau p} = \sqrt{u_\tau^2 + u_p^2}$ is used that consists of the classical friction velocity $u_\tau = \sqrt{|\tau_w|/\rho}$ and an additional velocity based on the streamwise pressure gradient $u_p = |(\mu/\rho^2)(dP/dx)|^{1/3}$; $\alpha = u_\tau^2/u_{\tau p}^2$ is a non-dimensional parameter. This eddy viscosity model is reffed to as the Duprat eddy viscosity model throughout.

4.3. Motivation for the Convective Term Modeling

Before the new wall model is stated, the importance of the convective term in the wall vicinity is shown on a complex flow case of Hickel and Adams [21]. This case is the incompressible non-equilibrium turbulent flat-plate boundary layer flow with a displacement-thickness Reynolds number going from $Re_{\delta 1} = 1000$ to 30000, labeled APGTBL throughout. Due to the strong non-equilibrium conditions that result from a constant adverse pressure-gradient imposed at the upper domain boundary, the mean velocity profiles of this boundary layer flow do not follow the classic logarithmic law of the wall. The adverse pressure gradient leads to an unsteady and massive flow separation, which is not fixed in space and covers more than a third of the computational domain. Figure 4.1 shows the mean streamlines. The time

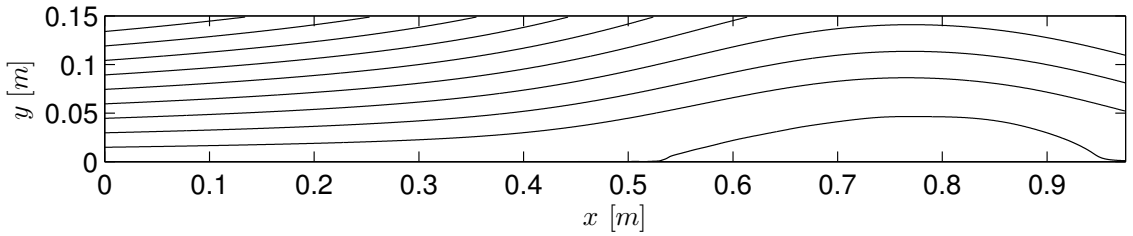

Figure 4.1.: APGTBL, mean streamlines

averaged separation region is located between $x = 0.53\ m$ and $0.97\ m$. Using the time averaged data from the fully resolved LES-NWR, the time averaged terms of the thin boundary layer equation in streamwise direction (see Eq. (3.1.2)) can be reconstructed. Figure 4.2 shows the pressure gradient $(1/\rho)\, dP/dx$, the viscous term $\nu \partial^2 U/\partial y^2$, the convective term $U\partial U/\partial x + V\partial U/\partial y$ and the unresolved Reynolds stress term at five different stations $x = \{0.1\ m, 0.2\ m, 0.3\ m, 0.4\ m, 0.5\ m\}$. The stations are chosen, where the flow in average is not separated. Hence, the TBLE can be applied. According to the TBLE the unresolved Reynolds stress term is represented by $-\frac{\partial \overline{u'v'}}{\partial y}$. Nevertheless, this term is not contained in the LES database. Thus, it is computed using the TBLE

$$-\frac{\partial \overline{u'v'}}{\partial y} = U\frac{\partial U}{\partial x} + V\frac{\partial U}{\partial y} + \frac{1}{\rho}\frac{dP}{dx} - \nu\frac{\partial^2 U}{\partial y^2}, \tag{4.3.1}$$

and thus, the unresolved term accounts for all numerical and boundary layer approximation errors. In the region $y < 0.1\delta_0$, the most significant terms are the unresolved Reynolds stress term, the viscous and the pressure terms. As predicted by the TBL theory the pressure variation across the boundary layer can be neglected in comparison to the variation of other terms. If the region $y < 0.1\delta_0$ should be modeled, the above mentioned terms should be included in the modeling. This figure states that the convective term is zero at the near-wall region $y < 0.01\delta_0$ and in the entire boundary layer at $x = 0.5\ m$ that is close to the separation. The convective term

becomes important above $y < 0.01\delta_0$, but it still has the minor contribution to the streamwise momentum equation. In this case it is not worth to rise computational effort by choosing partial differential equations for the wall modeling instead of ordinary differential equations just to account for the convective term. If the convective term can be modeled in the way that partial differential equations are not required than the wall model quality will rise without considerable computational costs. Convective term modeling has been discussed by Hickel *et al.* [22]. In this work a new convective term model is proposed. The new model is presented in following section.

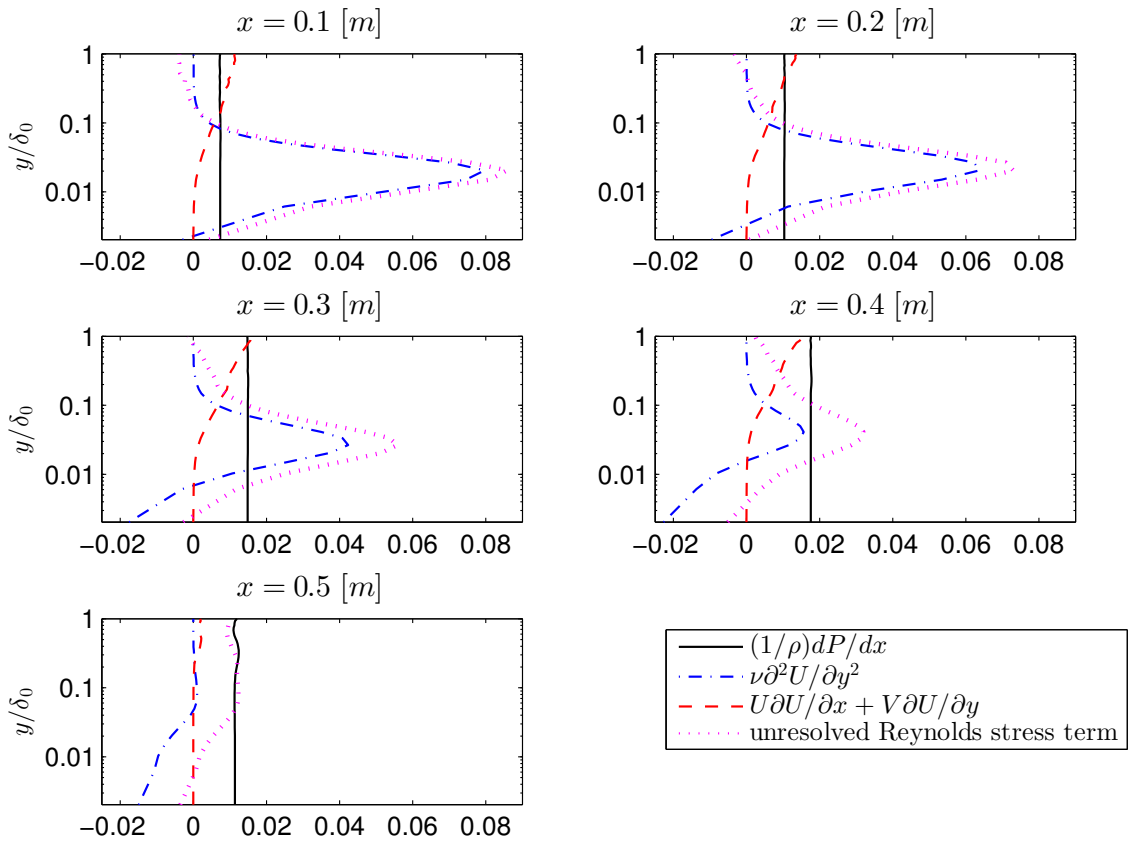

Figure 4.2.: APGTBL, time averaged terms of the streamwise momentum equation across the boundary layer at different streamwise locations. All terms are scaled by a local boundary layer thickness. The wall-distance is scaled by the inlet boundary thickness δ_0.

4.4. Convective Term Modeling for Incompressible Flow

4.4.1. Two-Dimensional Flow

At first, the new model is shown for a plane flow, where the motion in spanwise direction is fully neglected. Afterwards, the model is extended to three dimensions. The new model solves the two-dimensional TBLE on a near-wall embedded grid

$$\frac{\partial U}{\partial x} + \frac{\partial V}{\partial y} = 0, \tag{4.4.1}$$

$$\frac{\partial U}{\partial t} + U\frac{\partial U}{\partial x} + V\frac{\partial U}{\partial y} + \frac{1}{\rho}\frac{dP}{dx} = \frac{\partial}{\partial y}\left(\nu + \nu_t\right)\frac{\partial U}{\partial y}. \tag{4.4.2}$$

The field quantities at the upper boundary of the embedded grid are denoted by subscript $_{top}$. The pressure term does not vary in the embedded mesh. Hence, it is taken from the LES cell at the interface

$$\frac{1}{\rho}\frac{dP}{dx} = \left(\frac{1}{\rho}\frac{dP}{dx}\right)_{top} = \left(\frac{1}{\rho}\frac{dP}{dx}\right)_{LES}. \tag{4.4.3}$$

The velocity at the upper boundary is also taken from the LES cell $U_{top} = U_{LES}$, The velocity at the no-slip wall is zero $U_w = 0$. The convective term can be modeled as one term or it can be split in modeling of $\frac{\partial U}{\partial x}(y)$ and $V(y)$. The latter method is easier. It is enough to find an appropriate model for $\frac{\partial U}{\partial x}(y)$, then the wall-normal velocity is obtained by the integration of the continuity equation

$$V(y) = -\int_0^y \frac{\partial U}{\partial x}(\tilde{y})\, d\tilde{y}. \tag{4.4.4}$$

The streamwise derivative of the mean velocity and the convective term in general are very poorly studied, there are no physical models to describe it. Therefore, $\frac{\partial U}{\partial x}(y)$ is expressed as a polynomial function

$$\frac{\partial U}{\partial x}(y) = \sum_{i=0}^{n} a_i y^i. \tag{4.4.5}$$

The wall model has only two sources of information, the wall itself and the LES cell in which the wall model grid is embedded. Hence, we search for the terms

$$\left(\frac{\partial U}{\partial x}\right)_w, \quad \left(\frac{\partial^{1+i} U}{\partial x \partial y^i}\right)_w \quad \text{with } i = 1, 2, 3, .. \tag{4.4.6}$$

$$V_{top}, \quad \left(\frac{\partial U}{\partial x}\right)_{top}, \quad \left(\frac{\partial^{1+j} U}{\partial x \partial y^j}\right)_{top}, \quad \text{with } j = 1, 2, 3, .. \tag{4.4.7}$$

The information available at the wall is $\left(\frac{\partial U}{\partial x}\right)_w = 0$ that yields the polynomial coefficient $a_0 = 0$. The LES cell can give all types of the information listed in Eq. (4.4.7). Nevertheless, coarse resolution in the wall-normal direction and numerical differentiation introduce numerical errors. That makes the higher order derivatives unreliable. Furthermore, giving too many information at the upper boundary and only few at the wall might disturb behavior of $\frac{\partial U}{\partial x}$ close to the wall. Higher order polynomials might introduce oscillations that are not physical. In this work we consider at most the second order derivative of the mean velocity, i.e., we focus on V_{top}, $\left(\frac{\partial U}{\partial x}\right)_{top}$ and $\left(\frac{\partial^2 U}{\partial x \partial y}\right)_{top}$. On a staggered grid, which is commonly used for incompressible LES, it is advantageous to set the interface at the LES cell center since the continuity equation is fulfilled there. That yields the most accurate $\left(\frac{\partial U}{\partial x}\right)_{top}$. To accurately compute V_{top} and $\left(\frac{\partial^2 U}{\partial x \partial y}\right)_{top}$ the interface should be set not in a near-wall LES cell but at least in the second off-wall LES cell. Using all these informations from the LES cell, $\frac{\partial U}{\partial x}$ becomes the third order polynomial and V the forth order polynomial, respectively. If the term $\left(\frac{\partial^2 U}{\partial x \partial y}\right)_{top}$ is neglected, the order is reduced by one. Both polynomials are listed in Table 4.1. The polynomials are computed and compared to $\frac{\partial U}{\partial x}$ and V from

$\mathcal{O}\left(\frac{\partial U}{\partial x}\right)$	$\mathcal{O}\left(V(y)\right)$	$\frac{\partial U}{\partial x}(y)$	$V(y)$	Constraints
3	4	$\frac{\partial U}{\partial x}(y) = \sum_{i=1}^{3} a_i y^i$	$V(y) = -\sum_{i=1}^{3} \frac{1}{i+1} a_i y^{i+1}$	V_{top} $\left(\frac{\partial U}{\partial x}\right)_{top}$ $\left(\frac{\partial^2 U}{\partial x \partial y}\right)_{top}$
2	3	$\frac{\partial U}{\partial x}(y) = \sum_{i=1}^{2} a_i y^i$	$V(y) = -\sum_{i=1}^{2} \frac{1}{i+1} a_i y^{i+1}$	V_{top} $\left(\frac{\partial U}{\partial x}\right)_{top}$

Table 4.1.: Polynomials for $\frac{\partial U}{\partial x}$ and V modeling.

the database [21] in Figure 4.3. The interface has been chosen to be at $y_{top} = 0.1\delta_0$, where $\delta_0 = 5.8992\ mm$ is the inlet boundary layer thickness. The inlet boundary thickness is the smallest boundary layer thickness through the entire plate. There are minor differences in $\frac{\partial U}{\partial x}$. The higher order approximation is slightly better than the lower one, mainly close to the inlet, where the flow is attached. The difference between the approximations and the fully resolved LES in the wall-normal velocity is negligible. The third order polynomial serves as a sufficient approximation. A higher order does not give any visible advantages. Figure 4.4 shows the same models but with the interface at $y_{top} = 0.3\delta_0$. The shape of $\frac{\partial U}{\partial x}$ becomes more complicated such that the polynomials can not reproduce it at each location but they still can represent the global behavior. The higher order polynomial gives better results than the lower order polynomial. The shape of V is much better estimated than that of $\frac{\partial U}{\partial x}$. It should be noted that this *a posteriori* benchmark is idealistic since the in-

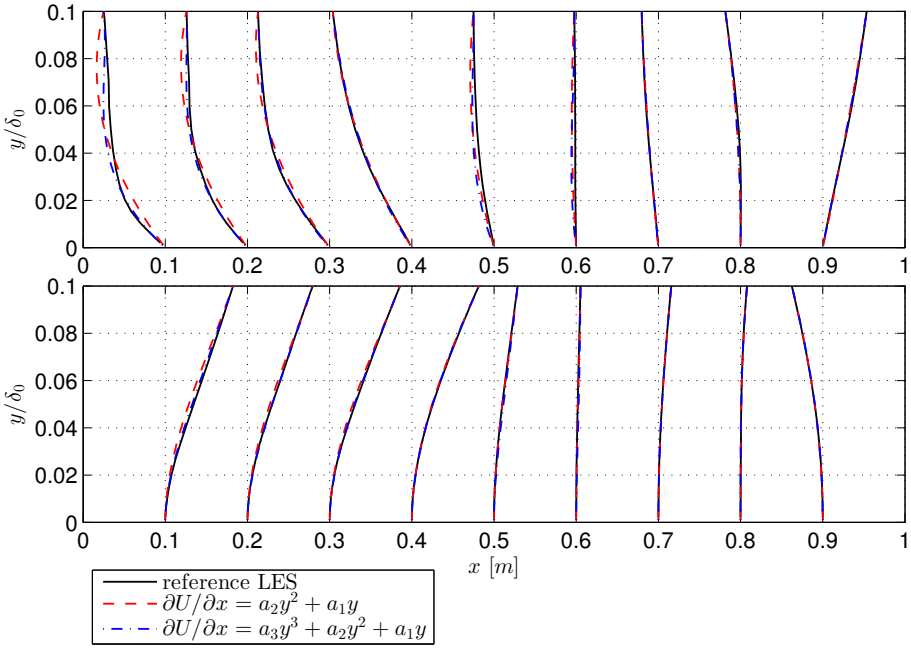

Figure 4.3.: APGTBL, (a) streamwise mean velocity derivative $\partial U/\partial x$, (b) wall-normal velocity V. Wall model interface at $y_{top} = 0.1\delta_0$.

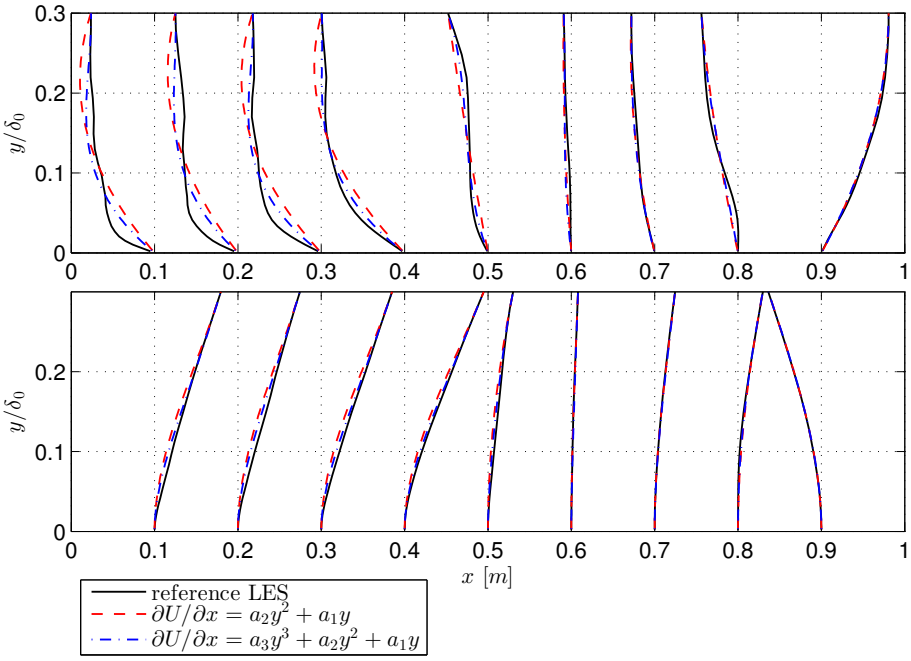

Figure 4.4.: APGTBL, (a) streamwise mean velocity derivative $\partial U/\partial x$, (b) wall-normal velocity V. Wall model interface at $y_{top} = 0.3\delta_0$.

formation at the interface was provided by the fully resolved LES database. The polynomial function gives good results given the perfect velocity field. Hence, if all other terms of the streamwise momentum equation are modeled well enough and the LES resolution is good enough to compute the derivatives at the interface then the polynomial model approximates $\frac{\partial U}{\partial x}$ and V accurately.

4.4.2. Three-Dimensional Flow

In this section the incompressible wall model is extended to a three-dimensional flow. The full TBLE equations in three dimensions are given by

$$\frac{\partial U}{\partial x} + \frac{\partial V}{\partial y} + \frac{\partial W}{\partial z} = 0, \tag{4.4.8}$$

$$\frac{\partial U}{\partial t} + U\frac{\partial U}{\partial x} + V\frac{\partial U}{\partial y} + W\frac{\partial U}{\partial z} + \frac{1}{\rho}\frac{dP}{dx} = \frac{\partial}{\partial y}\left(\nu + \nu_t\right)\frac{\partial U}{\partial y}, \tag{4.4.9}$$

$$\frac{\partial W}{\partial t} + U\frac{\partial W}{\partial x} + V\frac{\partial W}{\partial y} + W\frac{\partial W}{\partial z} + \frac{1}{\rho}\frac{dP}{dx} = \frac{\partial}{\partial y}\left(\nu + \nu_t\right)\frac{\partial U}{\partial y}. \tag{4.4.10}$$

In analogy to a two-dimensional flow, we get following quantities from the interface

$$\begin{gathered} V_{top}, \\ \left(\frac{\partial U}{\partial x}\right)_{top}, \quad \left(\frac{\partial^2 U}{\partial x \partial y}\right)_{top}, \quad \left(\frac{\partial U}{\partial z}\right)_{top}, \quad \left(\frac{\partial^2 U}{\partial z \partial y}\right)_{top}, \\ \left(\frac{\partial W}{\partial x}\right)_{top} \quad \left(\frac{\partial^2 W}{\partial x \partial y}\right)_{top}, \quad \left(\frac{\partial W}{\partial z}\right)_{top}, \quad \left(\frac{\partial^2 W}{\partial z \partial y}\right)_{top}. \end{gathered}$$

The terms $W\frac{\partial U}{\partial z}$ and $U\frac{\partial W}{\partial x}$ couple the momentum equations. We consider flows where one flow direction is dominating. Thus, these terms have the minor part in the momentum transport and they can be modeled by low order polynomials. We choose the first order polynomials for $\frac{\partial U}{\partial z}$ and $\frac{\partial W}{\partial x}$

$$\frac{\partial U}{\partial z} = \left(\frac{\partial U}{\partial z}\right)_{top}\frac{y}{y_{top}}, \tag{4.4.11}$$

$$\frac{\partial W}{\partial x} = \left(\frac{\partial W}{\partial x}\right)_{top}\frac{y}{y_{top}}. \tag{4.4.12}$$

This modeling is relatively cheap since it does not require higher order derivatives $\left(\frac{\partial^2 U}{\partial z \partial y}\right)_{top}$, $\left(\frac{\partial^2 W}{\partial x \partial y}\right)_{top}$ and any stabilizing features. There are five constrains at the interface to model $\frac{\partial U}{\partial x}$ and $\frac{\partial W}{\partial z}$, i.e., it is possible to compose one third order polynomial and one second order polynomial:

$$\left(\frac{\partial U}{\partial x}\right)^U = a_3^U y^3 + a_2^U y^2 + a_1^U y \quad \text{and} \quad \left(\frac{\partial W}{\partial z}\right)^U = b_2^U y^2 + b_1^U y, \tag{4.4.13}$$

or

$$\left(\frac{\partial U}{\partial x}\right)^W = a_2^W y^2 + a_1^W y \quad \text{and} \quad \left(\frac{\partial W}{\partial z}\right)^W = b_3^W y^3 + b_2^W y^2 + b_1^W y, \tag{4.4.14}$$

where superscript ^{U} or ^{W} denotes the velocity component that is described by a higher order polynomial. A smooth switch between the polynomials with different orders is ensured by a weighting function

$$\mathcal{W} = \frac{U_{top}^2}{U_{top}^2 + W_{top}^2}, \tag{4.4.15}$$

such that

$$\frac{\partial U}{\partial x} = \mathcal{W}\left(\frac{\partial U}{\partial x}\right)^U + (1-\mathcal{W})\left(\frac{\partial U}{\partial x}\right)^W, \tag{4.4.16}$$

$$\frac{\partial W}{\partial z} = \mathcal{W}\left(\frac{\partial W}{\partial z}\right)^U + (1-\mathcal{W})\left(\frac{\partial W}{\partial z}\right)^W. \tag{4.4.17}$$

The polynomial coefficients a_i^j and b_i^j are given in Appendix A.3. According to Figure 4.3 and 4.4 $|\partial U/\partial x| \leq |\left(\partial U/\partial x\right)_{top}|$. We use this fact to bound the derivatives $\partial U/\partial x$ and $\partial W/\partial z$. Thus, we require for $\partial U/\partial x$

$$\begin{cases} 0 \leq \frac{\partial U}{\partial x} \leq \left(\frac{\partial U}{\partial x}\right)_{top} & \text{if } \left(\frac{\partial U}{\partial x}\right)_{top} \geq 0, \\ \left(\frac{\partial U}{\partial x}\right)_{top} \leq \frac{\partial U}{\partial x} \leq 0 & \text{else,} \end{cases} \tag{4.4.18}$$

and for $\partial W/\partial z$

$$\begin{cases} 0 \leq \frac{\partial W}{\partial z} \leq \left(\frac{\partial W}{\partial z}\right)_{top} & \text{if } \left(\frac{\partial W}{\partial z}\right)_{top} \geq 0, \\ \left(\frac{\partial W}{\partial z}\right)_{top} \leq \frac{\partial W}{\partial z} \leq 0 & \text{else.} \end{cases} \tag{4.4.19}$$

In this way we prevent the polynomial to provide unphysical values for the mean velocity derivatives and, as a consequence, for the entire convective term. For convenience, we consider the system with superscript ^{U} (third order polynomial for $\frac{\partial U}{\partial x}$, second order for $\frac{\partial W}{\partial z}$), but the same restrictions are valid for the system with superscript ^{W}. In case of $\left(\frac{\partial W}{\partial z}\right)^U$, which is a second order polynomial, it is straightforward to fulfill the above constraint by requesting a restriction for $\left(\frac{\partial^2 W}{\partial z \partial y}\right)_{top}$

$$\begin{cases} 0 \leq \left(\frac{\partial^2 W}{\partial z \partial y}\right)_{top} \leq \frac{2}{y_{top}}\left(\frac{\partial W}{\partial z}\right)_{top} & \text{if } \left(\frac{\partial W}{\partial z}\right)_{top} \geq 0, \\ \frac{2}{y_{top}}\left(\frac{\partial W}{\partial z}\right)_{top} \leq \left(\frac{\partial^2 W}{\partial z \partial y}\right)_{top} < 0 & \text{else.} \end{cases} \tag{4.4.20}$$

If value of $\left(\frac{\partial^2 W}{\partial z \partial y}\right)_{top}$ that comes from a LES cell violates the above inequalities, $\left(\frac{\partial^2 W}{\partial z \partial y}\right)_{top}$ is set to an appropriate bound value, 0 or $\frac{2}{y_{top}}\left(\frac{\partial W}{\partial z}\right)_{top}$.

Bounding for the third order polynomial $\left(\frac{\partial U}{\partial x}\right)^U$ is not trivial, only one constraint can be easily prescribed at the interface:

$$\begin{cases} \left(\frac{\partial^2 U}{\partial x \partial y}\right)_{top} \geq 0 & \text{if } \left(\frac{\partial U}{\partial x}\right)_{top} \geq 0, \\ \left(\frac{\partial^2 U}{\partial x \partial y}\right)_{top} \leq 0 & \text{else.} \end{cases} \tag{4.4.21}$$

For certain combinations of $\{V_{top},\ \left(\frac{\partial^2 U}{\partial x \partial y}\right)_{top},\ \left(\frac{\partial W}{\partial z}\right)_{top},\ \left(\frac{\partial^2 W}{\partial z \partial y}\right)_{top}\}$ the third order polynomial still can get out of bounds. If it happens, the third order polynomial is reduced by one order neglecting V_{top}, and it becomes identical to $\left(\frac{\partial U}{\partial x}\right)^W$. After the order reduction, the modeled wall normal velocity V^U does not depend on V_{top} anymore. To account for V_{top} in the modeling of V^U, the scaling factor s^U is introduced

$$V^U(y) = -s^U \int_0^y \left(\frac{\partial U}{\partial x}\right)^U_{reduced} + \left(\frac{\partial W}{\partial z}\right)^U d\tilde{y} \tag{4.4.22}$$

with

$$s^U = \frac{V_{top}}{-\int_0^{y_{top}} \left(\frac{\partial U}{\partial x}\right)^U_{reduced} + \left(\frac{\partial W}{\partial z}\right)^U d\tilde{y}}. \tag{4.4.23}$$

This wall model with ordinary thin boundary layer equations is abbreviated as OTBLE_3, where index "3" stands for the highest order polynomial. The OTBLE_3 with the van Driest eddy viscosity is abbreviated as OTBLE_3_VD and the model with the Duprat eddy viscosity as OTBLE_3_Du, respectively.
If the partial cross-derivatives $\left(\frac{\partial^2 U}{\partial x \partial y}\right)_{top}$ and $\left(\frac{\partial^2 W}{\partial z \partial y}\right)_{top}$ are not computed then there are only three constraints at the interface. That is enough for one second and one first order polynomial:

$$\left(\frac{\partial U}{\partial x}\right)^U = a_2^U y^2 + a_1^U y \quad \text{and} \quad \left(\frac{\partial W}{\partial z}\right)^U = b_1^U y, \tag{4.4.24}$$

or

$$\left(\frac{\partial U}{\partial x}\right)^W = a_1^W y \quad \text{and} \quad \left(\frac{\partial W}{\partial z}\right)^W = b_2^W y^2 + b_1^W y. \tag{4.4.25}$$

The polynomial coefficients a_i^j and b_i^j are given in Appendix A.4. The first order polynomial does not require any bounding. The bounding of the second order polynomial on the example of the system "U",where $\left(\frac{\partial U}{\partial x}\right)_{top}$ is modifiable, is given by

$$\begin{cases} \left(\frac{\partial U}{\partial x}\right)_{top} \leq -3\frac{V_{top}}{y_{top}} - \frac{3}{2}\left(\frac{\partial W}{\partial z}\right)_{top} & \text{if } \left(\frac{\partial U}{\partial x}\right)_{top} \geq 0, \\ \left(\frac{\partial U}{\partial x}\right)_{top} \geq -3\frac{V_{top}}{y_{top}} - \frac{3}{2}\left(\frac{\partial W}{\partial z}\right)_{top} & \text{else.} \end{cases} \tag{4.4.26}$$

As in case of the third order polynomial, $\frac{\partial U}{\partial x}$ can get out of bounds for certain combinations of $\{V_{top},\ \left(\frac{\partial W}{\partial z}\right)_{top}\}$. The order reduction neglecting V_{top} leads to the first order polynomial. To account for V_{top} in the wall normal velocity modeling the scaling given in Eq. (4.4.2) and (4.4.2) is applied. This wall model with at most second order polynomial is abbreviated as OTBLE_2.
The model without the convective term is abbreviated as OTBLE_0.

4.5. Convective Term Modeling for Compressible Flow

The three-dimensional compressible TBLE equations read

$$\frac{\partial \overline{\rho}}{\partial t} + \frac{\partial \overline{\rho}\tilde{u}}{\partial x} + \frac{\partial \overline{\rho}\tilde{v}}{\partial y} + \frac{\partial \overline{\rho}\tilde{w}}{\partial z} = 0, \tag{4.5.1}$$

$$\overline{\rho}\frac{\partial \tilde{u}}{\partial t} + \overline{\rho}\tilde{u}\frac{\partial \tilde{u}}{\partial x} + \overline{\rho}\tilde{v}\frac{\partial \tilde{u}}{\partial y} + \overline{\rho}\tilde{w}\frac{\partial \tilde{u}}{\partial z} + \frac{\partial P}{\partial x} = \frac{\partial}{\partial y}\left((\mu + \mu_t)\frac{\partial \tilde{u}}{\partial y}\right), \tag{4.5.2}$$

$$\overline{\rho}\frac{\partial \tilde{w}}{\partial t} + \overline{\rho}\tilde{u}\frac{\partial \tilde{w}}{\partial x} + \overline{\rho}\tilde{v}\frac{\partial \tilde{w}}{\partial y} + \overline{\rho}\tilde{w}\frac{\partial \tilde{w}}{\partial z} + \frac{\partial P}{\partial z} = \frac{\partial}{\partial y}\left((\mu + \mu_t)\frac{\partial \tilde{w}}{\partial y}\right), \tag{4.5.3}$$

$$\begin{aligned}\overline{\rho}c_p\frac{\partial \tilde{T}}{\partial t} + \overline{\rho}\tilde{u}c_p\frac{\partial \tilde{T}}{\partial x} + \overline{\rho}\tilde{v}c_p\frac{\partial \tilde{T}}{\partial y} + \overline{\rho}\tilde{w}c_p\frac{\partial \tilde{T}}{\partial z} - \frac{\partial P}{\partial t} - \tilde{u}\frac{\partial P}{\partial x} - \tilde{w}\frac{\partial P}{\partial z} = \\ (\mu + \mu_t)\left(\left(\frac{\partial \tilde{u}}{\partial y}\right)^2 + \left(\frac{\partial \tilde{w}}{\partial y}\right)^2\right) + \frac{\partial}{\partial y}\left((k + k_t)\frac{\partial \tilde{T}}{\partial y}\right).\end{aligned} \tag{4.5.4}$$

The partial cross-derivatives $\frac{\partial \tilde{u}}{\partial z}$ and $\frac{\partial \tilde{w}}{\partial x}$ in the momentum equations are modeled by first order polynomials (see Eq. (4.4.11) and (4.4.12)) as in incompressible flow. The compressible continuity equation can be rewritten as

$$\frac{\partial \overline{\rho}}{\partial t} + \overline{\rho}\left(\frac{\partial \tilde{u}}{\partial x} + \frac{\partial \tilde{w}}{\partial z}\right) + \tilde{u}\frac{\partial \overline{\rho}}{\partial x} + \tilde{w}\frac{\partial \overline{\rho}}{\partial z} + \frac{\partial \overline{\rho}\tilde{v}}{\partial y} = 0, \tag{4.5.5}$$

where

$$\frac{\partial \overline{\rho}}{\partial x} = \frac{1}{RT}\frac{\partial P}{\partial x} - \frac{P}{RT^2}\frac{\partial \tilde{T}}{\partial x}. \tag{4.5.6}$$

We model only a near-wall part of the turbulent boundary layer, the streamwise temperature variation behaves like the variation of the wall temperature. The wall temperature T_w can be approximated by the total temperature T_t, whose deviation along the boundary layer can be neglected. Hence,

$$\frac{\partial \tilde{T}}{\partial x} \approx \frac{\partial \tilde{T}_w}{\partial x} \approx \frac{\partial \tilde{T}_t}{\partial x} \approx 0. \tag{4.5.7}$$

The same observation is valid for the spanwise direction, hence $\frac{\partial \tilde{T}}{\partial z} \approx 0$. The simplified version of the continuity equation in the integral form reads

$$(\overline{\rho}\tilde{v})(y) = \int_0^y -\frac{\partial \overline{\rho}}{\partial t} - \overline{\rho}\left(\frac{\partial \tilde{u}}{\partial x} + \frac{\partial \tilde{w}}{\partial z}\right) - \frac{\tilde{u}}{R\tilde{T}}\left(\frac{\partial P}{\partial x}\right)_{top} - \frac{\tilde{w}}{R\tilde{T}}\left(\frac{\partial P}{\partial z}\right)_{top} d\tilde{y}. \tag{4.5.8}$$

Using this equation with following quantities at the interface

$$(\overline{\rho}\tilde{v})_{top},$$
$$\left(\frac{\partial\tilde{u}}{\partial x}\right)_{top}, \quad \left(\frac{\partial^2\tilde{u}}{\partial x\partial y}\right)_{top},$$
$$\left(\frac{\partial w}{\partial z}\right)_{top}, \quad \left(\frac{\partial^2\tilde{w}}{\partial z\partial y}\right)_{top},$$

the derivatives $\frac{\partial\tilde{u}}{\partial x}$ and $\frac{\partial\tilde{w}}{\partial z}$ can be modeled as third and second order polynomials. The difference to incompressible case is that we require $(\overline{\rho}\tilde{v})_{top}$ instead of $\tilde{v}_{top}$, and the integral equation for $(\overline{\rho}\tilde{v})$ can not be analytically integrated since it depends on the field quantities like $\tilde{u}$ and $\tilde{w}$ that are solution of the wall model equations. Hence, the integration is performed numerically with the quantities from the previous iteration. There is the same split in systems with superscript ^{U} and ^{W} as in incompressible case. Exactly the same bounding and order reduction are applied. The compressible scaling factor is defined by

$$s^U = \frac{(\overline{\rho}\tilde{v})_{top}}{\int_0^{y_{top}} -\frac{\partial\overline{\rho}}{\partial t} - \overline{\rho}\left(\frac{\partial\tilde{u}}{\partial x} + \frac{\partial\tilde{w}}{\partial z}\right) - \frac{\tilde{u}}{R\tilde{T}}\left(\frac{\partial P}{\partial x}\right)_{top} - \frac{\tilde{w}}{R\tilde{T}}\left(\frac{\partial P}{\partial z}\right)_{top} d\tilde{y}}. \tag{4.5.9}$$

The polynomial coefficients for OTBLE_3 and OTBLE_2 are given in Appendix A.5 and A.6, respectively.
Since $\frac{\partial\tilde{T}}{\partial x}$ and $\frac{\partial\tilde{T}}{\partial z}$ are neglected, the internal energy equation reads

$$\overline{\rho}c_p\frac{\partial\tilde{T}}{\partial t} + \overline{\rho}\tilde{v}c_p\frac{\partial\tilde{T}}{\partial y} - \frac{\partial P}{\partial t} - \tilde{u}\frac{\partial P}{\partial x} - \tilde{w}\frac{\partial P}{\partial z} = (\mu+\mu_t)\left(\left(\frac{\partial\tilde{u}}{\partial y}\right)^2 + \left(\frac{\partial\tilde{w}}{\partial y}\right)^2\right) + \frac{\partial}{\partial y}\left((k+k_t)\frac{\partial\tilde{T}}{\partial y}\right). \tag{4.5.10}$$

It should be noted that the convection of the internal energy $e = c_pT - p/\rho$ is reduced but still exists in each direction: in the wall normal direction it is represented by the temperature gradient $\frac{\partial\tilde{T}}{\partial y}$ and in the wall-tangential directions by the pressure gradient $\frac{\partial P}{\partial x}$ and $\frac{\partial P}{\partial z}$.
Instead of solving the energy equation, an analytical approximation of the adiabatic wall temperature in the steady state

$$T_w \approx T_e + \frac{r}{2c_p}U_e^2 \tag{4.5.11}$$

can be extended for the near-wall region

$$\tilde{T}\left(\tilde{u}\left(y\right),\tilde{w}\left(y\right)\right) = \tilde{T}_{top} + \frac{r}{2c_p}\left(\tilde{u}_{top}^2 + \tilde{w}_{top}^2 - \tilde{u}^2\left(y\right) - \tilde{w}^2\left(y\right)\right) \tag{4.5.12}$$

with the turbulent recovery factor $r = \sqrt[3]{Pr_t}$. The momentum equations still have to be solved iteratively but the analytical internal energy equation might reduce the number of iterations needed for convergence.

5. Wall Model Implementation

The presented wall model is implemented as a boundary condition in the compressible multi-component flow solver INCA for performing large-eddy simulations with implicit turbulence modeling. The time advancement is realized with an explicit third order Runge Kutta scheme. The wall model routine is called every Runge-Kutta substep. In Section 5.1 an implementation of the incompressible wall model is described. Section 5.2 deals with an implementation of the compressible wall model.

5.1. Incompressible Wall Model

The wall model solution algorithm is given in the flowchart in Figure 5.1. The interface quantities U_{top}, W_{top}, V_{top}, $\left(\frac{\partial U}{\partial x}\right)_{top}$, $\left(\frac{\partial U}{\partial z}\right)_{top}$, $\left(\frac{\partial^2 U}{\partial x \partial y}\right)_{top}$, $\left(\frac{\partial W}{\partial x}\right)_{top}$, $\left(\frac{\partial W}{\partial z}\right)_{top}$ and $\left(\frac{\partial^2 W}{\partial z \partial y}\right)_{top}$ are computed (interpolated) at the interface by the LES flow solver and are given to the wall model routine. In the wall model routine, terms $\frac{\partial U}{\partial x}$, $\frac{\partial U}{\partial z}$, $\frac{\partial W}{\partial x}$, $\frac{\partial W}{\partial z}$ and V are computed since they do not depend on wall model solution of U and W. If the derivatives are out of bounds then the model reduction is performed. If $|U_{top}| \geq |W_{top}|$, the u-momentum equation is solved at first, then the w-momentum equation. The momentum equations are solved sequentially, therefore the updated quantities can be used to solve the next equation in order to speed up the convergence. The solution process is iterated as long the convergence criteria are not fulfilled or the maximum iteration number is reached. The maximum iteration number is equal to $max\,(50, 2N_{wm})$, where N_{wm} is the number of grid points in the wall model. If for any reason the convergence criteria are not satisfied after the iteration limit has been reached, the convective term is switched off, and the iteration process is repeated once again. After the iterative solution process, the wall shear stress is computed and supplied back to the LES flow solver. It should be noted that the wall shear stress is explicitly computed, i.e., it is computed from the velocity field in the previous iteration step. The momentum equation are discretized implicit in time

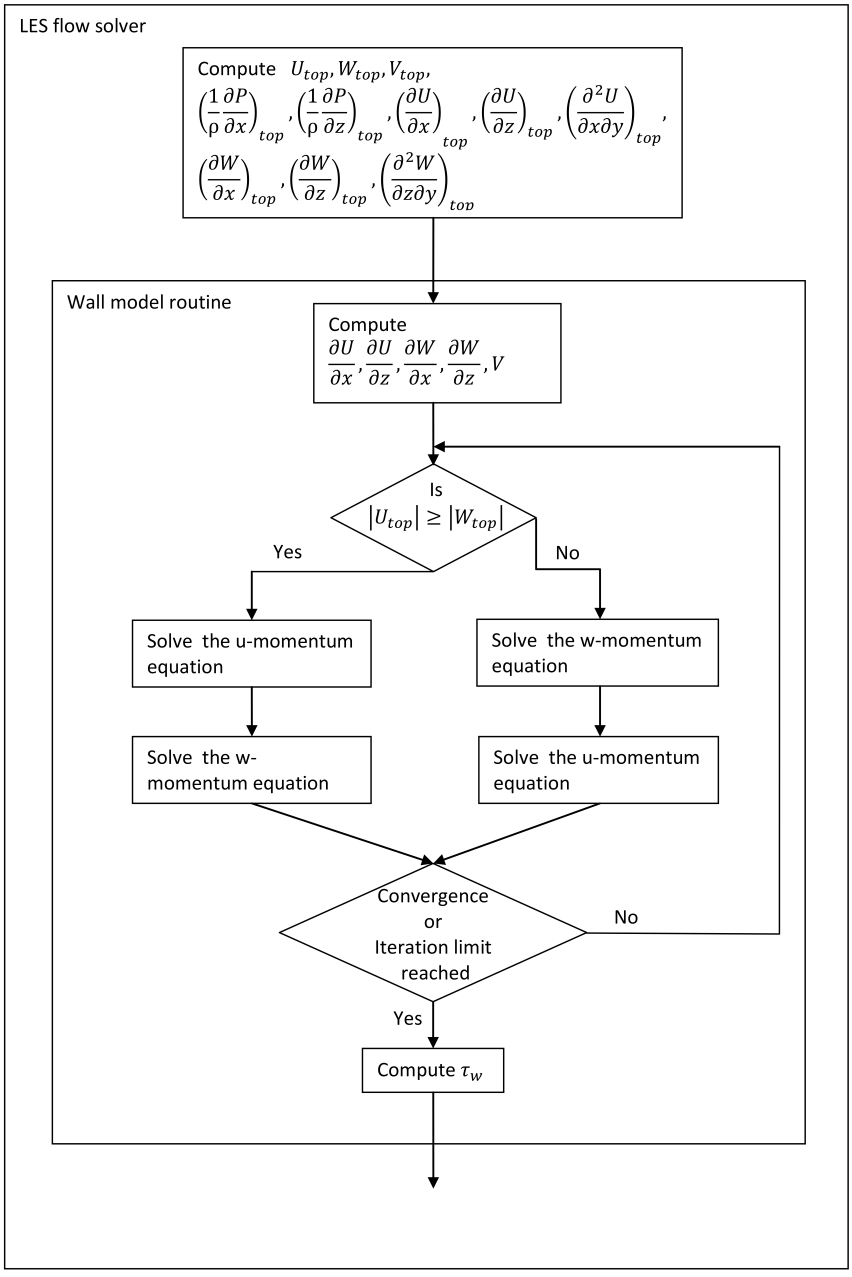

Figure 5.1.: Wall model solution algorithm for incompressible flow.

$$\frac{U^n - U^{n-1}}{\Delta t} + U^n \frac{\partial U}{\partial x} + V \frac{\partial U^n}{\partial y} + W^n \frac{\partial U}{\partial z} + \left(\frac{1}{\rho} \frac{\partial P}{\partial x} \right)_{top} = \frac{\partial}{\partial y} \left(\nu + \nu_t \right) \frac{\partial U^n}{\partial y}, \quad (5.1.1)$$

$$\frac{W^n - W^{n-1}}{\Delta t} + U^n \frac{\partial W}{\partial x} + V \frac{\partial W^n}{\partial y} + W^n \frac{\partial W}{\partial z} + \left(\frac{1}{\rho} \frac{\partial P}{\partial z} \right)_{top} = \frac{\partial}{\partial y} \left(\nu + \nu_t \right) \frac{\partial W^n}{\partial y}. \quad (5.1.2)$$

The superscript $^{(n-1)}$ denotes the stored quantities from the previous time step. The eddy viscosity and the coupling terms between the equations are updated after each iteration in the wall model routine. In space the equations are discretized with a central difference scheme of second order. Since the embedded mesh might be not equidistant, special finite difference formulas are required to account for nonuniform mesh, which are given in Appendix A.7. The central difference scheme of second order provides the tridiagonal system of equations. Hence, it can be easily solved using the Thomas algorithm, that gives converges after two iterations. The only one convergence issue is dependency of the eddy viscosity on the wall shear stress. The system of equations can be split rearranged in following form

$$L_v(i)\phi(i+1) + D_v(i)\phi(i) + U_v(i)\phi(i-1) = S_v(i) \quad \text{with } i = 0, 2, ..., N_{wm}, \quad (5.1.3)$$

where ϕ is the solution vector; $L_v(i)$, $D_v(i)$ and $U_v(i)$ are the lower diagonal, diagonal and upper diagonal vectors; $S(i)$ is the source vector. For the solution vector $U(i)$ with boundary conditions $U(0) = 0$, $U(N_{wm}) = U_{top}$; $L_v(i)$, $D_v(i)$, $U_v(i)$, $S_v(i)$ read

$$i = 0 : \quad (5.1.4)$$

$$L_v(1) = 0, \quad D_v(1) = 1, \quad U_v(1) = 0, \quad S_v(1) = 0. \quad (5.1.5)$$

$$i = 2, .., N_{wm} - 1 : \quad (5.1.6)$$

$$L_v(i) = \frac{2\left(\nu + \nu_t(i)\right)}{\left(\alpha(i) + 1\right) h(i)^2} - \left(\frac{d\nu_t}{dy}(i) - V(i) \right) \frac{\alpha(i)}{\left(\alpha(i) + 1\right) h(i)}, \quad (5.1.7)$$

$$D_v(i) = \frac{-1}{\Delta t} - \frac{\partial U}{\partial x}(i) - \frac{2\left(\nu + \nu_t(i)\right)}{\alpha(i) h(i)^2} + \left(\frac{d\nu_t}{dy}(i) - V(i) \right) \frac{\alpha(i) - 1}{\alpha(i) h(i)}, \quad (5.1.8)$$

$$U_v(i) = \frac{2\left(\nu + \nu_t(i)\right)}{\alpha(i)\left(\alpha(i) + 1\right) h(i)^2} + \left(\frac{d\nu_t}{dy}(i) - V(i) \right) \frac{1}{\alpha(i)\left(\alpha(i) + 1\right) h(i)}, \quad (5.1.9)$$

$$S_v(i) = \frac{-U^{n-1}(i)}{\Delta t} + \left(\frac{1}{\rho} \frac{\partial P}{\partial x} \right)_{top} + W(i) \frac{\partial U}{\partial z}(i). \quad (5.1.10)$$

$$i = N_{wm} : \quad (5.1.11)$$

$$L_v(N_{wm}) = 0, \quad D_v(N_{wm}) = 1, \quad U_v(N_{wm}) = 0, \quad S_v(N_{wm}) = U_{top}. \quad (5.1.12)$$

The grid spacing is given by

$$h(i) = y(i) - y(i-1), \quad (5.1.13)$$

and the growth rate by

$$\alpha(i) = \frac{h(i+1)}{h(i)}. \tag{5.1.14}$$

The equations given in this section account for the variable grid growth rate $\alpha(i)$. In case of the uniform mesh $\alpha = 0$ and $h = const$.

5.2. Compressible Wall Model

The wall model solution algorithm is given in the flowchart in Figure 5.2. The interface quantities $\tilde{u}_{top}$, $\tilde{w}_{top}$, $(\overline{\rho}\tilde{v})_{top}$, $\left(\frac{\partial\tilde{u}}{\partial x}\right)_{top}$, $\left(\frac{\partial\tilde{u}}{\partial z}\right)_{top}$, $\left(\frac{\partial^2\tilde{u}}{\partial x\partial y}\right)_{top}$, $\left(\frac{\partial\tilde{w}}{\partial x}\right)_{top}$, $\left(\frac{\partial\tilde{w}}{\partial z}\right)_{top}$ and $\left(\frac{\partial^2\tilde{w}}{\partial z\partial y}\right)_{top}$ are computed (interpolated) at the interface by the LES flow solver and given to the wall model routine. In the wall model routine, terms $\frac{\partial\tilde{u}}{\partial z}$ and $\frac{\partial\tilde{w}}{\partial x}$ are computed at first since they do not depend on wall model solution fields. $\frac{\partial\tilde{u}}{\partial x}$, $\frac{\partial\tilde{w}}{\partial z}$ and $\overline{\rho}\tilde{v}$ are computed in the iterative process since they depend on solution fields $\tilde{u}$, $\tilde{w}$, $\tilde{T}$ and $\overline{\rho}$. If the derivatives $\frac{\partial\tilde{u}}{\partial x}$ and $\frac{\partial\tilde{w}}{\partial z}$ are out of bounds then the model reduction is performed. If $|\tilde{u}_{top}| \geq |\tilde{w}_{top}|$, the u-momentum equation is solved at first, then the w-momentum equation following by the energy equation (or analytical formula for the temperature field). The equations are solved sequentially, therefore the updated quantities can be used to solve the next equation in order to speed up the convergence. Then, the density field is updated using the equation of state. The solution process is iterated as long the convergence criteria are not fulfilled or the maximum iteration number is reached. If for any reason the convergence criteria are not satisfied after the iteration limit has been reached then the convective term is switched off, and the iteration process is repeated once again. After the iterative solution process, the wall shear stress is computed and supplied back to the LES flow solver. The time, space discretization and the tridiagonal solver are the same as in the incompressible case. The L_v, D_v, U_v, S_v vectors are given for the momentum equation in the streamwise direction:

$i = 0$:

$$L_v(1) = 0, \quad D_v(1) = 1, \quad U_v(1) = 0, \quad S_v(1) = 0. \tag{5.2.1}$$

$i = 2, .., N_{wm} - 1$:

$$L_v(i) = \frac{2\left(\mu(i) + \mu_t(i)\right)}{(\alpha(i)+1)\,h(i)^2} - \left(\frac{d(\mu+\mu_t)}{dy}(i) - (\overline{\rho}\tilde{v})(i)\right)\frac{\alpha(i)}{(\alpha(i)+1)\,h(i)}, \tag{5.2.2}$$

$$D_v(i) = \frac{-\overline{\rho}(i)}{\Delta t} - \overline{\rho}(i)\frac{\partial \tilde{u}}{\partial x}(i) - \frac{2\left(\mu(i) + \mu_t(i)\right)}{\alpha(i)h(i)^2} + \left(\frac{d(\mu+\mu_t)}{dy}(i) - (\overline{\rho}\tilde{v})(i)\right)\frac{\alpha(i)-1}{\alpha(i)h(i)}, \tag{5.2.3}$$

$$U_v(i) = \frac{2\left(\mu(i) + \mu_t(i)\right)}{\alpha(i)\,(\alpha(i)+1)\,h(i)^2} + \left(\frac{d(\mu+\mu_t)}{dy}(i) - (\overline{\rho}\tilde{v})(i)\right)\frac{1}{\alpha(i)\,(\alpha(i)+1)\,h(i)}, \tag{5.2.4}$$

$$S_v(i) = \frac{-\overline{\rho}(i)\tilde{u}^{n-1}(i)}{\Delta t} + \left(\frac{\partial P}{\partial x}\right)_{top} + \overline{\rho}(i)\tilde{w}(i)\frac{\partial \tilde{u}}{\partial z}(i). \tag{5.2.5}$$

$i = N_{wm}$:

$$L_v(N_{wm}) = 0, \quad D_v(N_{wm}) = 1, \quad U_v(N_{wm}) = 0, \quad S_v(N_{wm}) = \tilde{u}_{top}. \tag{5.2.6}$$

and for the energy equation with an adiabatic wall:

$i = 0$:

$$L_v(1) = 0, \quad D_v(1) = 1, \quad U_v(1) = -1, \quad S_v(1) = 0. \tag{5.2.7}$$

$i = 2, .., N_{wm} - 1$:

$$L_v(i) = \frac{-2\left(k(i) + k_t(i)\right)}{(\alpha(i)+1)\,h(i)^2} - \left(\frac{-d(k+k_t)}{dy}(i) + (\overline{\rho}\tilde{v})(i)c_p\right)\frac{\alpha(i)}{(\alpha(i)+1)\,h(i)}, \tag{5.2.8}$$

$$D_v(i) = \frac{\overline{\rho}(i)c_p}{\Delta t} + \frac{2\left(k(i) + k_t(i)\right)}{\alpha(i)h(i)^2} + \left(\frac{-d(k+k_t)}{dy}(i) - (\overline{\rho}\tilde{v})(i)c_p\right)\frac{\alpha(i)-1}{\alpha(i)h(i)}, \tag{5.2.9}$$

$$U_v(i) = \frac{-2\left(k(i) + k(i)\right)}{\alpha(i)\,(\alpha(i)+1)\,h(i)^2} + \left(\frac{-d(k+k_t)}{dy}(i) + (\overline{\rho}\tilde{v})(i)c_p\right)\frac{1}{\alpha(i)\,(\alpha(i)+1)\,h(i)}, \tag{5.2.10}$$

$$S_v(i) = \frac{\overline{\rho}(i)c_p\tilde{T}^{n-1}(i)}{\Delta t} + \frac{P^n(i) - P^{n-1}(i)}{\Delta t} + \tilde{u}(i)\left(\frac{\partial P}{\partial x}\right)_{top} + \tilde{w}(i)\left(\frac{\partial P}{\partial z}\right)_{top}$$
$$+ \left(\mu(i) + \mu_t(i)\right)\left(\left(\frac{\partial \tilde{u}}{\partial x}(i)\right)^2 + \left(\frac{\partial \tilde{w}}{\partial z}(i)\right)^2\right). \tag{5.2.11}$$

$i = N_{wm}$:

$$L_v(N_{wm}) = 0, \quad D_v(N_{wm}) = 1, \quad U_v(N_{wm}) = 0, \quad S_v(N_{wm}) = \tilde{T}_{top}. \tag{5.2.12}$$

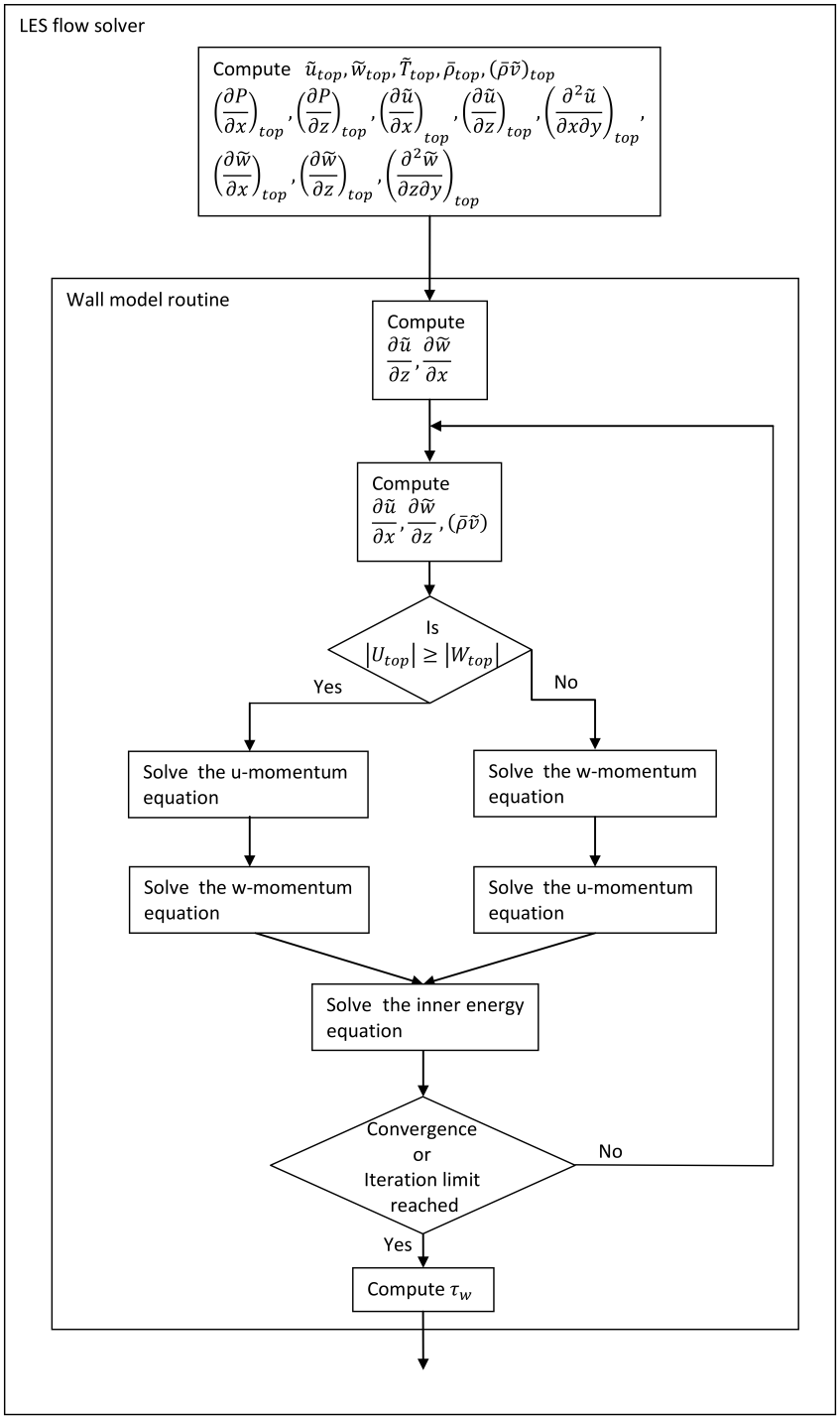

Figure 5.2.: Wall model solution algorithm for compressible flow.

6. Wall Model Validation

In this chapter the developed wall model is validated. At first, a stand-alone steady wall model simulation is performed with the interface quantities supplied by the APGTBL database, which has been already used in Sections 4.3 and 4.4.
Then, the wall model is validated by running WMLES. Turbulence subgrid-scale term is modeled with the adaptive local deconvolution method proposed by Hickel *et al.* [23]. For time advancement, an explicit third-order Runge-Kutta scheme is used. All simulations are performed with CFL= 1. For incompressible simulations the filtered incompressible Navier-Stokes equations are discretized on a staggered Cartesian mesh. The Poisson equation for pressure and diffusive terms are discretized by second order centered difference schemes. The Poisson equation is solved at every Runge-Kutta step.
First large-eddy simulations with wall modeling are performed for a turbulent channel flow. After that, the wall model is studied for compressible flow by performing simulations of a shock/turbulent boundary layer interaction.

6.1. Stand-Alone Wall Model Simulation

6.1.1. Wall Model Comparison

The wall model with 200 uniform cells is applied on the APGTBL as post processing tool using the averaged data from database [21] at the interface. The model affects only the velocity below the interface and thus, the wall shear stress. These quantities can be compared to the velocity profile and wall shear stress of the reference LES. The database contains only time averaged quantities, hence the wall model solves the steady TBLE.
In the steady APGTBL case the difference between different convective term models can be seen if we take the eddy viscosity computed from the unresolved term in the database[1]. Then, there are no modeled terms except of the convective term. Hence, the eddy viscosity and convective models do not interfere. Figure 6.1 shows the relative error in the friction coefficient $C_{f,wm}/C_{f,LES} - 1$ with the interface at $y_{top} = 0.1\delta_0$ and $y_{top} = 0.2\delta_0$, where $\delta_0 = 12.64\ mm$.

[1] As mentioned in section 4.3, the unresolved term also contains modeling and numerical errors.

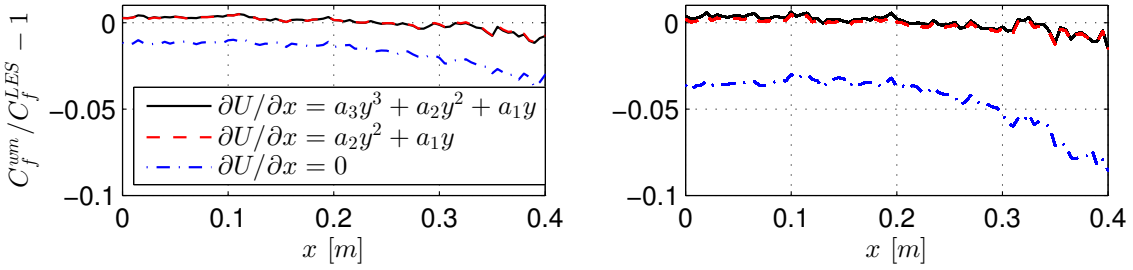

Figure 6.1.: APGTBL, error in the friction coefficient supplied by the wall model relative to the reference LES. (a) the wall model interface at $y_{top} = 0.1\delta_0$, (b) $y_{top} = 0.2\delta_0$.

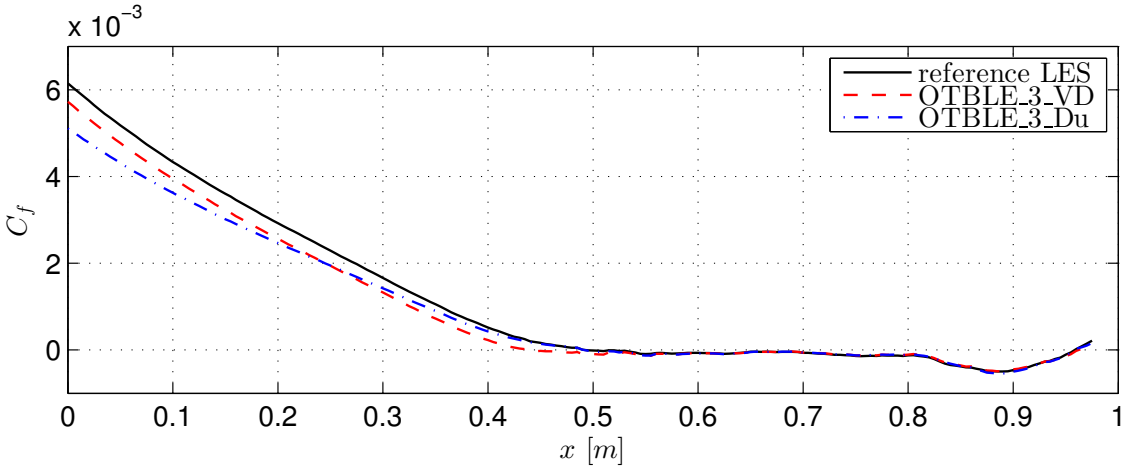

Figure 6.2.: APGTBL, wall friction coefficient. The wall model interface at $y_{top} = 0.1\delta_0$.

The skin friction coefficient is defined by

$$C_f = \frac{2\tau_w}{\rho_0 U_0}. \tag{6.1.1}$$

The relative error is a useful quantity only in the attached flow region between $x = 0\ m$ and $x < 0.5\ m$. Both convective term models have comparable relative error that is estimated to be less than 0.01, whereas the model without the convective term has an error of 0.02 in average for $y_{top} = 0.1\delta_0$ and 0.05 for $y_{top} = 0.2\delta_0$, respectively. Neglecting the convective term leads to underestimation of C_f in the turbulent boundary layer. Even if the eddy viscosity is perfectly estimated, the skin friction coefficient can be estimated only with an error around $2\% - 5\%$.
The importance of the eddy viscosity model is also investigated. The skin friction coefficient, calculated with the van Driest and Duprat eddy viscosity models, is shown in Figure 6.2. In both cases the convective term is modeled as third order polynomial, the interface is set to $y_{top} = 0.1\delta_0$. The van Driest eddy viscosity is

superior to Duprat eddy viscosity in the developed turbulent boundary layer and the Duprat model is better close to the separation point. Hence, the separation point is better predicted by the Duprat model than by the van Driest eddy viscosity. Nevertheless, both models underestimate the friction coefficient. The relative error in the friction coefficient is shown in Figure 6.3. The relative error is roughly one

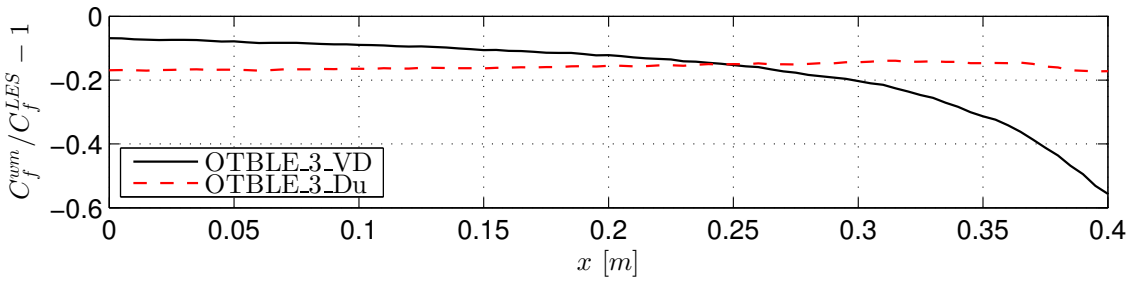

Figure 6.3.: APGTBL, error in the friction coefficient supplied by the wall model relative to the reference LES. The wall model interface at $y_{top} = 0.1\delta_0$.

order of magnitude larger than that of the convective term alone. The error in the eddy viscosity is dominant, hence the eddy viscosity modeling is still of paramount importance, even if the wall model accounts for other terms. The streamwise velocity profiles are shown in Figure 6.4. The velocity profile is somewhat controversial. The

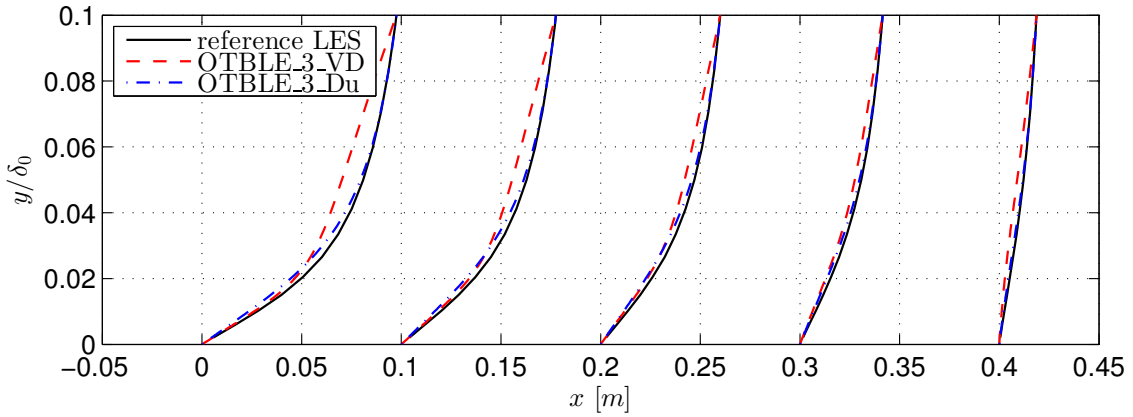

Figure 6.4.: APGTBL, mean velocity profiles. The wall model interface at $y_{top} = 0.1\delta_0$.

wall model with the van Driest eddy viscosity model yields better prediction of the friction coefficient close to the inlet. Nevertheless, the velocity profile does not match the LES profile in the middle of the modeled region. The Duprat model fits the velocity profile reasonably well. The reason for that is illustrated in Figure 6.5. The eddy viscosities are shown at $x = 0.1\ m$. The Duprat model approximates the eddy viscosity at $y^+ > 15$ better than the van Driest model. Whereas, the van Driest model is better in the buffer region and viscous sublayer at $y^+ < 15$, therefore it

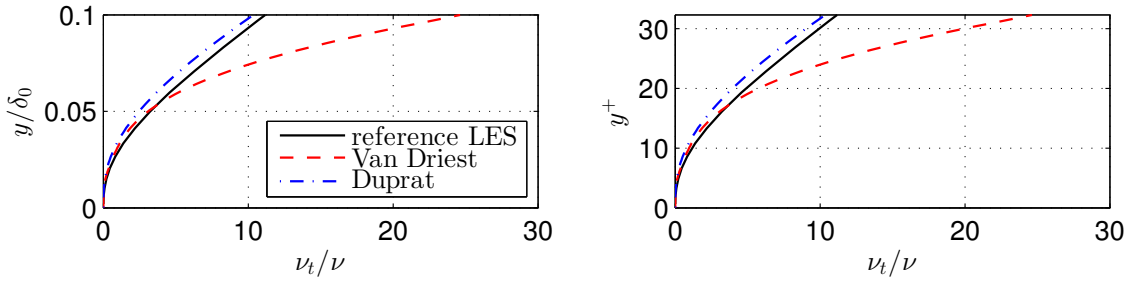

Figure 6.5.: APGTBL, eddy viscosity at $x = 0.1\ m$. (a) the wall distance scaled with δ_0, (b) the wall distance in wall units.

predicts better the friction coefficient. Since it is an a posteriori test, the velocity at the interface is fixed, thus both models match U_{top}. The importance of the correct velocity profile should be not underestimated. The velocity mismatch region is a sign that the model might interfere the LES in the real simulation when the model and the main computational domain are coupled.
It should be pointed out that the LES eddy viscosity is computed from the unresolved term in the time averaged database. That means it also accounts for the TBL approximation errors and numerical errors. As a consequence, the eddy viscosity error can be smaller than estimated but the eddy viscosity modeling is still the most important issue. Several other algebraic and one equation eddy viscosity models were tested such as Cebeci-Smith model, Baldwin-Lomax model, 1/2-Equation model[2]. None of these models could show better results than van Driest and Duprat eddy viscosity models.

6.1.2. Wall Model Grid Convergence Study

OTBLE model solves a set of ordinary differential equations on a one-dimensional mesh. It is important that the wall model does not introduce additional numerical errors in the simulation. Hence, the wall model grid should be fine enough to minimize numerical errors and, in the same time, it should have as few nodes as possible to minimize computational cost. The effect of the uniform grid resolution on the friction coefficient C_f is shown in Figure 6.6. The friction coefficient is evaluated at $x = 0.1\ m$. This position suits well for the convergence study, since the C_f is high and the convective term in the TBLE is non zero. According to the figure, the uniform mesh with at least 60 and 120 grid points for $y_{top} = 0.1\delta_0$ and $y_{top} = 0.2\delta_0$, respectively, has acceptable numerical error. This wall resolution corresponds to spacing $(\Delta^+)_{uniform} = 0.5$ in wall units with $l^+ = 0.02\ m$. Such a fine resolution is needed to resolve the inner layer. The outer layer can be coarser. Therefore, the

[2]These models can be found in Wilcox [10].

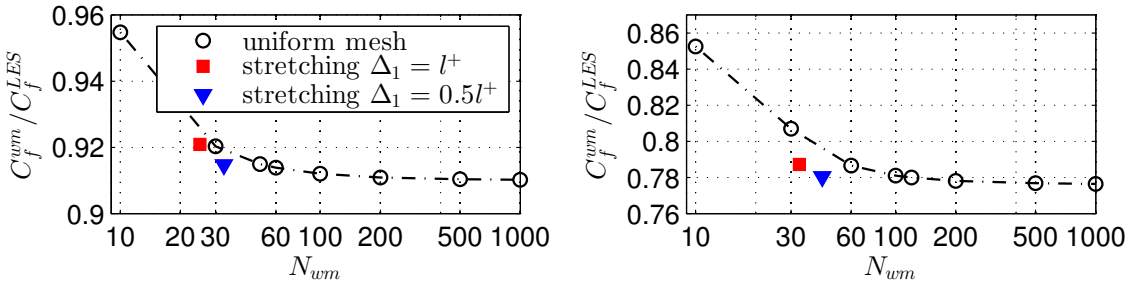

Figure 6.6.: APGTBL, effect of the wall model resolution on the friction coefficent at $x = 0.1\ m$. (a) the wall model interface at $y_{top} = 0.1\delta_0$, $y_{top} = 0.2\delta_0$.

stretching with fixed growth rate α is applied. The recursive definition is given by

$$\frac{y_i}{y_1} = \sum_{j=0}^{j=i} \alpha^j = \frac{1-\alpha^i}{1-\alpha}, \quad \text{with } i \geq 2 \tag{6.1.2}$$

This inflation has an advantage that the height of the first cell y_1 and the growth rate α can be directly adjusted. y_1 and α are defined such that three conditions are satisfied:

$$(1) \quad \frac{y_1}{l^+} \leq 0.5, \tag{6.1.3}$$

$$(2) \quad k \leq 1.2, \tag{6.1.4}$$

$$(3) \quad \frac{y_N - y_{N-1}}{y_{top}} \leq 0.05. \tag{6.1.5}$$

These restrictions are motivated by the physical structure of the boundary layer. The size of the cell at the wall is limited in wall units; the size of cell at the interface is limited by the height of the wall model; and the growth rate is responsible for the smooth transition. Figure 6.6 shows that stretched grids with $y_1 = l^+$ and $y_1 = 0.5l^+$ have the same accuracy as the uniform grids with $(\Delta^+)_{uniform} = 1$ and $(\Delta^+)_{uniform} = 0.5$, respectively. For all further simulations the stretched grid with $y_1 = 0.5l^+$ is chosen.

6.1.3. Summary

This stand-alone test case has shown that the modeling of the convective term improves the the prediction of the near-wall flow field and hence, it improves the estimation of the wall shear stress. The quality of the eddy viscosity model is of paramount importance for the calculation of τ_w.
The wall model equations converge on a uniform grid with $(\Delta^+)_{uniform} = 0.5$. Grid stretching can be applied maintaining resolution at the wall $y_1 = 0.5l^+$.
The wall model was fitted by time averaged well resolved quantities. In following

sections the wall model is tested on time dependent simulations, where LES and the wall model are coupled.

6.2. Turbulent Channel Flow

In this section, the OTBLE model is investigated in a turbulent channel flow, which is abbreviated as TCF throughout. Results are compared to the reference DNS of Alamo et al. [24]. We consider the case with nominal $Re_\tau = 950$, the flow is driven by a mean pressure gradient that is controlled to maintain a constant mass flow corresponding to $Re_{bulk} = 20580$. The Reynolds number is based on the channel half height.

6.2.1. Computational Setup

The computational domain has the extent $2\pi H \times 2H \times \pi H$ in the streamwise, wall-normal and spanwise directions. The channel half height is $H = 1$, the mass averaged (bulk) velocity is $U_{bulk} = 1$, the kinematic viscosity is $\nu = 1/Re_{bulk}$. Periodic boundary conditions are imposed in the streamwise and spanwise directions. Using the definition of the Reynolds number based on the friction velocity, the viscous length scale is given by

$$l^+ = \frac{\nu}{U_\tau} = \frac{H}{Re_\tau} \approx 0.001. \tag{6.2.1}$$

The grid resolution is motivated by [25], where LES-NWR was performed on a grid with $128 \times 128 \times 128$ cells. The computational grid parameters of the reference LES are given in Table 6.1. The computational domain is stretched is the wall-

Streamwise direction	$L_x = 2\pi H$	$N_x = 128$	$\Delta_x^+ = 46.6$
Wall-normal direction	$L_y = 2H$	$N_y = 128$	$\Delta_{y,min}^+ = 1.5$ $\Delta_{y,max}^+ = 33.7$ $\Delta_{y,avg}^+ = 14.8$
Spanwise direction	$L_z = \pi H$	$N_z = 128$	$\Delta_z^+ = 23.3$

Table 6.1.: TCF at $Re_\tau = 950$, grid for LES-NWR.

normal direction using a hyperbolic tangent function in order to increase resolution in vicinity of the walls. If the wall model is applied, there is no need for the grid stretching. The computational grid should be fine enough to resolve the length scales of the flow in the middle region of the channel. This requirement gives the constraint for the wall-normal resolution $\Delta_y^+ \leq \Delta_{y,max}^+ = 33.7$, i.e., $N_y \geq 56$ for a uniform mesh. Resolutions in all directions are related. If resolution in the wall-normal direction is reduced then it can be reduced in the other directions too. The

relation $\Delta_x^+ : \Delta_y^+ : \Delta_z^+$ is assumed to be approximately $2 : 1 : 1$ for the TCF. This assumption follows from comparison of Δ_x^+, $\Delta_{y,avg}^+$ and Δ_z^+ in the reference LES from Table 6.1. The last constraint is the height of the wall model, which is typically around $0.1\delta_{ref}$. These considerations are valid for any flat wall bounded flow case and, they are summarized in one decision algorithm, which is shown in Figure 6.7.

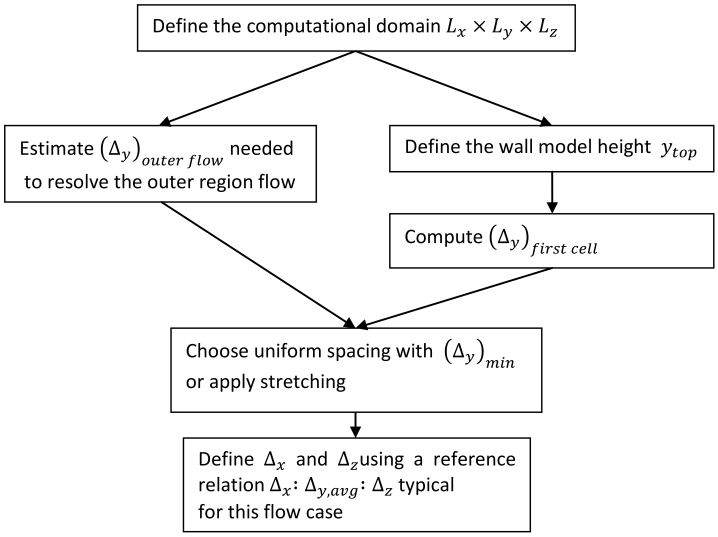

Figure 6.7.: Decision algorithm for determination of the WMLES grid resolution.

6.2.2. Interface Location

OTBLE model requires mean velocity fields and their derivatives as input at the interface. It is of paramount importance that the input data contains as less errors as possible. It is important from which of the first few off-wall cells the input for wall model is taken. In this section we consider OTBLE models with the interface at the first to the fourth LES off-wall cell. Since the grid is staggered, it is not possible to choose a position within the cell, where u, w and v are accessible without interpolation. The interface is set to the center of LES cell, since the continuity equation is fulfilled there. In the cell center, $\partial U/\partial x$ and $\partial W/\partial z$ are computed most precisely.
Simulations are performed on uniform grid with resolution $90 \times 56 \times 90$ and $108 \times 70 \times 108$. The first resolution was chosen such that $\Delta_y^+ \approx \left(\Delta_{y,max}^+\right)_{LES-NWR}$. The latter resolution sets the model height $y_{mw} = 0.1\delta = 0.1H$ in the center of the forth off-wall cell. Both grids are shown in Tables 6.3 and 6.3. The wall model is OTBLE_3_VD. The velocity profiles on both grids, coarse and fine, are shown in Figures 6.8 and 6.9, respectively. WMLES with the interface at the first cell reproduce the DNS velocity profile poorly in the vicinity of the wall. Other models are in agreement with the DNS velocity profile except of the first few cells at wall.

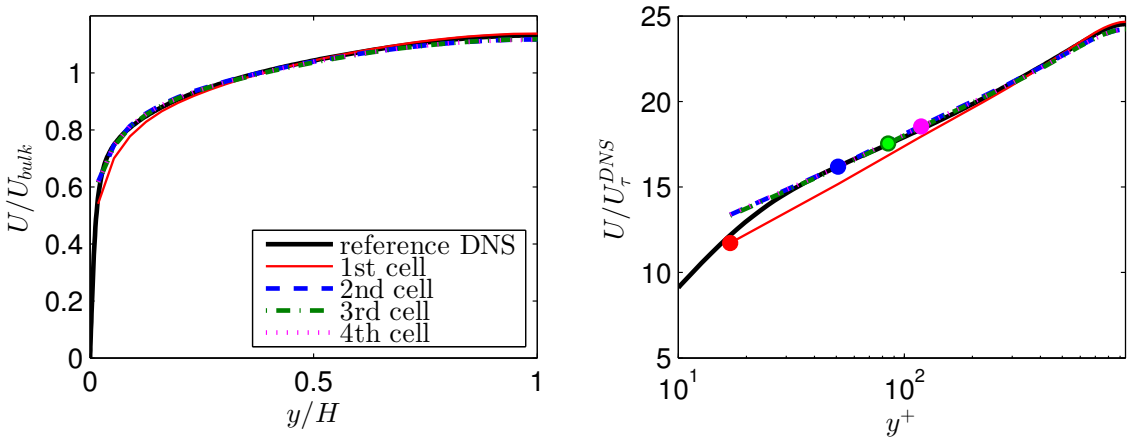

Figure 6.8.: TCF, mean velocity profiles. DNS of Alamo *et al*, LES with resolution $90\times56\times90$ with OTBLE_3_VD wall model, interface in the fist to fourth off-wall LES cell. Filled circles indicate the interface between LES and the wall model.

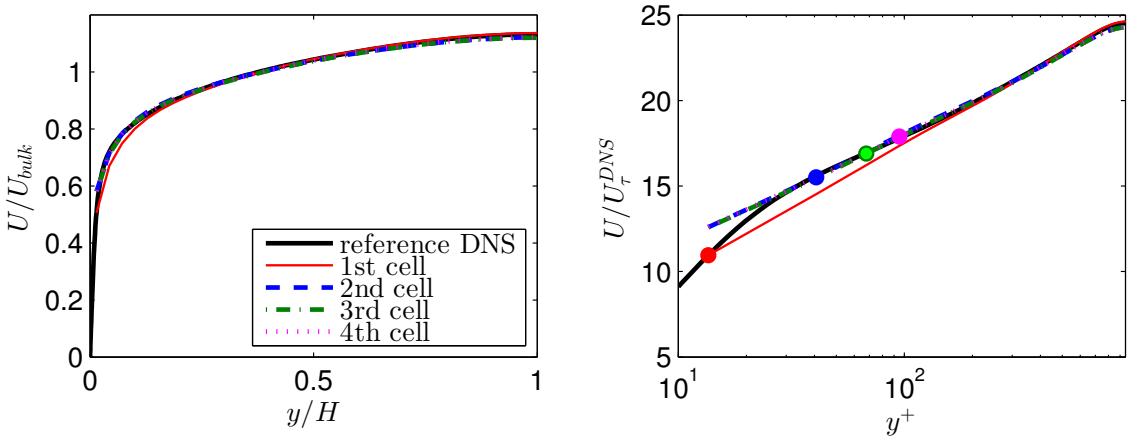

Figure 6.9.: TCF, mean velocity profiles. DNS of Alamo *et al*, LES with resolution $108\times70\times108$ with OTBLE_3_VD wall model, interface in the fist to fourth off-wall LES cell. Filled circles indicate the interface between LES and the wall model.

Streamwise direction	$L_x = 2\pi H$	$N_x = 90$	$\Delta_x^+ = 66.3$
Wall-normal direction	$L_y = 2H$	$N_y = 56$	$\Delta_y^+ = 33.9$
Spanwise direction	$L_z = \pi H$	$N_z = 128$	$\Delta_z^+ = 33.2$

Table 6.2.: TCF at $Re_\tau = 950$, grid $90 \times 56 \times 90$ for WMLES.

Streamwise direction	$L_x = 2\pi H$	$N_x = 90$	$\Delta_x^+ = 55.3$
Wall-normal direction	$L_y = 2H$	$N_y = 56$	$\Delta_y^+ = 17.6$
Spanwise direction	$L_z = \pi H$	$N_z = 128$	$\Delta_z^+ = 27.6$

Table 6.3.: TCF at $Re_\tau = 950$, grid $108 \times 70 \times 108$ for WMLES.

That behavior is common for all WMLES with the interface higher than the first cell. It can be explained with Figure 6.10. The figure shows the LES velocity profile and the wall model velocity profile of the simulation on grid $90 \times 56 \times 90$ with the interface at the fourth off-wall cell. The wall model velocity is equal to the velocity at the LES cell at the interface, but below the interface LES cells and the model do not match. The wall model velocity profile fits reasonably well with DNS profile, but velocity at LES cells does not. LES is underresolved near the wall, i.e., it can not follow the wall model velocity profile and consequently, the DNS velocity profile. To decide which model is better we consider the friction velocity supplied by the wall model. The friction velocity for WMLES on both grids, $90 \times 56 \times 90$ and $108 \times 70 \times 108$, is shown in Figure 6.11. The first off-wall cell does not suit for the wall model interface. The other cells are suitable since they yield friction velocities that are by far better than the first cell. There are two reasons why the interface should not be too close to the wall and, in the same time, not too far from it. If the interface is too close to the wall then the input for the model is taken form the under-resolved cells, i.e., the input quantities, velocities and their derivatives, are inaccurate[3]. For that reason WMLES with the interface at the first cell yields a spurious result. In TCF the convective term is negligible[4]. Thus, the accuracy of $\left(\frac{\partial U}{\partial x}\right)_{top}$ and $\left(\frac{\partial W}{\partial z}\right)_{top}$ is not relevant. The major part of the error is due to interpolation of U and V on the staggered grid. The other constraint is the accuracy of the eddy viscosity model and the convective term model away from the wall. The closer to the wall the cell is, the more precise are the models. Unfortunately, this effect can not be seen in TCF at this resolution: the convective term is negligible and the van Driest eddy viscosity model yields excellent results for TCF since the velocity profile follows the law of the wall. In complex flows the efficiency of the eddy viscosity model can be strongly reduced, e.g., in APGBL the van Driest eddy viscosity might be already inaccurate for $y^+ > 20$ (see Figure 6.5). For that reason the second off-wall LES cell is chosen for the wall model interface for all further simulations.

[3]Kawai and Larsson have studied errors in the LES in the first few grid points off the wall in [26].

[4]In section 6.2.3 it is shown that wall model with the convective term yields the same result as the model without it.

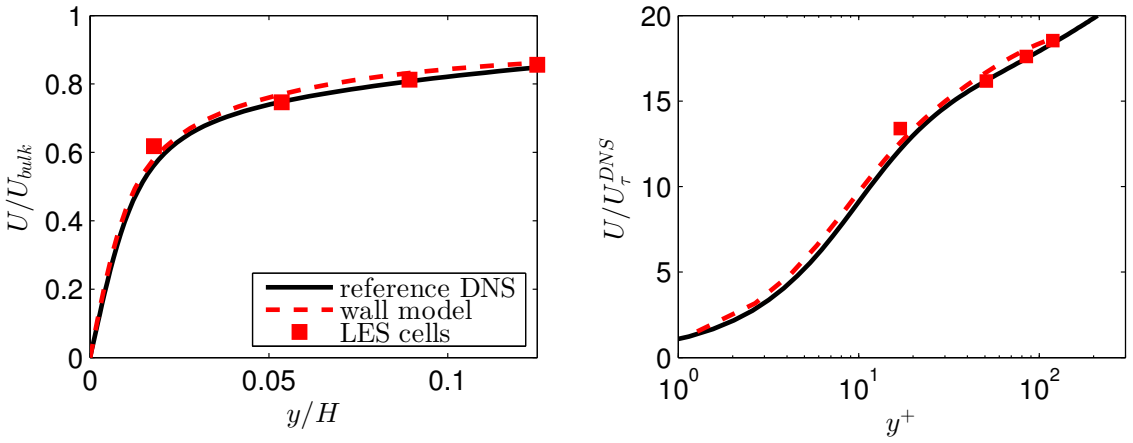

Figure 6.10.: TCF, wall model velocity profiles for turbulent channel flow. DNS of Alamo *et al*, LES with resolution $90 \times 56 \times 90$ with OTBLE_3_VD wall model, interface at fourth off-wall LES cells.

It should be noted that choosing the cell upon the first off-wall cell for the wall model interface introduces the "velocity mismatch" at all LES cells beyond the interface. As a consequence, these cells should be excluded from any velocity profile analysis as if these cells do not exist. The mismatch can be prevented only if LES has the near-wall resolution. Furthermore, wall shear stress computed from the first off-wall cell does not have any physical meaning or, at least, does not have anything to do with the real wall shear stress that is provided by the wall model. Only if WMLES has near-wall resolution, both quantities are equal.

6.2.3. Wall Model Comparison

In this section we compare TCF simulations with different wall models. The simulations are performed on uniform grid $90 \times 56 \times 90$ with $y_{top} = 0.054H$. In steady turbulent channel flow the convective term can be neglected. OTBLE models with convective term and without it yield the same results for the time averaged velocity profile and friction velocity. It has two consequences. First of all, if the time averaged quantities of a flow are of interest and if the time averaged convection can be neglected then there is no need to model the convective term for this type of simulation. The second important consequence is that the modeled convective term does not lead to spurious results, i.e., the modeled convective term is zero where it should be zero. In this section the wall models OTBLE_3_VD, OTBLE_2_VD, OTBLE_0_VD are referred to as OTBLE_VD and all models with the Duprat eddy viscosity are referred to as OTBLE_Du, respectively. Simulations with OTBLE models are compared to the simulation with the generalized wall function (GWF) model, to the simulation without any wall model on grid $90 \times 56 \times 90$ and $120 \times 120 \times 120$. The

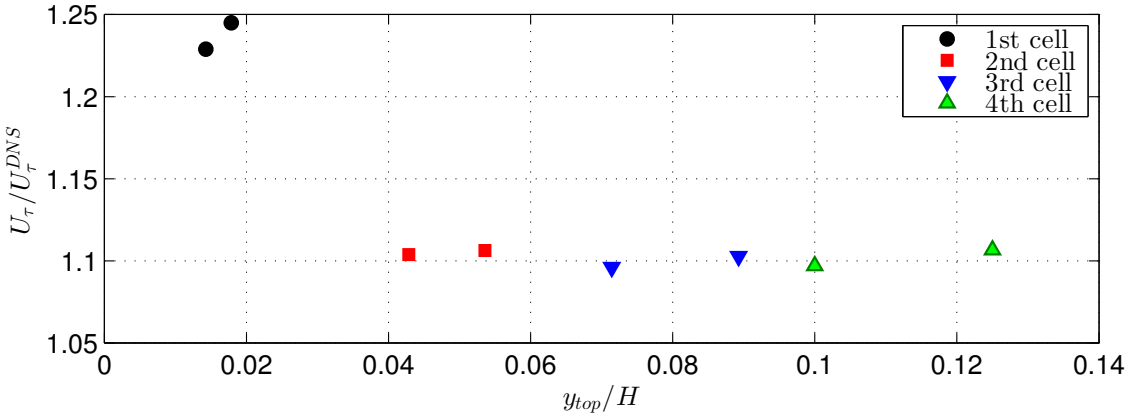

Figure 6.11.: TCF, friction velocity scaled with DNS reference value. For each interface location, two simulations on grid $90 \times 56 \times 90$ and $108 \times 70 \times 108$.

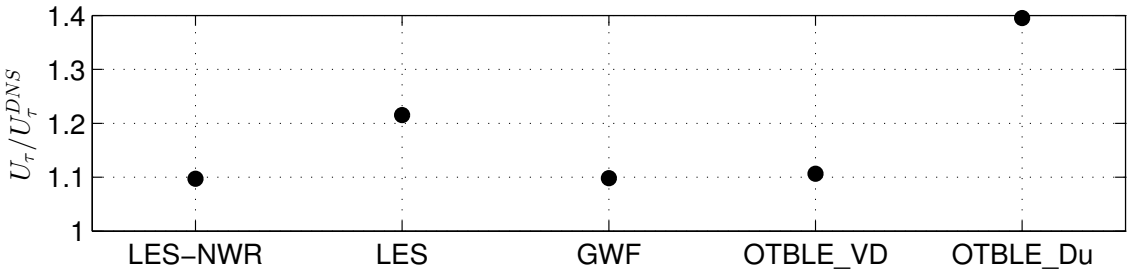

Figure 6.12.: TCF, friction velocity scaled with the DNS reference value. LES-NWR on grid $120 \times 120 \times 120$, other LES simulations on grid $90 \times 56 \times 90$.

latter simulation is a reproduction of LES-NWR [25], which can be considered as fully resolved. The friction velocities scaled with the DNS reference value are shown in Figure 6.12. All performed large-eddy simulations overestimate the friction velocity. The LES-NWR friction velocity deviates from the DNS value around 10%. The OTBLE_VD on a coarse grid fulfills its objective and reproduces quite well the wall friction of the LES-NWR. GWF also yields the wall friction comparable to LES-NWR. GWF was derived from the law of the wall, which is valid for turbulent channel flow. Hence, the GWF is the most suitable for such cases. The LES without wall modeling on a coarse grid and OTBLE_Du yield the highest deviation from the DNS friction velocity. The inaccuracy of LES on a coarse grid is predictable, but the inaccuracy of the OTBLE_Du is not so obvious. It is explained later by means of the velocity profile. At first, we look at time averaged velocity profiles of simulations with the GWF and OTBLE_VD models in Figure 6.13. These two models yield velocity profiles, which are in agreement with the DNS profile in the outer flow region. The OTBLE_VD model shows typical "velocity mismatch" at the first off-wall cell. The mean velocity at the second off-wall LES cell, where the wall model interface is located, fits to the DNS profile. That is the reason for a good wall

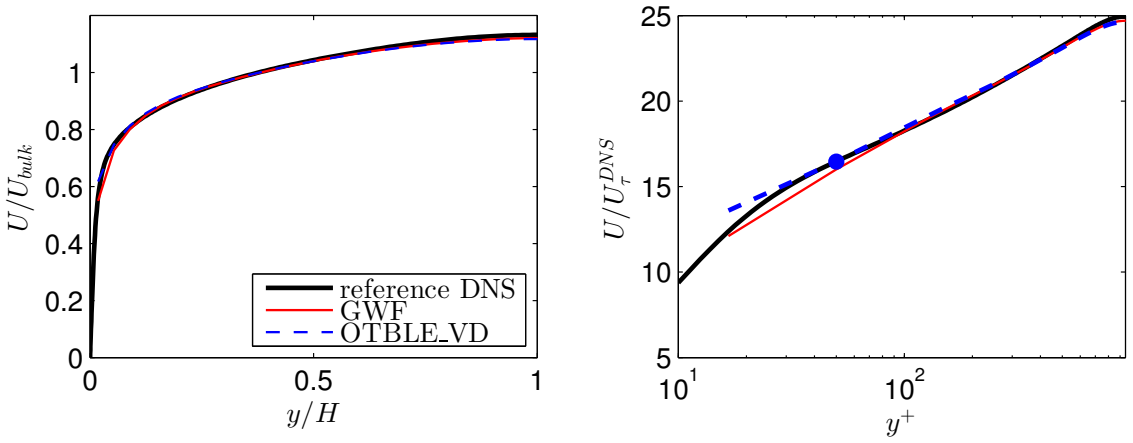

Figure 6.13.: TCF, mean velocity profiles. DNS of Alamo *et al*, LES with resolution $90 \times 56 \times 90$ with GWF and OTBLE_VD wall model. Filled circle indicates the interface between LES and the wall model.

shear stress prediction. The GWF model has the interface at the first off-wall cell, i.e., the OTBLE_VD has to model the double of the height of the GWF, and it still provides the same accuracy as in the wall shear stress as the GWF. The uniform grid $90 \times 56 \times 90$ implies the spacing relation $\Delta_x^+ : \Delta_y^+ : \Delta_z^+ \approx 2 : 1 : 1$. OTBLE_VD simulations on $120 \times 56 \times 120$ (i.e., the same Nx and N_y as in LES-NWR) yield the friction velocity, which is 1% lower than U_τ on the coarser grid. This difference can be safely neglected, thus the idea that the computational grid can be coarsened fulfilling the spacing relation $\Delta_x^+ : \Delta_y^+ : \Delta_z^+ \approx 2 : 1 : 1$ is reasonable. The resolution is also fine enough in the wall-normal direction. Figure 6.11 shows that refinement does not improve the wall shear stress prediction.
There is one more investigation to be done. The reason for an unexpected large error of the OTBLE_Du model should be explained. Figure 6.14 shows the time averaged model velocity profiles for OTBLE_VD and OTBLE_Du. The model velocity profile of OTBLE_VD follow the DNS profile. Whereas, the model velocity profile of OTBLE_Du does not. The Duprat eddy viscosity model is unreliable in this test case. It is unlikely that the model coefficients κ, A, β are the reason for the error. The eddy viscosity model was developed in a turbulent channel flow and it predicts well the eddy viscosity in a posteriori test case in Section 6.1 (see Figure 6.3). The problem might be the incompatibility with the unsteady OTBLE model. The fluctuation of the modeled velocity, of the convective term and of the pressure gradient might corrupt the eddy viscosity model. Especially, unsteadiness of the pressure gradient is crucial since it appears in the formulation of the Duprat eddy viscosity in contrast to the van Driest eddy viscosity. Figure 6.15 shows the model velocity profiles of the OTBLE_Du first with the full pressure gradient $u_{p1} = |\,(\mu/\rho^2)\sqrt{(\partial P/\partial x)^2 + (\partial P/\partial z)^2}\,|^{1/3}$, then only with the streamwise pressure gradient $u_{p2} = |\,(\mu/\rho^2)\,(\partial P/\partial x)\,|^{1/3}$ and finally without any pressure gra-

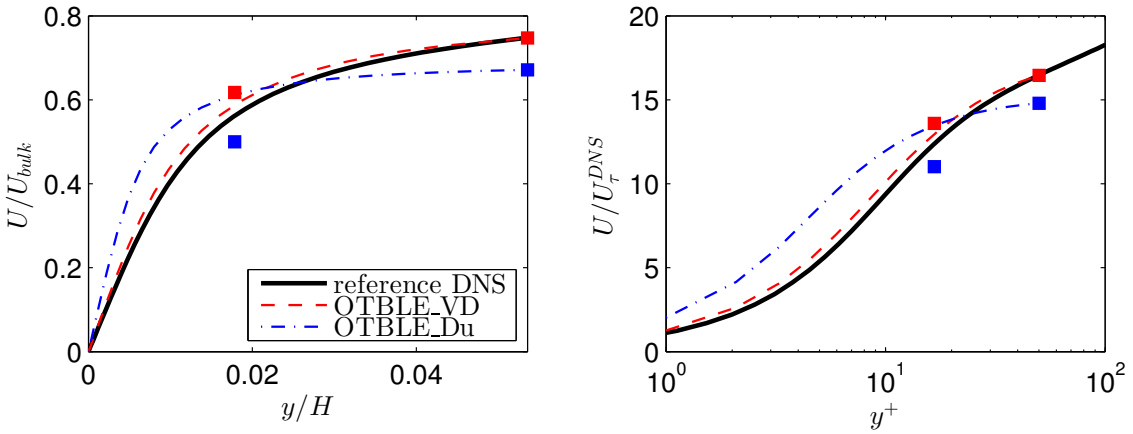

Figure 6.14.: TCF, wall model velocity profiles for turbulent channel flow. DNS of Alamo *et al*, LES with resolution $90 \times 56 \times 90$ with OTBLE_VD and OTBLE_Du wall model. Filled squares indicates LES cells.

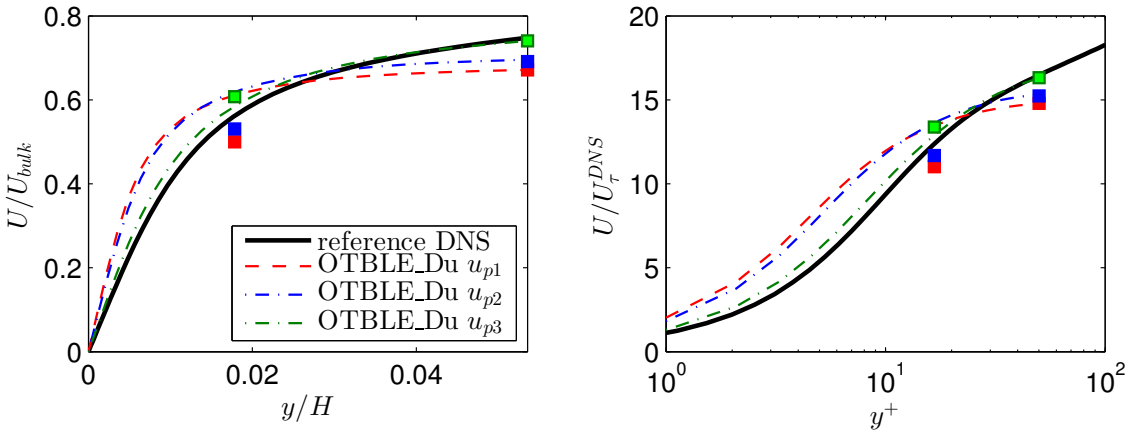

Figure 6.15.: TCF, wall model velocity profiles for turbulent channel flow. DNS of Alamo *et al*, LES with resolution $90 \times 56 \times 90$ with OTBLE_Du and different u_p formulations. Filled squares indicate LES cells.

dient $u_{p3} = 0$. The exclusion of the pressure gradient in the eddy viscosity model improves the agreement with the DNS profile and the friction velocity as a consequence. The friction velocities are $(U_\tau)^{Du}_{u_{p1}} = 1.26U^{VD}_\tau$, $(U_\tau)^{Du}_{u_{p2}} = 1.19U^{VD}_\tau$ and $(U_\tau)^{Du}_{u_{p3}} = 1.02U^{VD}_\tau$. The van Driest eddy viscosity still performs better than the modified versions of the Duprat model. The van Driest model has proven its reliability, it might be not always accurate but it is robust and thus chosen for further simulations as default eddy viscosity model.

6.2.4. Summary

Turbulent channel flow simulations with different wall models have shown that GWF and OTBLE_VD models perform well and reproduce the friction velocity of a fully resolved LES with near-wall resolution.
The Duprat eddy viscosity model with pressure dependency has shown to be incompatible with unsteady OTBLE model in turbulent channel flow simulations.
The spacing relation $\Delta^+_x : \Delta^+_y : \Delta^+_z \approx 2 : 1 : 1$ has proven to be a reasonable instruction for the grid coarsening in TCF.
All OTBLE models with an interface higher than the first off-wall cell show the typical "velocity mismatch" in LES cells below the interface.
The wall model interface should be set above the first LES cell but not too far from the wall because the eddy viscosity model and the convective term model are inaccurate further from the wall.
If the convective term in time averaged flow can be neglected than it can also be neglected in the OTBLE model since it does not affect the time averaged quantities.

6.3. Shock/Turbulent Boundary Layer Interaction

In this section we consider an LES of a shock/turbulent boundary layer interaction (labeled STBLI throughout) consistent with the flow conditions of the IUSTI experiment of Dupont *et al.* [27]. An oblique shock wave generated by an 9° wegde impinges on a $M = 2.3$ flat plate turbulent boundary layer with a displacement thickness Reynolds number of $Re_{\delta 1} = 21000$. A sketch of a STBLI is given in Figure 6.16. For a sufficiently large shock strength, the associated adverse pressure gradient induces a separation of the boundary layer. At the leading edge of the separation bubble, compression waves form the the reflected shock. The flow deviation along the downstream side of the bubble produces the expansion fan, which is followed by reattachment compression waves. Further downstream, the boundary layer recovers to an equilibrium state after a relaxation process. The test case provides regions where equilibrium assumptions are supposed to hold (e.g. upstream the separation bubble) and regions with strong non-equilibrium effects.

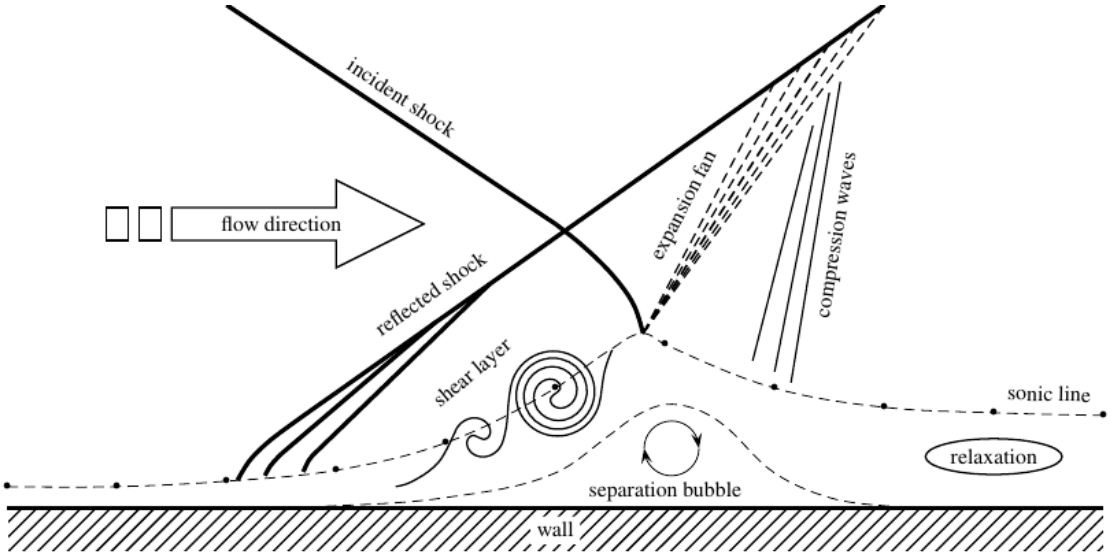

Figure 6.16.: Sketch of the oblique shock/boundary layer interaction taken from Touber and Sandham [2].

6.3.1. Computational Setup

Recently, the fully resolved ILES of STBLI was performed by Budich at TU Munich [28]. This simulation is taken as a reference for the wall model investigation and is referred to as LES-NWR. Its computational setup is given in Table 6.4. The hyperbolic sine stretching with stretching factor 5.5 is applied in the wall-normal direction. The initial conditions are generated using the digital filter technique described in [2]. In this study we use use the computational setup of Budich, but

$\delta_0^{ref} = 12.64\ mm$			
$\delta_0^{in} = 0.826\ \delta_0^{ref}$			
$l^+ = 0.001079\ \delta_0^{ref}$			
Streamwise direction	$L_x = 31.08\ \delta_0^{ref}$	$N_x = 800$	$\Delta_x^+ = 35.91$
Wall-normal direction	$L_y = 6\ \delta_0^{ref}$	$N_y = 180$	$\Delta_{y,min}^+ = 1.39$ $\Delta_{y,max}^+ = 167.35$ $\Delta_{y,avg}^+ = 30.89$
Spanwise direction	$L_z = 1.6\ \delta_0^{ref}$	$N_z = 120$	$\Delta_z^+ = 12.32$

Table 6.4.: STBLI, grid for LES-NWR.

modify grid resolution. The wall model should cover 10% of the smallest boundary

layer height δ_0^{in}, that implies $\Delta^+_{y,min} = 51.03$ if the interface is set to the center of the second off-wall cell. The resolution in the outer region is unchanged, i.e., $\Delta^+_{y,max} = 167.35$. That yields the stretching factor 1.85 for the hyperbolic sine stretching function, $N_y = 66$ and $\Delta^+_{y,avg} = 84.25$. Thus, default grid resolution is chosen to be $N_x \times N_y \times N_z = 672 \times 66 \times 70$ such that the relation $\Delta^+_x : \Delta^+_{y,avg} : \Delta^+_z \approx 2 : 4 : 1$ is fulfilled. This relation requires finer grid than relation for turbulent channel flow, which is $\left(\Delta^+_x : \Delta^+_{y,avg} : \Delta^+_z\right)_{TCF} \approx 2 : 1 : 1$. The refinement in the streamwise direction is motivated by the flow complexity of STBLI. The grid for WMLES is shown in Table 6.5. The simulations are initialized with 2 flow

$\delta_0^{ref} = 12.64\ mm$			
$\delta_0^{in} = 0.826\ \delta_0^{ref}$			
$y_{top} = 0.1\delta_0^{in}$			
$l^+ = 0.001079\ \delta_0^{ref}$			
Streamwise direction	$L_x = 31.08\ \delta_0^{ref}$	$N_x = 672$	$\Delta^+_x = 42.861$
Wall-normal direction	$L_y = 6\ \delta_0^{ref}$	$N_y = 66$	$\Delta^+_{y,min} = 50.27$ $\Delta^+_{y,max} = 161.6$ $\Delta^+_{y,avg} = 84.25$
Spanwise direction	$L_z = 1.6\ \delta_0^{ref}$	$N_z = 70$	$\Delta^+_z = 21.18$

Table 6.5.: STBLI, grid for WMLES.

through times (FTTs) without a wall model following by 4 FTTs with it. Statistics are gathered subsequently during 10 FTTs. One FTT is equal to $31.08\delta_0^{ref}/U_0$. The origin of the Cartesian coordinate system is set to the point, where the shock nominally impinges at the wall. Thus, the computational domain expands from $x = -23.16\delta_0^{ref}$ to $x = 7.96\delta_0^{ref}$ in the streamwise direction. All WMLES are run with the van Driest eddy viscosity model, since the Duprat eddy viscosity has shown poor results in turbulent channel flow (see Section 6.2.3).

6.3.2. Streamwise Temperature Gradient

In the derivation of the wall model energy equation, the wall-tangential temperature convection is neglected. Figure 6.17 shows the streamwise temperature gradient and the streamwise temperature convection at the wall $y = 0$ and at $y = 0.1\delta_{in}^{ref}$ of the LES-NWR. In the boundary layer $x/\delta_0^{ref} < -5$ and in the second part of the separation region $x/\delta_0^{ref} > -2$ and in the reattachment region $x/\delta_0^{ref} > 1$, the streamwise temperature convection can be neglected. Only in the separation region where the

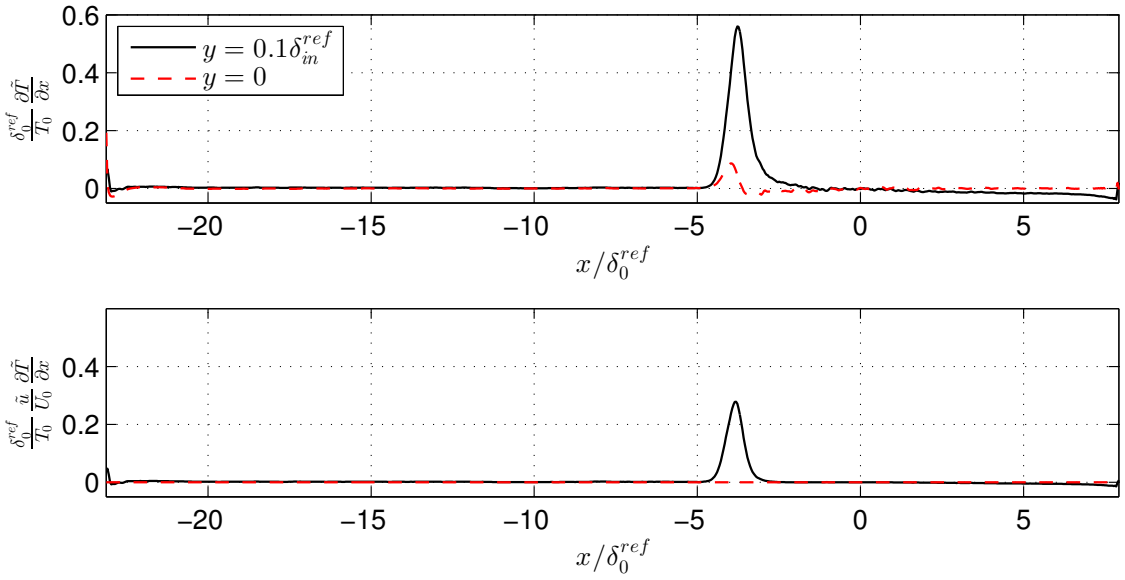

Figure 6.17.: STBLI, LES-NWR. (a) streamwise temperature gradient, (b) streamwise temperature convection.

compression waves heat the gas, $-5 < x/\delta_0^{ref} < -2$, the temperature gradient is important but only further from the wall. The wall is only weakly affected since $T_w \approx T_t$. The velocity is decreased by compression waves thus the dimensionless temperature convection is roughly halved in comparison to the dimensionless temperature gradient. Hence, the LES-NWR shows that the assumption $\tilde{u}\frac{\partial \tilde{T}}{\partial x} \approx 0$ is reasonable everywhere except of regions affected by strong compression waves.

6.3.3. Isothermal Wall Model

The wall model equations can be solved neglecting the energy equation if it is assumed that the modeled region is isothermal $T = const$. This statement together with the the constant pressure across the boundary layer leads to constant density, i.e., the compressible equations are reduced to the incompressible ones. Figure 6.18 shows the temperature at the wall and at the interface y_{top} for simulations with 0TBLE_3 model first with the energy equation then without it. It should pointed out that the wall temperature taken from the wall model is referred to as the wall temperature and not that taken from the first off-wall LES cell. The wall model with the energy equation predicts the wall temperature well, whereas the isothermal wall model underestimates it by roughly 20%. Such a high discrepancy is explained by a high Mach number (see Figure 6.19a). With the nominal inflow Mach number of 2.3, the flow at the interface before the oblique shock is still supersonic with $M \approx 1.3$. A large error in temperature leads to an error in the wall shear stress because of the viscosity dependency on temperature. Using Eq. 2.1.11 with $S_0 = 0.753$, the

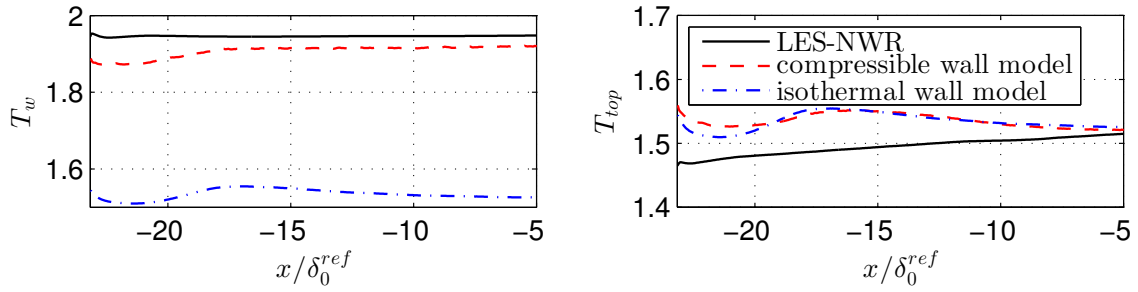

Figure 6.18.: STBLI, reference LES-NWR and LES with compressible and incompressible (isothermal) wall models. (a) wall temperature, (b) temperature at the wall model interface.

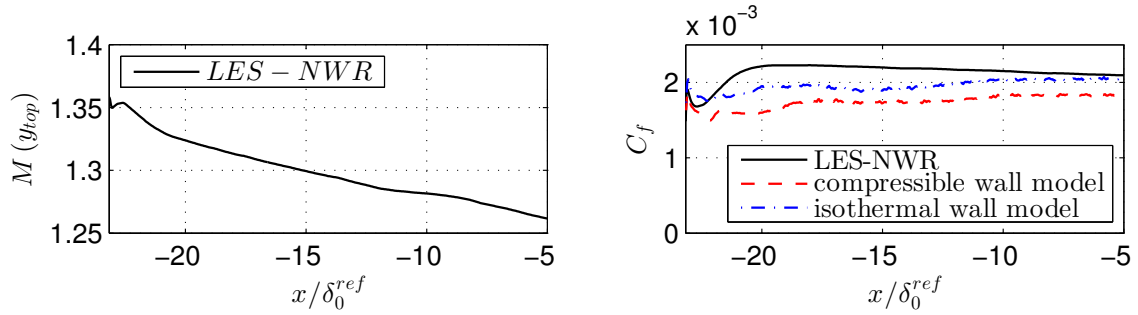

Figure 6.19.: STBLI, reference LES-NWR and LES with compressible and incompressible (isothermal) wall models. (a) local Mach number at the wall model interface height, (b) skin friction coefficient.

viscosity ratio is estimated to be

$$\left(\frac{\mu_{isothermal}}{\mu_{full\ \ model}}\right)_w \approx 0.83. \tag{6.3.1}$$

That means the underprediction of the wall shear stress by the isothermal wall model is 17%, given the same velocity gradient at the wall. Nevertheless, the velocity gradient is not the same for both models. The skin friction coefficient is higher with the isothermal model (see Figure 6.19b). The reason for that is much higher velocity gradient of the compressible model. Given the same mean velocity and density at the interface for both models, the incompressible flow has a higher mass flow rate than the compressible flow because of the density reduction towards the wall in the compressible case. Hence, the wall shear stress is higher for the isothermal model. C_f in both cases is scaled with the same reference value. Thus, C_f supplied by the incompressible model is higher. The isothermal model is not better than the compressible model. Since the compressible model underestimtes C_f, the incompressible model occasionally yields better result. The isothermal wall model is not considered in further investigations and it is not recommended to use in high Mach number computations. Figure 6.18b shows that both models have comparable

temperatures at the interface even if the wall temperatures are different. The reason is that the wall model supplies the LES flow solver only with the wall shear stress. If both models yield similar values for τ_w then the solution fields on the LES grid are similar too.

6.3.4. Wall Model Comparison

In this section we compare OTBLE models with different convection term formulations. Furthermore, we differentiate between models with the energy equation (abbrevated by suffix '-full') and models with analytical formulation for the temperature (abbrevated by suffix '-ana'). Hence, the models to compare are:

1. OTBLE_3_full,
2. OTBLE_2_full,
3. OTBLE_0_full,
4. OTBLE_3_ana,
5. OTBLE_2_ana,
6. OTBLE_0_ana.

At first we investigate the attached boundary layer $x/\delta_0^{ref} < -5$ that is in equilibrium and has negligible streamwise pressure gradient. The simulations with different convective term formulations yield very similar time averaged results. As a consequence, the convective term modeling is by far less important than the modeling of other terms like the eddy viscosity. Results of the WMLES with both energy models and the LES without wall modeling on the same coarse grid are shown in Figure 6.20. There are no significant differences between both models. The pressure is reasonably well predicted by all underresolved simulations. The boundary layer thickness in simulations with the OTBLE models overestimate the reference LES result close to the inlet. Then, for $x/\delta_0^{ref} > -13$ they match. The coarse simulation without wall modeling overestimates δ, it also clearly fails to estimate the wall temperature and the skin friction. Both models yields somewhat different wall temperatures, but they deviate from the reference LES temperature by roughly 1.5%. That is negligible and, hence, it does not affect the velocity profile nor the viscosity at the wall. As a consequence, both models yield the same skin friction coefficient. The predicted C_f is lower than that of the reference LES. The modeling error is due to the eddy viscosity formulation. The reason for the skin friction underestimation might be also in the inflow turbulence generation since the digital filter is sensitive to the spanwise and wall-normal grid resolution. That might be also the reason for the boundary layer thickness mismatch between both models and the reference LES at the inlet.

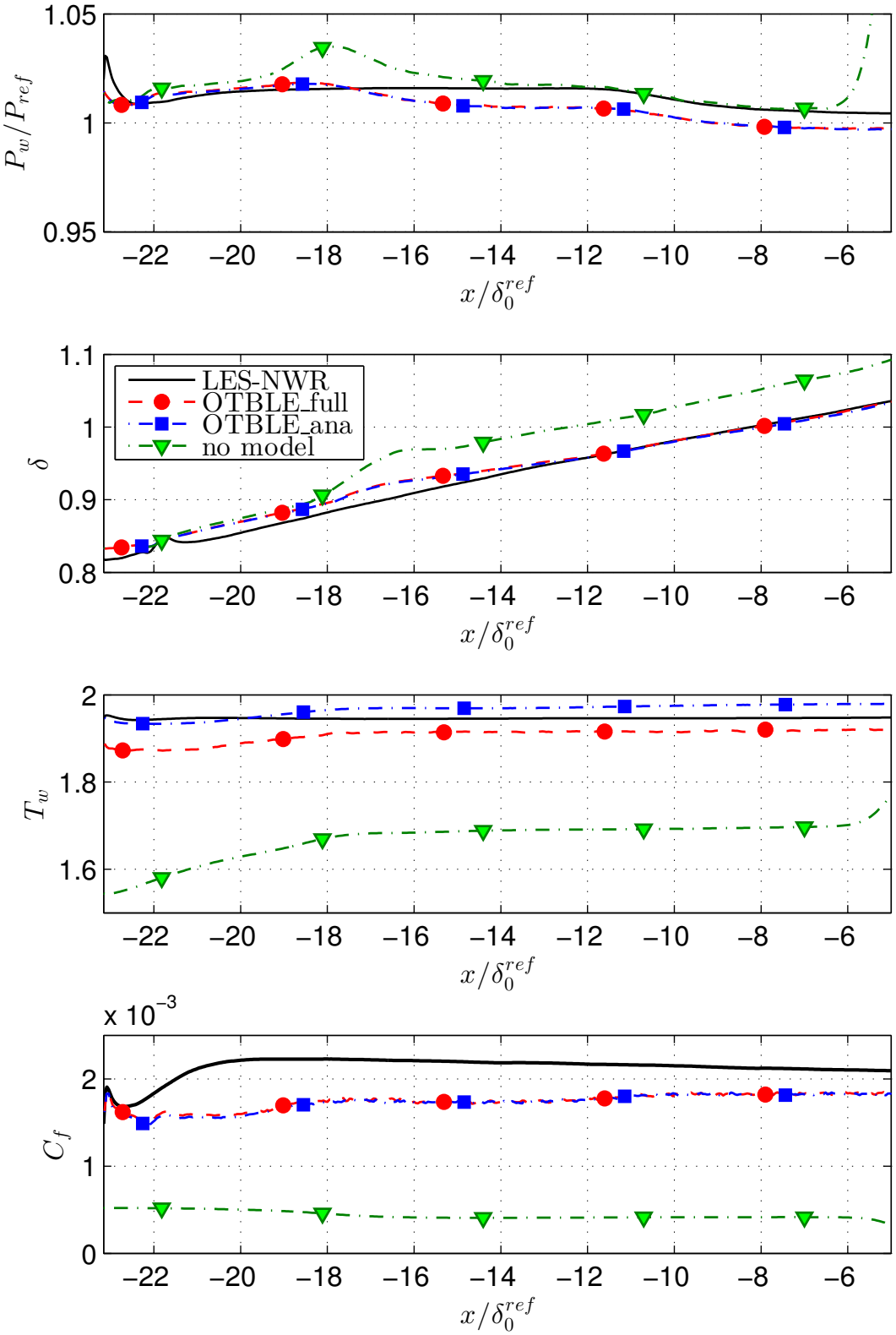

Figure 6.20.: STBLI, attached flow region. (a) pressure at the wall, (b) wall temperature, (c) boundary layer thickness, (d) skin friction coefficient.

The second wall region $x/\delta_0^{ref} > -5$ deals with separation and reattachment and hence, it is highly unsteady. At first we investigate the OTBLE_3_full and OTBLE_3_ana models and the coarse LES without wall modeling. Results are shown in Figure 6.21. The LES on the coarse grid without wall modeling can predict well the pressure at the wall and the temperature at the second off-wall cell. The reason for such a well prediction is that these quantities are to the most part imposed by the outer flow. The coarse LES fails in the wall friction estimation since it can not resolve the near-wall flow field. In simulations with wall models the separation area is much smaller than that in the reference LES. The oblique shock has a stronger intensity since the pressure level in the reattachment region is higher than in the reference LES. Stronger shock intensity enhances compression waves and hence, the skin friction decreases steeper. The temperature level at the interface is estimated with a small error.

Wall models provide two spurious features in the separation region: negative streamwise temperature gradient at the beginning of the compression region, and they yield strong negative skin friction. It can be explained by means of Figure 6.22 that shows the mean velocity profile at two first off-wall LES cells. In both cases WMLES cells have positive streamwise velocity, i.e., there is no separation in the LES domain. The separation exists only in the wall model region (both models provide negative C_f) at $-3 < x/\delta_0^{ref} < 1$. The LES grid can not resolve the separation bubble. The separation region in the reference LES and in the wall model region are shown in Figure 6.23. The shape is determined by $\tilde{u} = 0$. The reference region has the dimensions $L_{sep} = 4.56$ and $H_{sep} = 0.19$, i.e., it is resolved with 117 cells in the streamwise and 67 cells in the wall-normal direction in LES-NWR. On the coarse grid the resolution of that bubble would be 98 and 3 cells, respectively. The resolution in the wall-normal direction is too coarse to reproduce that separation bubble or any thinner one. If the separation exists only in the modeled layer, the supplied negative wall shear stress accelerates the flow in LES near-wall cells, and thus it remains attached. Therefore, the region, where wall model yields negative C_f, is much smaller than the separation region in the reference LES. This effect is referred to as "virtual separation".

Strong negative skin friction coefficient can be explained by means of the ordinary differential equation analysis. The adverse pressure gradient in the wall model is so strong that it should enforce the stream to revert. But the velocity at the upper boundary is kept positive. To fulfill the boundary condition, the region with the reverted flow can not fill the entire wall model height. Thus, the flow in one part closer to the wall is reverted, but in the other part the flow keeps the direction of the velocity at the upper boundary. Hence, the velocity gradient at the wall is stronger negative to account for the adverse pressure gradient. That yields unphysical strong negative skin friction coefficient. Negative streamwise temperature gradient in the compression zone at the wall originates in the virtual separation and in the absence of the temperature convection term in the energy equation.

Both wall models, one with energy equation and the other with an analytical expression for the temperature lead comparable results. The model with the energy

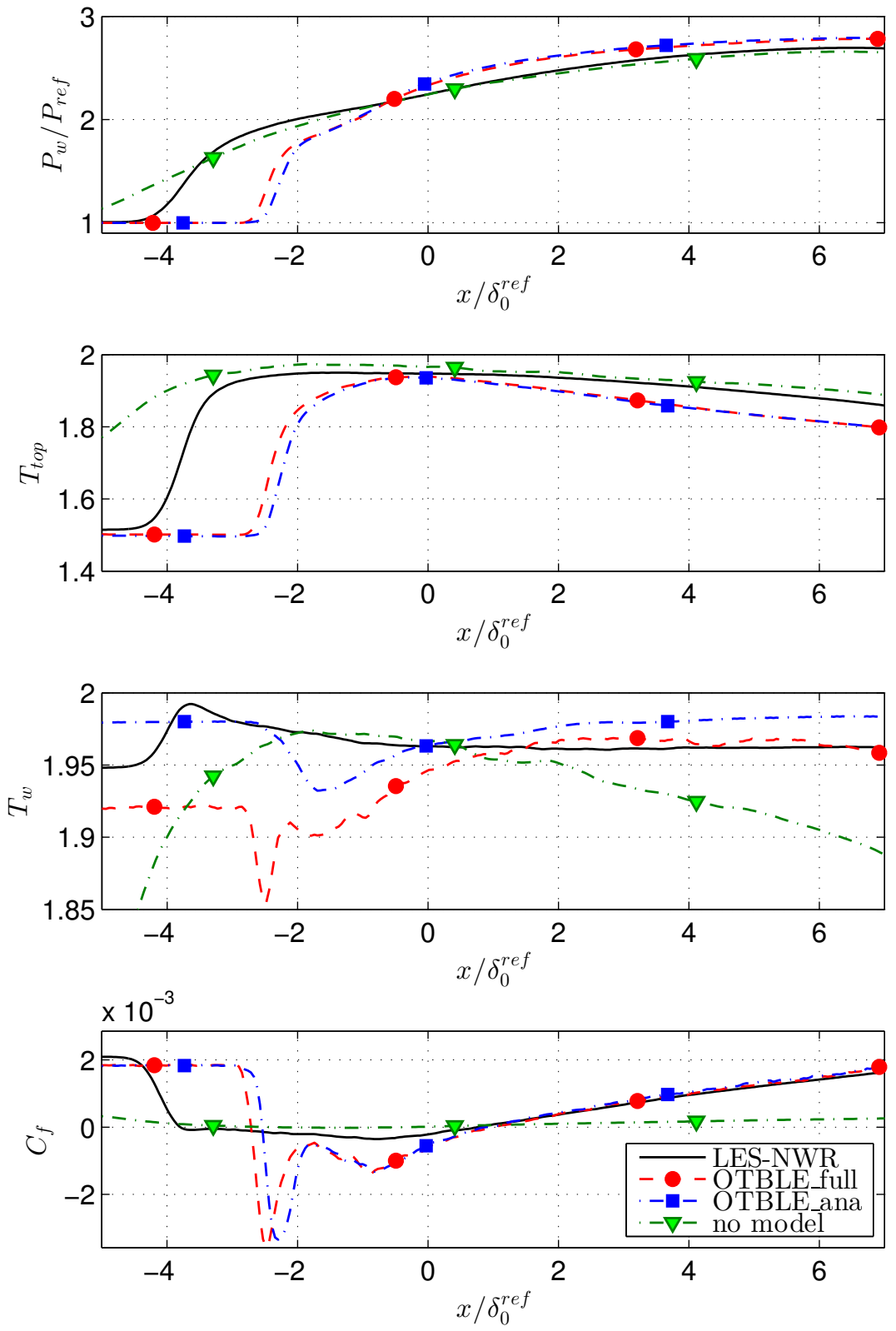

Figure 6.21.: STBLI, separation and reattachment regions. (a) pressure at the wall, (b) temperature at the model interface height, (c) wall temperature, (d) skin friction coefficient.

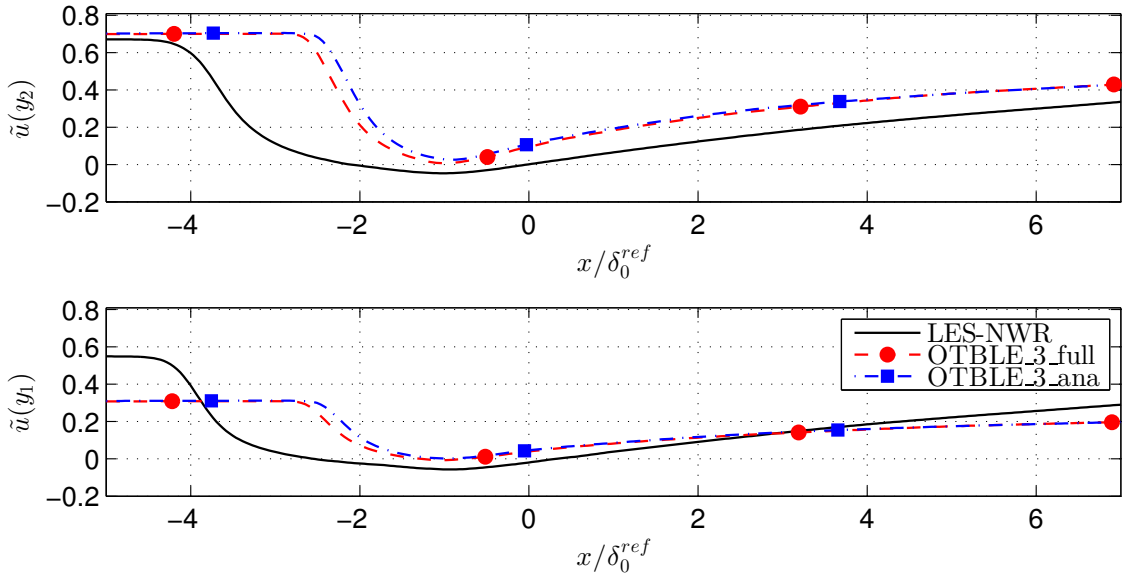

Figure 6.22.: STBLI, separation and reattachment regions. (a) streamwise velocity at the height of the second off-wall WMLES cell, (b) streamwise velocity at the height of the first off-wall WMLES cell.

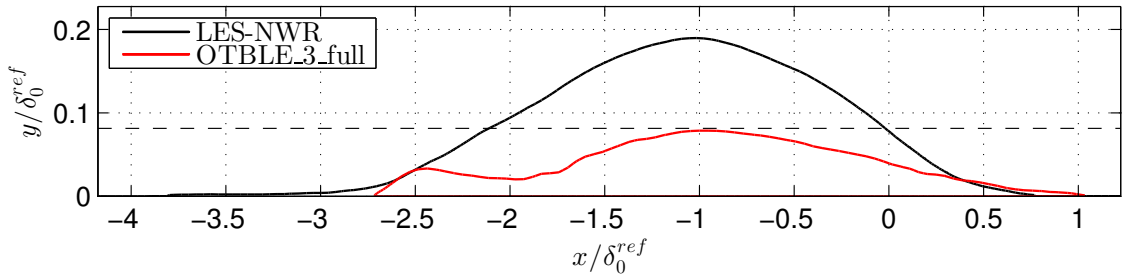

Figure 6.23.: STBLI, separation bubble of LES-NWR and separation bubble in the all model region (virtual separation). Dashed line indicates the wall model interface.

equation might be slightly better since it predicts the beginning of the compression region further upstream (see the pressure at the wall, Figure 6.21). But it requires more computational effort. The less compressible the flow is in the wall model region, the less important is temperature variation. Hence, the analytical expression for the temperature can be used as a cheap alternative to the energy equation.
It can not be concluded, which convective term formulation is better since they all yields the same results in the boundary layer and in reattachment regions. They differ only in the "virtual separation" region. Figure 6.24 shows C_f at $-3 < x/\delta_0^{ref} < 1$ for WMLES with OTBLE_3_full, OTBLE_2_full and OTBLE_0_full. The models with lower order convection and with no convection have weaker C_f oscillations than the higher order convective term model. The boundary layer region shows

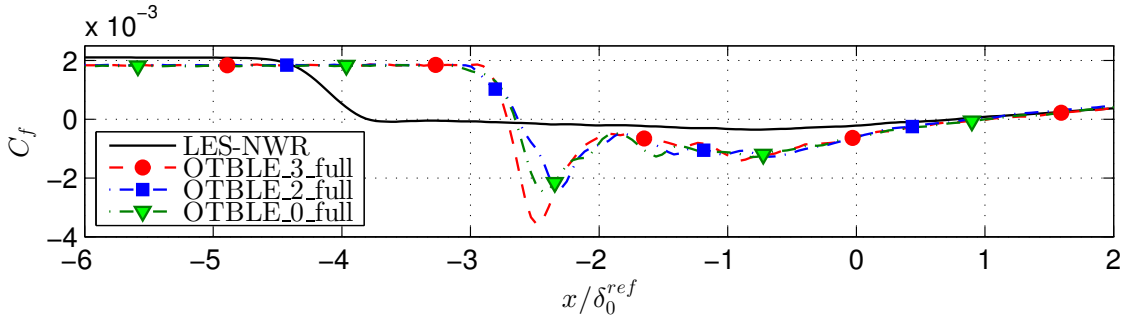

Figure 6.24.: STBLI, separation region. Skin friction coefficient.

that the importance of the convective term modeling is far behind the importance of the eddy viscosity modeling.

6.3.5. Virtual Separation Fix

There are two suggestions to fix the virtual separation. One possible solution might be modification of the velocity at LES cells at the wall. If the wall model indicates the separation, i.e., wall shear stress has an opposite sign to the velocity at the interface then the velocity at the LES cell is modified to trigger the separation. For instance, the velocity can be set to zero. The indication process can take one iteration as well as several iterations. It should be pointed out that modification of the velocity violates the conservative concept of the finite volume method. Hence, it is strongly advised not to change the velocity field directly. Instead of the "velocity fix", the computed wall shear stress can be adjusted to trigger the separation. The wall shear stress can be set to zero as long the wall model indicates the mismatch in sign of $\tilde{u}$ and τ_w. Figure 6.25 shows the velocity profile at the first off-wall LES cells computed with OTBLE_0_full with "wall shear stress fix". 24 LES cells have slightly negative mean streamwise velocity. Separation is not virtual anymore, spurious negative C_f has disappeared and the compression occurs earlier. That can

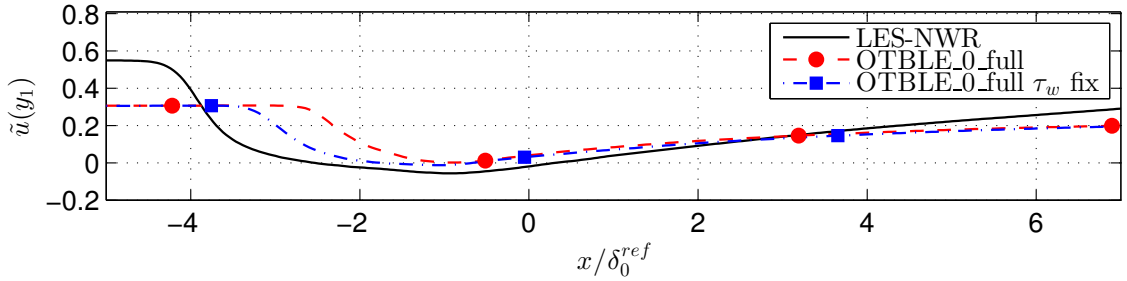

Figure 6.25.: STBLI, separation and reattachment regions. Streamwise velocity at the height of the second off-wall WMLES cell.

be seen in Figure 6.26. The wall shear stress fix improves significantly the wall model. Nevertheless, the separation region is still underresolved. To achieve further improvements, grid refinement should be performed in the separation region.

6.3.6. Summary

In shock/turbulent boundary layer interaction, the eddy viscosity is the most crucial modeled term. Error introduced by convective term modeling is negligible in comparison to that of the eddy viscosity model. Convective term can be safely neglected in shock-free equilibrium regions.
The wall model with analytical expression for the temperature yields results comparable to the wall model with the simplified energy equation. The analytical model is faster and hence preferable. Nevertheless, differences between both models might become more significant in hypersonic flow or at higher Reynolds number.
This test case discovered a new problem of virtual separation that is related to the interaction wall model/separation region. This problem occurs only if the LES resolution is too coarse to resolve a separation bubble that exists only in the wall model. A wall shear stress fix proposed in the above section can significantly improve the wall model.

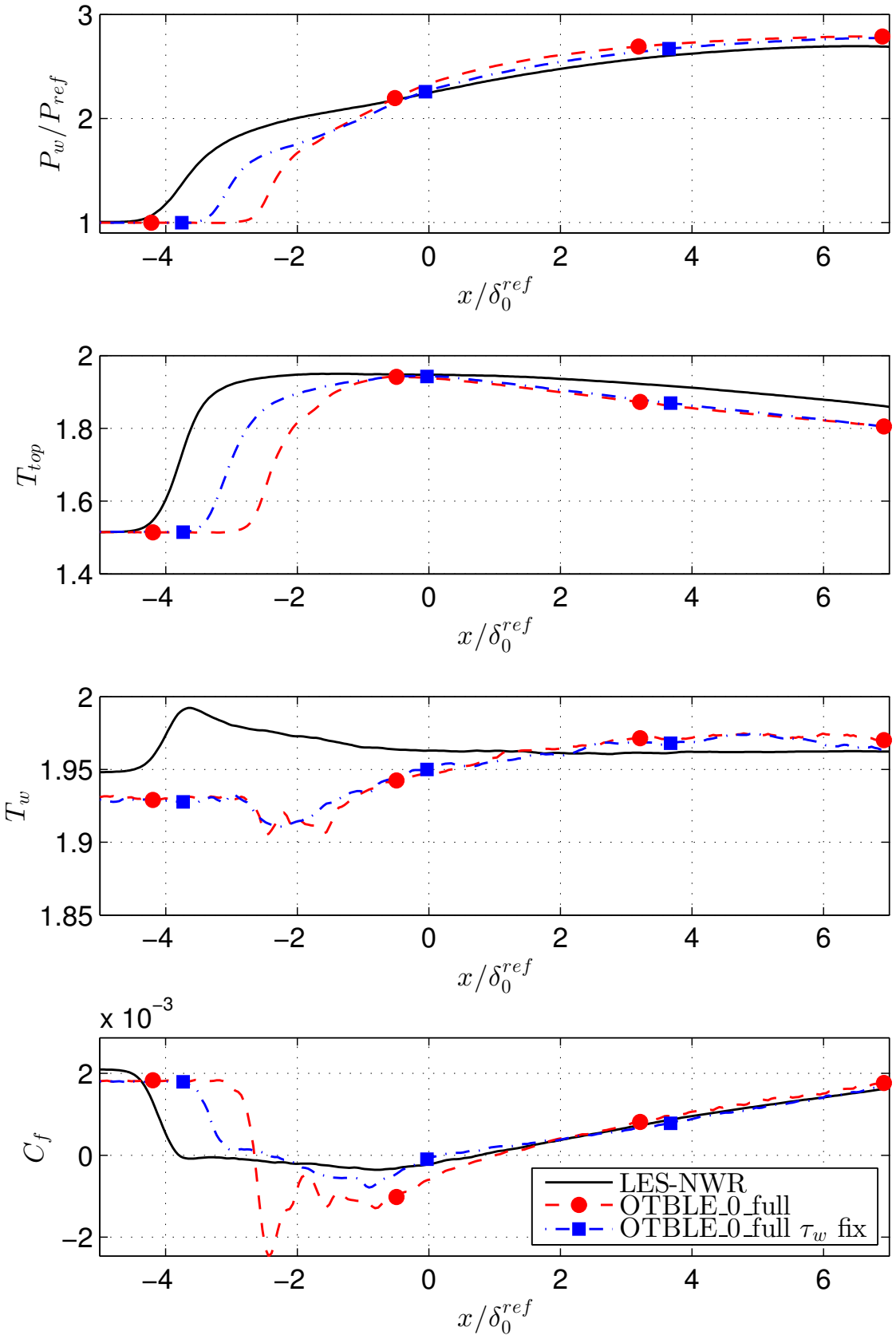

Figure 6.26.: STBLI, separation and reattachment regions. (a) pressure at the wall, (b) temperature at the model interface height, (c) wall temperature, (d) skin friction coefficient.78

7. Conclusion

LES with the proposed wall model perform well if the wall model interface is set to $y_{top} = 0.1\delta_{min}$. It has been shown that the interface should be set at least at the second off-wall LES cell. The solution at the first off-wall LES cell is too inaccurate and can not be used as input for the wall model. The wall model embedded mesh should be fine enough to achieve convergence. The resolution with $\Delta = 0.5l^+$ has proven to be sufficient at the lower boundary (wall). A grid stretching can be applied towards the upper boundary (wall model interface). Simulations results suggest that the convective term can safely be neglected in equilibrium regions. In compressible flow the energy equation can be replaced by the analytical expression for the temperature.
On coarse grid, WMLES yields results comparable to LES with near wall resolution. Nevertheless LES-NWR results can not be exactly reproduced by WMLES. The reasons are discussed in the following section.

7.1. Sources of Error in WMLES

In this section all possible sources of error are summarized. The first error is introduced by the fundamental assumption that the TBLE are valid for description of the boundary layer of an unsteady LES simulation. The neglected terms are small only in the Reynolds averaged sense. The filtered terms preserve instantaneous fluctuations, hence it is not straightforward to estimate the instantaneous significance of different terms. Nevertheless, simulations have shown that in regions, where the flow is in equilibrium, the TBLE can be applied for WMLES. In highly unsteady region like separation region, the TBLE do not hold. Thus the wall model can not predict the exact position of separation point no matter how accurate the modeled terms are.
There are also sources of error within the TBL approximation. For the correct wall shear stress prediction, the eddy viscosity model is of paramount importance. The convective term error is negligible in comparison to the error introduced by available eddy viscosity models. Thus, development of reliable eddy viscosity models is assessed to be a primary topic in wall modeling research.
Next source of error comes from underresolution of WMLES. Even if the wall model is perfect, it requires input from LES cells. Thus, these cells should be fine enough to resolve the flow field at the height of the wall model interface. It is not straight-

forward to determine the optimal cell size. if the LES cell supplies inaccurate input to the wall model then the wall model can not predict correct wall shear stress. The LES grid resolution is also extremely important if there are small structures like small separation bubbles. If the size of the separation bubble is of order of the LES grid spacing then it can not be captured by LES. Hence, the separation exists only in the wall model region. That leads to inaccurate prediction of the separation point and to spurious wall shear stress oscillations. This effect is referred to as virtual separation. The problem can be partially solved by an *ad hoc* wall shear stress fix.
The last source of error is due to the current implementation of the wall model. LES flow solver and the wall model are not coupled iteratively, i.e., the wall model computes wall shear stress using LES field quantities from the previous time step. Nevertheless, this error might become significant only in highly unsteady simulations.
Proposes possible improvements to reduce the wall model error are proposed in the next section.

7.2. Further Improvements and Investigations

There are several suggestions to improve the wall model.
To speed up the computation, number of cells in the wall model can be adjusted dynamically according to the locally computed wall shear stress. Then, solution at the previous time step should be interpolated on the new mesh if the mesh resolution has been changed. One could use compact finite difference schemes, that increases the scheme order without changing the stencil. Thus, the Thomas algorithm can still be applied.
To improve the eddy viscosity model one can try to use two equations models.
The compressible wall model can be improved in compression regions by taking into account the streamwise temperature convection, where the temperature gradient can be modeled as a polynomial.
There are some further investigations, which can be done to access which model is better, that with energy equation or that with analytical expression for the temperature. The compressible wall model should be validated by a simulation with wall heat transfer and by hypersonic flow simulation.

A. Appendix

A.1. Transformation Between Conservative and Primitive Form

The density weighted material derivative of a random quantity ϕ is defined by

$$\rho\frac{D\phi}{Dt} = \rho\frac{\partial\phi}{\partial t} + \rho u_i\frac{\partial\phi}{\partial x_i}. \tag{A.1.1}$$

The material derivative is written in primitive form. The same derivative written in conservative form is defined by

$$\frac{\partial\rho\phi}{\partial t} + \frac{\partial(\rho u_i\phi)}{\partial x_i}. \tag{A.1.2}$$

The transformation is possible by means of the continuity equation (2.1.1). We rewrite the conservative form as

$$\rho\frac{\partial\phi}{\partial t} + \phi\frac{\partial\rho}{\partial t} + \frac{\partial(\rho u_i\phi)}{\partial x_i}. \tag{A.1.3}$$

Then, we replace $\frac{\partial\rho}{\partial t}$ by $-\frac{\partial(\rho u_i)}{\partial x_i}$. and finally, we get

$$\rho\frac{\partial\phi}{\partial t} + \rho u_i\frac{\partial\phi}{\partial x_i} = \frac{\partial\rho\phi}{\partial t} + \frac{\partial(\rho u_i\phi)}{\partial x_i}. \tag{A.1.4}$$

A.2. Van Driest Transformation

The van Driest transformation can be regarded as transforming the inner-layer part of the compressible boundary layer streamwise velocity profile $\tilde{u}(y^+)$ to an equivalent incompressible flow profile $U(y^+)$ that obeys the law of the wall. The transformation formula is given by

$$U^+_{VD}(y^+) = \int_0^{\tilde{u}^+}\sqrt{\frac{\rho}{\rho_w}}du^+. \tag{A.2.1}$$

The transformation takes into account the density variation across the compressible boundary layer. It is valid only for adiabatic walls. For extensions of the van Driest transformation, that, e.g., account for the wall heat transfer, it is referred to [29].

A.3. Polynomial Coefficients for the Incompressible OTBLE_3 Wall Model

The polynomial coefficients a_j^i and b_j^i for the incompressible OTBLE_3 wall model are

$$a1^U = -\frac{-{y_{top}}^2\left(\frac{\partial^2 U}{\partial x \partial y}\right)_{top} - 2\,{y_{top}}^2\left(\frac{\partial^2 W}{\partial z \partial y}\right)_{top} + 6\,y_{top}\left(\frac{\partial U}{\partial x}\right)_{top} + 8\,y_{top}\left(\frac{\partial W}{\partial z}\right)_{top} + 12\,V_{top}}{{y_{top}}^2}, \tag{A.3.1}$$

$$a2^U = \frac{-3\,{y_{top}}^2\left(\frac{\partial^2 U}{\partial x \partial y}\right)_{top} - 4\,{y_{top}}^2\left(\frac{\partial^2 W}{\partial z \partial y}\right)_{top} + 15\,y_{top}\left(\frac{\partial U}{\partial x}\right)_{top} + 16\,y_{top}\left(\frac{\partial W}{\partial z}\right)_{top} + 24\,V_{top}}{{y_{top}}^3}, \tag{A.3.2}$$

$$a3^U = -2\,\frac{-{y_{top}}^2\left(\frac{\partial^2 U}{\partial x \partial y}\right)_{top} - {y_{top}}^2\left(\frac{\partial^2 W}{\partial z \partial y}\right)_{top} + 4\,y_{top}\left(\frac{\partial U}{\partial x}\right)_{top} + 4\,y_{top}\left(\frac{\partial W}{\partial z}\right)_{top} + 6\,V_{top}}{{y_{top}}^4}, \tag{A.3.3}$$

$$b1^U = \frac{-y_{top}\left(\frac{\partial^2 W}{\partial z \partial y}\right)_{top} + 2\left(\frac{\partial W}{\partial z}\right)_{top}}{y_{top}}, \tag{A.3.4}$$

$$b2^U = -\frac{-y_{top}\left(\frac{\partial^2 W}{\partial z \partial y}\right)_{top} + \left(\frac{\partial W}{\partial z}\right)_{top}}{{y_{top}}^2}, \tag{A.3.5}$$

$$a1^W = \frac{-y_{top}\left(\frac{\partial^2 U}{\partial x \partial y}\right)_{top} + 2\left(\frac{\partial U}{\partial x}\right)_{top}}{y_{top}}, \tag{A.3.6}$$

$$a2^W = -\frac{-y_{top}\left(\frac{\partial^2 U}{\partial x \partial y}\right)_{top} + \left(\frac{\partial U}{\partial x}\right)_{top}}{{y_{top}}^2}, \tag{A.3.7}$$

$$b1^W = -\frac{-2\,{y_{top}}^2\left(\frac{\partial^2 U}{\partial x \partial y}\right)_{top} - {y_{top}}^2\left(\frac{\partial^2 W}{\partial z \partial y}\right)_{top} + 8\,y_{top}\left(\frac{\partial U}{\partial x}\right)_{top} + 6\,y_{top}\left(\frac{\partial W}{\partial z}\right)_{top} + 12\,V_{top}}{{y_{top}}^2}, \tag{A.3.8}$$

$$b2^W = \frac{-4\,{y_{top}}^2\left(\frac{\partial^2 U}{\partial x \partial y}\right)_{top} - 3\,{y_{top}}^2\left(\frac{\partial^2 W}{\partial z \partial y}\right)_{top} + 16\,y_{top}\left(\frac{\partial U}{\partial x}\right)_{top} + 15\,y_{top}\left(\frac{\partial W}{\partial z}\right)_{top} + 24\,V_{top}}{{y_{top}}^3}, \tag{A.3.9}$$

$$b3^W = -2\,\frac{-{y_{top}}^2\left(\frac{\partial^2 U}{\partial x \partial y}\right)_{top} - {y_{top}}^2\left(\frac{\partial^2 W}{\partial z \partial y}\right)_{top} + 4\,y_{top}\left(\frac{\partial U}{\partial x}\right)_{top} + 4\,y_{top}\left(\frac{\partial W}{\partial z}\right)_{top} + 6\,V_{top}}{{y_{top}}^4}. \tag{A.3.10}$$

A.4. Polynomial Coefficients for the Incompressible OTBLE_2 Wall Model

The polynomial coefficients a_j^i and b_j^i for the incompressible OTBLE_2 wall model are

$$a1^U = -\frac{2\,y_{top}\left(\frac{\partial U}{\partial x}\right)_{top} + 3\,y_{top}\left(\frac{\partial W}{\partial z}\right)_{top} + 6\,V_{top}}{{y_{top}}^2}, \tag{A.4.1}$$

$$a2^U = 3\,\frac{y_{top}\left(\frac{\partial U}{\partial x}\right)_{top} + y_{top}\left(\frac{\partial W}{\partial z}\right)_{top} + 2\,V_{top}}{{y_{top}}^3}, \tag{A.4.2}$$

$$b1^U = \frac{\left(\frac{\partial W}{\partial z}\right)_{top}}{y_{top}}, \tag{A.4.3}$$

$$a1^W = \frac{\left(\frac{\partial U}{\partial x}\right)_{top}}{y_{top}}, \tag{A.4.4}$$

$$b1^W = -\frac{2\,y_{top}\left(\frac{\partial W}{\partial z}\right)_{top} + 3\,y_{top}\left(\frac{\partial U}{\partial x}\right)_{top} + 6\,V_{top}}{{y_{top}}^2}, \tag{A.4.5}$$

$$b2^W = 3\,\frac{y_{top}\left(\frac{\partial W}{\partial z}\right)_{top} + y_{top}\left(\frac{\partial U}{\partial x}\right)_{top} + 2\,V_{top}}{{y_{top}}^3}. \tag{A.4.6}$$

A.5. Polynomial Coefficients for the Compressible OTBLE_3 Wall Model

The polynomial coefficients a_j^i and b_j^i for the compressible OTBLE_3 wall model are

$$a_1^U = \frac{-1}{y_{top}\,({y_{top}}^2 I_1 - 2\,I_2\,y_{top} + I_3)}\left(-{y_{top}}^3 I_1\left(\frac{\partial^2\tilde{w}}{\partial z\partial y}\right)_{top} + 2\,I_1\,{y_{top}}^2\left(\frac{\partial\tilde{w}}{\partial z}\right)_{top}\right.$$
$$- I_2\,{y_{top}}^2\left(\frac{\partial^2\tilde{u}}{\partial x\partial y}\right)_{top} + I_2\,{y_{top}}^2\left(\frac{\partial^2\tilde{w}}{\partial z\partial y}\right)_{top} + {y_{top}}^3 I_S + {y_{top}}^3(\overline{\rho}\tilde{v})_{top}$$
$$\left.+3\,y_{top}\,I_2\left(\frac{\partial\tilde{u}}{\partial x}\right)_{top} - y_{top}\,I_2\left(\frac{\partial\tilde{w}}{\partial z}\right)_{top} + y_{top}\left(\frac{\partial^2\tilde{u}}{\partial x\partial y}\right)_{top} I_3 - 2\left(\frac{\partial\tilde{u}}{\partial x}\right)_{top} I_3\right), \tag{A.5.1}$$

$$a_2^U = \frac{1}{y_{top}^2\,({y_{top}}^2 I_1 - 2\,I_2\,y_{top} + I_3)}\left(-{y_{top}}^3 I_1\left(\frac{\partial^2\tilde{u}}{\partial x\partial y}\right)_{top} - 2\,{y_{top}}^3 I_1\left(\frac{\partial^2\tilde{w}}{\partial z\partial y}\right)_{top}\right.$$
$$+ 3\,I_1\,{y_{top}}^2\left(\frac{\partial\tilde{u}}{\partial x}\right)_{top} + 4\,I_1\,{y_{top}}^2\left(\frac{\partial\tilde{w}}{\partial z}\right)_{top} + 2\,I_2\,{y_{top}}^2\left(\frac{\partial^2\tilde{w}}{\partial z\partial y}\right)_{top} + 2\,{y_{top}}^3 I_S$$
$$\left.+2\,{y_{top}}^3(\overline{\rho}\tilde{v})_{top} - 2\,y_{top}\,I_2\left(\frac{\partial\tilde{w}}{\partial z}\right)_{top} + y_{top}\left(\frac{\partial^2\tilde{u}}{\partial x\partial y}\right)_{top} I_3 - \left(\frac{\partial\tilde{u}}{\partial x}\right)_{top} I_3\right), \tag{A.5.2}$$

$$a_3^U = \frac{-1}{y_{top}^2\,({y_{top}}^2 I_1 - 2\,I_2\,y_{top} + I_3)}\left(-{y_{top}}^2 I_1\left(\frac{\partial^2\tilde{u}}{\partial x\partial y}\right)_{top} - {y_{top}}^2 I_1\left(\frac{\partial^2\tilde{w}}{\partial z\partial y}\right)_{top}\right.$$
$$+ 2\,I_1\,y_{top}\left(\frac{\partial\tilde{u}}{\partial x}\right)_{top} + 2\,I_1\,y_{top}\left(\frac{\partial\tilde{w}}{\partial z}\right)_{top} + I_2\,y_{top}\left(\frac{\partial^2\tilde{u}}{\partial x\partial y}\right)_{top} + I_2\,y_{top}\left(\frac{\partial^2\tilde{w}}{\partial z\partial y}\right)_{top}$$
$$\left.+{y_{top}}^2 I_S + {y_{top}}^2(\overline{\rho}\tilde{v})_{top} - I_2\left(\frac{\partial\tilde{u}}{\partial x}\right)_{top} - I_2\left(\frac{\partial\tilde{w}}{\partial z}\right)_{top}\right), \tag{A.5.3}$$

$$b_1^U = \frac{-y_{top}\left(\frac{\partial^2\tilde{w}}{\partial z\partial y}\right)_{top} + 2\left(\frac{\partial\tilde{w}}{\partial z}\right)_{top}}{y_{top}}, \tag{A.5.4}$$

$$b_2^U = \frac{y_{top}\left(\frac{\partial^2\tilde{w}}{\partial z\partial y}\right)_{top} - \left(\frac{\partial\tilde{w}}{\partial z}\right)_{top}}{{y_{top}}^2}, \tag{A.5.5}$$

$$a_1^W = \frac{-y_{top}\left(\frac{\partial^2\tilde{u}}{\partial x\partial y}\right)_{top} + 2\left(\frac{\partial\tilde{u}}{\partial x}\right)_{top}}{y_{top}}, \tag{A.5.6}$$

$$a_2^W = \frac{y_{top}\left(\frac{\partial^2\tilde{u}}{\partial x\partial y}\right)_{top} - \left(\frac{\partial\tilde{u}}{\partial x}\right)_{top}}{{y_{top}}^2}, \tag{A.5.7}$$

$$b_1^W = \frac{-1}{y_{top}\,({y_{top}}^2 I_1 - 2\,I_2\,y_{top} + I_3)} \left(-{y_{top}}^3 I_1 \left(\frac{\partial^2 \tilde{u}}{\partial x \partial y}\right)_{top} + 2\,I_1\,{y_{top}}^2 \left(\frac{\partial \tilde{u}}{\partial x}\right)_{top} \right.$$
$$+ I_2\,{y_{top}}^2 \left(\frac{\partial^2 \tilde{u}}{\partial x \partial y}\right)_{top} - I_2\,{y_{top}}^2 \left(\frac{\partial^2 \tilde{w}}{\partial z \partial y}\right)_{top} + {y_{top}}^3 I_S + {y_{top}}^3 (\overline{\rho}\tilde{v})_{top}$$
$$\left. -y_{top}\,I_2 \left(\frac{\partial \tilde{u}}{\partial x}\right)_{top} + 3\,y_{top}\,I_2 \left(\frac{\partial \tilde{w}}{\partial z}\right)_{top} + y_{top} \left(\frac{\partial^2 \tilde{w}}{\partial z \partial y}\right)_{top} I_3 - 2 \left(\frac{\partial \tilde{w}}{\partial z}\right)_{top} I_3 \right), \tag{A.5.8}$$

$$b_2^W = \frac{1}{y_{top}^2\,({y_{top}}^2 I_1 - 2\,I_2\,y_{top} + I_3)} \left(-2\,{y_{top}}^3 I_1 \left(\frac{\partial^2 \tilde{u}}{\partial x \partial y}\right)_{top} - {y_{top}}^3 I_1 \left(\frac{\partial^2 \tilde{w}}{\partial z \partial y}\right)_{top} \right.$$
$$+ 4\,I_1\,{y_{top}}^2 \left(\frac{\partial \tilde{u}}{\partial x}\right)_{top} + 3\,I_1\,{y_{top}}^2 \left(\frac{\partial \tilde{w}}{\partial z}\right)_{top} + 2\,I_2\,{y_{top}}^2 \left(\frac{\partial^2 \tilde{u}}{\partial x \partial y}\right)_{top} + 2\,{y_{top}}^3 I_S$$
$$\left. +2\,{y_{top}}^3 (\overline{\rho}\tilde{v})_{top} - 2\,y_{top}\,I_2 \left(\frac{\partial \tilde{u}}{\partial x}\right)_{top} + y_{top} \left(\frac{\partial^2 \tilde{w}}{\partial z \partial y}\right)_{top} I_3 - \left(\frac{\partial \tilde{w}}{\partial z}\right)_{top} I_3 \right), \tag{A.5.9}$$

$$b_3^W = \frac{-1}{y_{top}^2\,({y_{top}}^2 I_1 - 2\,I_2\,y_{top} + I_3)} \left(-{y_{top}}^2 I_1 \left(\frac{\partial^2 \tilde{u}}{\partial x \partial y}\right)_{top} - {y_{top}}^2 I_1 \left(\frac{\partial^2 \tilde{w}}{\partial z \partial y}\right)_{top} \right.$$
$$+ 2\,I_1\,y_{top} \left(\frac{\partial \tilde{u}}{\partial x}\right)_{top} + 2\,I_1\,y_{top} \left(\frac{\partial \tilde{w}}{\partial z}\right)_{top} + I_2\,y_{top} \left(\frac{\partial^2 \tilde{u}}{\partial x \partial y}\right)_{top}$$
$$\left. +I_2\,y_{top} \left(\frac{\partial^2 \tilde{w}}{\partial z \partial y}\right)_{top} + {y_{top}}^2 I_S + {y_{top}}^2 (\overline{\rho}\tilde{v})_{top} - I_2 \left(\frac{\partial \tilde{u}}{\partial x}\right)_{top} - I_2 \left(\frac{\partial \tilde{w}}{\partial z}\right)_{top} \right), \tag{A.5.10}$$

where

$$I_1 = \int_0^{y_{top}} \overline{\rho} y d\tilde{y}, \tag{A.5.11}$$

$$I_2 = \int_0^{y_{top}} \overline{\rho} y^2 d\tilde{y}, \tag{A.5.12}$$

$$I_3 = \int_0^{y_{top}} \overline{\rho} y^3 d\tilde{y}, \tag{A.5.13}$$

$$I_S = \int_0^{y_{top}} \frac{\partial \overline{\rho}}{\partial t} + \frac{\tilde{u}}{R\tilde{T}} \left(\frac{\partial P}{\partial x}\right)_{top} + \frac{\tilde{w}}{R\tilde{T}} \left(\frac{\partial P}{\partial z}\right)_{top} d\tilde{y}. \tag{A.5.14}$$

It can be shown that the denominator of the polynomial coefficients $({y_{top}}^2 I_1 - 2\,I_2\,y_{top} + I_3) \neq 0$ if the wall model has at least three grid points.

A.6. Polynomial Coefficients for the Compressible OTBLE_2 Wall Model

The polynomial coefficients a_j^i and b_j^i for the compressible OTBLE_2 wall model are

$$a_1^U = -\frac{I_1\, y_{top} \left(\frac{\partial \tilde{w}}{\partial z}\right)_{top} + {y_{top}}^2 I_S + {y_{top}}^2 (\overline{\rho}\tilde{v})_{top} + I_2 \left(\frac{\partial \tilde{u}}{\partial x}\right)_{top}}{y_{top}\,(I_1\, y_{top} - I_2)}, \tag{A.6.1}$$

$$a_2^U = \frac{I_1 \left(\frac{\partial \tilde{u}}{\partial x}\right)_{top} + I_1 \left(\frac{\partial \tilde{w}}{\partial z}\right)_{top} + I_S\, y_{top} + (\overline{\rho}\tilde{v})_{top}\, y_{top}}{y_{top}\,(I_1\, y_{top} - I_2)}, \tag{A.6.2}$$

$$b_1^U \frac{\left(\frac{\partial \tilde{w}}{\partial z}\right)_{top}}{y_{top}}, \tag{A.6.3}$$

$$a_1^W \frac{\left(\frac{\partial \tilde{u}}{\partial x}\right)_{top}}{y_{top}}, \tag{A.6.4}$$

$$b_1^U = -\frac{I_1\, y_{top} \left(\frac{\partial \tilde{u}}{\partial x}\right)_{top} + {y_{top}}^2 I_S + {y_{top}}^2 (\overline{\rho}\tilde{v})_{top} + I_2 \left(\frac{\partial \tilde{w}}{\partial z}\right)_{top}}{y_{top}\,(I_1\, y_{top} - I_2)}, \tag{A.6.5}$$

$$b_2^U = \frac{I_1 \left(\frac{\partial \tilde{w}}{\partial z}\right)_{top} + I_1 \left(\frac{\partial \tilde{u}}{\partial x}\right)_{top} + I_S\, y_{top} + (\overline{\rho}\tilde{v})_{top}\, y_{top}}{y_{top}\,(I_1\, y_{top} - I_2)}. \tag{A.6.6}$$

It can be shown that the denominator of the polynomial coefficients $(I_1\, y_{top} - I_2) \neq 0$ if the wall model has at least three grid points.

A.7. Finite Difference Formulas for Nonuniform Mesh

Finite difference formulas for nonuniform mesh are taken from [30]. The second order central difference scheme for the first derivative on nonuniform mesh is given by

$$\frac{dU_i}{dx} = \frac{-\alpha_i^2 U_{i-1} + U_i\,(\alpha_i^2 - 1) + U_{i+1}}{h_i\,(\alpha_i + 1)\,\alpha_i}, \tag{A.7.1}$$

where $h_i = x_i - x_{i-1}$ is a grid spacing and $\alpha_i = \frac{h_{i+1}}{h_i}$ is a growth rate. The second order central difference scheme for the first derivative on nonuniform mesh is given by

$$\frac{d^2U_i}{dx^2} = \frac{U_{i+1} - U_i\,(1+\alpha) + \alpha U_{i-1}}{\alpha_i\,(\alpha_i + 1)\,h_i^2}. \tag{A.7.2}$$

Bibliography

[1] S. B. Pope. *Turbulent Flows*. Cambridge, 2000.

[2] E. Touber and N. D. Sandham. Large-eddy simulation of low-frequency unsteadiness in a turbulent shock-induced separation bubble. *Theoretical and Computational Fluid Dynamics*, 23:79–107, 2009.

[3] N. V. Nikitin, F. Nicoud, B. Wasistho, K. D. Squires, and P. R. Spalart. An approach to wall modeling in large-eddy simulations. *Physics of Fluids*, 12:1629–1632, 2000.

[4] J. S. Baggett. On the feasibility of merging les with rans in the near-wall region of attached turbulent flows. *Center for Turbulence Research, Annual Research Briefs 1998*, 1998.

[5] U. Piomelli, E. Balaras, H. Pasinato, K. D.Squires, and P. R. Spalart. The inner-outer layer interface in large-eddy simulations with wall-layer models. *International Journal of Heat and Fluid Flow*, 24, 2003.

[6] F. Hamba. A hybrid RANS/LES simulation of turbulent channel flow. *Theoretical and Computational Fluid Dynamics*, 16, 2003.

[7] F. Hamba. A hybrid RANS/LES simulation of high-Reynolds-number channel flow using additional filtering at the interface. *Theoretical and Computational Fluid Dynamics*, 20, 2006.

[8] L. Temmerman, M. Hadziabdic, M. A. Leschziner, and K. Hanjalic. A hybrid two-layer URANS-LES approach for large eddy simulation at high reynolds numbers. *International Journal of Heat and Fluid Flow*, 26:173–190, 2005.

[9] J. D. Anderson. *Modern Compressible Flow with Historical Perspective, 2nd edition*. McGraw Hill, 1990.

[10] D. C. Wilcox. *Turbulence Modeling for CFD, 2nd edition*. DCW Industries, 1994.

[11] A. Leonard. Energy cascade in large eddy simulation of turbulent fluid flow. *Advances in Geophysics*, 18A:237–248, 1974.

[12] E. Garnier, N. Adams, and P. Sagaut. *Large Eddy Simulation for Compressible*

Flows. Springer, 2009.

[13] W. Cabot and P. Moin. Approximate wall boundary conditions in the large-eddy simulation of high Reynolds number flow. *Flow, Turbulence and Combustion*, 63:269–291, 2000.

[14] T. G. Bagwell, R. J. Adrian, R. D. Moser, and J. Kim. Improved approximation of wall shear stress boundary conditions for large eddy simulation. *Near-wall turbulent flows International conference*, 1993.

[15] J. Jimenez and C. Vasco. Approximate lateral boundary conditions for turbulent simulations. *Center for Turbulence Research, Proceedings of the Summer Program 1998*, pages 269–291, 1998.

[16] F. Nicoud, G. Winckelmans, D. Carati, J. Baggett, and W. Cabot. Boundary conditions for LES away from the wall. *Center for Turbulence Research, Proceedings of the Summer Program 1998*, 1998.

[17] T.-H. Shih, L. A. Povinelli, and N.-S. Liu. Application of generalized wall function for complex turbulent flows. *Journal of Turbulence*, 4(15), 2003.

[18] M. Wang and P. Moin. Dynamic wall modeling for large-eddy simulation of complex turbulent flows. *Physics of Fluids*, 14, 2002.

[19] Z. L. Chen, S. Hickel, A. Devesa, J. Berland, and N. A. Adams. Wall modeling for implicit large-eddy simulation and immersed-interface methods. *Theoretical and Computational Fluid Dynamics*, 28:1–21, 2014.

[20] C. Duprat, G. Balarac, O. Metais, P. M. Congedo, and O. Brugiere. A wall-layer model for large-eddy simulations of turbulent flows with/out pressure gradient. *Physics of Fluids*, 23, 2011.

[21] S. Hickel and N. A. Adams. Implicit LES applied to zero-pressure-gradient and adverse-pressure-gradient boundary-layer turbulence. *International Journal of Heat and Fluid Flow*, 29:626–639, 2008.

[22] S. Hickel, E. Touber, J. Bodart, and J. Larsson. A parametrized non-equilibrium wall-model for large-eddy simulations. *Center of Turbulence Research, Proceedings of the Summer Programm 2012*, 2012.

[23] S. Hickel, N. A. Adams, and J. A. Domaradzki. An adaptive local deconvolution method for implicit LES. *Journal of Computational Physics*, 213:413–436, 2006.

[24] J. C. del Alamo, J. Jimenez, P. Zandonade, and R. D. Moser. Scaling of the energy spectra of turbulent channels. *Journal of Fluid Mechanics*, 500(15):135–144, 2004.

[25] S. Hickel and N. A. Adams. On implicit subgrid-scale modeling in wall-bounded

flows. *Physics of Fluids*, 19, 2007.

[26] S. Kawai and J. Larsson. Dynamic non-equilibrium wall-modeling for large eddy simulation at high reynolds numbers. *Physics of Fluids*, 25, 2013.

[27] P. Dupont, C. Haddad, and J.F. Debieve. Space and time organization in a shock-induced separated boundary layer. *Journal of Fluid Mechanics*, 559:255–277, 2003.

[28] B. Budich. Untersuchungen zur passiven beeinflussung turbulenter stoss-grenzschicht-wechselwirkungendurch mikro-wirbelgeneratoren. Master's thesis, TU Munich, 2012.

[29] T. Cebeci and J. Cousteix. *Modeling and Computation of Boundary-layer Flows, 2nd edition*. Horizons Publishing, 2005.

[30] D. R. Lynch. *Numerical Partial Differential Equations for Environmental Scientists and Engineers*. Springer, 2005.